Drag Reduction in Turbulent Pipe Flow by Transverse Wall Oscillations at Low and Moderate Reynolds Number

by

Daniel Coxe

A Thesis Presented in Partial Fulfillment
of the Requirements for the Degree
Master of Science

Approved March 2019 by the
Graduate Supervisory Committee:

Ronald Adrian, Co-Chair
Yulia Peet, Co-Chair
Marcus Herrmann

ARIZONA STATE UNIVERSITY

May 2019

ABSTRACT

This work helps to explain the drag reduction mechanisms at low and moderate turbulent Reynolds numbers in pipe flows. Through direct numerical simulation, the effects of wall oscillations are observed on the turbulence in both the near wall and the bulk region. Analysis of the average Reynolds Stresses at various phases of the flow is provided along with probability density functions of the fluctuating components of velocity and vorticity. The flow is also visualized to observe, qualitatively, changes in the total and fluctuating field of velocity and vorticity. Linear Stochastic Estimation is used to create a conditional eddy (associated with stress production) in the flow and visualize the effects of transverse wall oscillations on hairpin growth, auto-generation and structure.

DEDICATION

I would like to dedicate this work to my family. Especially my parents who have been supportive of my academic endeavors throughout my life.

ACKNOWLEDGMENTS

I wish to thank my graduate research advisors, Regents' Professor Ronald J. Adrian and Professor Yulia A. Peet, for their guidance and insight. Computational Resources were supported by the Extreme Science and Engineering Discovery Environment (XSEDE), which is supported by TG-ENG150019. Furthermore, the work was also supported by the Ira A. Fulton Professorship in Mechanical and Aerospace Engineering.

TABLE OF CONTENTS

CHAPTER Page

CHAPTER Page

APPENDIX

LIST OF TABLES

Table Page

LIST OF FIGURES

Figure Page

Figure Page

Figure Page

Figure Page

Chapter 1

Introduction

1.1 Background

When a fluid flows over a surface a force due to viscosity and the viscous shear rate occurs at the wall's surface. Integrated over the surface this force is referred to as the skin friction or the viscous drag; if the flow is laminar then viscous drag is proportional to the flow velocity; but if the flow is turbulent the drag is proportional to the square of velocity and increases rapidly with Reynolds number.

Viscous stress is alway the agency creating viscous drag in laminar and turbulent flow, but the turbulent transport of high momentum fluid towards the wall and low momentum fluid away from the wall sharpens the velocity gradient at the wall, thereby increasing the viscous wall shear stress. The motions take the form of wallward sweeps and outward ejections (Corino and Brodkey (1969), Willmarth and Lu (1972)). Ejections see low momentum fluid transported from the buffer region up into the log region (Corino and Brodkey (1969)).

Adrian (2007) summarized research showing that these ejection events are correlated with the organization and coherence of packets of turbulent hairpins. These hairpins are regions of high quasi-streamwise vorticity around $10 < y^+ < 20$ (see 2.18 for definition of

y^+), radial vorticity in $20 < y^+ < 40$, and azimuthal vorticity in the head of the hairpin. These vortices tend to organize and form *packets* which induce a velocity to carry low momentum fluid up out of the log layer and into the bulk region. By continuity ejections are associated with sweep of high-momentum fluid to replace the displaced low-momentum fluid. Self induction causes hairpins to lift out further towards the outer region. The shear imposes vortex stretching which increases the ejection and forms new hairpins thus sustaining the process. The creation of new hairpins in a packet is called autogeneration Zhou *et al.* (1996). It occurs if the fast hairpin has sufficient strength.

1.1.1 Pipe Flow Motivation

Pipe flow is critical to transport of industrial fluids: oil, gas, water, steam, etc. In general, these are all very high Reynolds number applications. As an example, the Alaskan North Slope pipeline has a Reynolds number varying between $1.5(10^4)$ and $5.5(10^5)$(Company (2016)). Any energy savings achieved by reduction (especially in the cold of Alaska) equates to large reduction of pumping costs; a simple but effective means to decrease pumping costs, is desirable. Additionally, a system that can be implemented without extensive modification to the pipe domain is also necessary. Methods of drag reduction follows:

1.2 Drag Reduction Mechanisms

There are two broad classes of drag reduction: passive and active. Passive drag reduction is characterized by no energy being introduced into the system. It is achieved by modifying the surface roughness in anisotropic manner to reduce skin friction . However, these methods have the deficiency of being Reynold's number dependent. Two examples are elasto-polymer injection which adds long chain polymers to the flow to eat up momentum robbing turbulent structures near the wall Yang (2009) and riblets Garcia-Mayoral and Jimenez (2011a).

Generally, performance degrades with increasingly turbulent flow. Active control does work on the flow with the goal of net energy savings. The flow control mechanism, in general effect the near wall turbulence such that the mean streamwise velocity gradient is decreased. An example of such a method is wall oscillations which act to mitigate the growth of said structures Choi and Clayton (2001).

In general all these mechanisms are predicated on one thing: modifications of the near wall turbulence. It is imperative to see what the turbulence is doing near the wall. It is also necessary to understand what is occurring when the flow near the wall interacts with the flow in the bulk. This is broadly understood to be sweep and ejection events. Adrian showed that there are packets that tend to organize into larger structures in boundary layer flow and assist with the transport of low momentum fluid away from the wall and high momentum fluid towards the wall.

These near wall turbulent structures act to extract energy from the mean flow and dissipate it at the walls. As previously mentioned, there are two key turbulent events that do this: sweeps and ejections. Sweep events occur when high momentum fluid packets from the bulk flow are guided down to the wall by the (spanwise) vortical structures in the flow. This fluid is forced into a region of low momentum, thus pulling kinetic energy out of the mean flow. Ejection events are characterized by low momentum fluid from the near wall fluid being forced up into the bulk flow region. The bulk flow accelerates this low momentum fluid, expending some of its own kinetic energy along the way. The net effect is a steep mean streamwise velocity gradient at the wall and a nearly flat velocity profile outside the buffer layer.

1.2.1 Passive Methods

Riblets

As previously stated, riblets modify wall roughness in such that drag is reduced. The intuition guiding this is that low and high speed streaks near the wall will be disrupted by the non-uniform geometry, provided the interference is disruptive. It has been well established that drag reduction up to 11% is achievable Choi (2000). However, it is also known that this drag reduction is geometry specific (although a good collapse is presented in Mayoral and Jiminez 2011 using a 'projected area' of $Ag^{+1/2} = 11$). The reasoning behind these riblets interfere with the low speed streaks and streamwise vorticity is not able to lift it up as easily. Given, the reynolds number dependence on spacing, the operation range must be known a-priori. Furthermore, deviations into higher Reynolds number flows show an increase in drag (for a given geometry).

There are several explainations for this drag increase:

1. generation of secondary vortices which counteract sweeps and ejections(Goldstein and Tuan (1998))

2. the characteristic length scale of the riblets is related to turbulent structures in the near wall region (Choi *et al.* (1993))

3. the generation and amplification of spanwise roll cells (Garcia-Mayoral and Jimenez (2011b))

Polymer Additives

Polymer additives requires the addition of elasto-polymer substance on the order of parts per million to reduce drag. These polymers change the fundamental physics of the flow from (typically) newtonian fluid flow to non-newtonian. These elasto-polymers, as the name

would imply, behave like a spring when sheared and the presence of such polymers, the fluid is modeled as a 'viscoelastic fluid'. Such models exist as the FENE-P and Oldroyd-B models for numerical simulations.

Drag reduction of upwards of 30% can be reliably achieved in channel flow with increased viscoelasticity (Min *et al.* (2003)). However, in order for drag reduction to occur viscoelastic flow requires a minimum criterion to be effective. Several proposals for this threshold exist:

1. $We_\tau = \frac{\lambda u_\tau^2}{\nu} > \alpha$ (Goldshtik *et al.* (1982)) shows that the relative strength of the elastic forces to viscous forces must be greater than the some parameter (characteristic of the viscoelastic model)

2. $\lambda > \frac{\nu}{u_\tau^2}$ This is known as the time criterion (Lumley (1969)). This characterizes that the relaxation time (λ) must be longer than the near wall turbulence time scale.

Effectively, polymer drag reduction is conditioned on the wall shear. This would imply that the polymer needs a minimum amount of shear to be effective.

1.2.2 Active Methods

Active drag reduction methods can be further broken down into two more classes: open-loop and closed-loop. Wall modifications/wall oscillations are a kind of open loop because no flow parameters that are fed-back as a parameter to control the flow. These methods are simple to implement and have shown up to 40% drag reduction (Choi *et al.* (2002)) for wall modifications. Closed-loop as the name would imply, requires the measurement of one or more flow parameters such that a control surface can be modulated to effect drag reduction. Examples of such sensed parameters include wall normal velocity, spanwise velocity, and streamwise velocity (Choi *et al.* (1994))

Wall Modifications

Wall modifications are distinct from Oscillations and riblets in that the wall deforms or changes in some way. Examples includes:

1. wall suction/blowing
2. bubble release from walls
3. wall deformations

Wall suction and blowing was explored thoroughly by Choi *et al.* (1994) where the author sought to control the wall normal, streamwise, spanwise, and velocity fluctations with either 'in-phase' or 'out-of-phase' suction/blowing. Control of the normal velocity was used to attempt to suppress the aforementioned sweep and ejection events. This was accomplished by applying an exactly opposite normal component of velocity at the wall (where the velocity was equal and opposite relative to some distance away from the wall). Skin friction reduction around 25% was accomplished using this method when the measured velocity was $y^+ = 10$ units away. Additionally, the power savings in this method were also very high indicating the efficacy of the method. Spanwise velocity control was implemented to counter streamwise vorticity near the walls. Drag increased when the sensing location was set to $y_d^+ = 20$, however $y_d^+ = 10$ yielded similar drag reduction to wall-normal control. Combined control of wall-normal and spanwise velocity completely suppressed turbulence, the caveat being the low Reynolds number of the flow. Lastly, streamwise control resulted in a maximum of 10% drag reduction when the wall velocity was 'in-phase' with the measured velocity, otherwise the drag increase was observed.

The principle behind bubble injection arrived from the idea of placing a layer of air between a ship and the water boundary layer to reduce skin friction (Madavan *et al.* (1984)). Although a solid layer is not practically implementable, microbubbles that are injected from

the wall is. Depending upon the method employed to deploy the bubbles, drag reduction upward of 70% is possible (Latorre and Babenko (1998)). The method of by which this drag reduction occurs is from the introduction of 'voids' in the boundary layer. These voids appear to prevent the formation of cohesive vortices which promote Reynolds stress production.

Wall deformations are wall normal deformations that *squeeze* and *expand* the flow. Direct numerical simulation of such wall modifications have resulted in upwards of 65% drag reduction resulting from the re-laminarization of the flow (Nakanishi *et al.* (2012)), albeit at low turbulent Reynolds number ($Re_\tau = 180$, based on unmodified case). This test further showed that for downstream traveling waves (in general) drag decreased, while upstream traveling waves showed drag increases. It is worth noting that peak drag reduction in this study results from a period of oscillation very close to spanwise wall velocity oscillations ($T^+ = 125$ vs $T^+ = 100$). Less effective is applying spanwise traveling wall deformation, yielding a maximum drag reduction of only 13.4% (Tomiyama and Fukagata (2013)). In this simulation, the traveling wave is given the typical wavelength $\lambda^+ = 100$ as this is expected to interact with the previously mentioned low speed streaks near the wall.

Wall Oscillations

The subject of investigation, drag reduction by wall oscillations is an effective mechanism of drag reduction Choi and Clayton (2001), Baron and Quadrio (1995), Quadrio and Ricco (2004). Wall Oscillations are characterized by applying a transverse wall velocity, i.e.:

$$\mathbf{u}_{\text{wall}}(t) = \mathbf{U} \sin\left(\frac{2\pi}{T} t\right) \tag{1.1}$$

where T is the period of oscillation and U is the amplitude of wall velocity.

Turbulent drag reduction is readily achievable in channel, boundary layer, and pipe flow

(Zhou and Ball (2008)) using sinusoidally varying transverse wall velocity. The motivation behind this method is that, similar to wall deformation, the imposed motion at the boundaries interact and disrupt the turbulent sweep and ejection events. Since these events are associated with streamwise vorticity, spanwise wall oscillations are likely to be a method by which drag reduction can be achieved.

Spatially varying waves (Skote (2013)) and traveling waves (Quadrio *et al.* (2009)) have shown even greater drag reduction for these boundary layer and channel flows. All papers cited are in agreement with regards to an optimal frequency and amplitude of oscillation. This optimal frequency has been discovered to be $T^+ \approx 100$ at low Reynolds number in turbulent channel flow (here '+' notation denote non-dimensionalization by friction velocity and kinematic viscosity Tennekes *et al.* (1972)). The reasoning for this is two fold:

1. In the buffer layer ($0 \leq y^+ \leq 30$) the turbulent structures are quasi-streamwise vortices with spacing of $\lambda^+ \cong 100$

2. The stokes layer should extend into the region where these structures persist

The second item, the Stoke's Layer is a phenomenon that arises from a classical solution to the Navier-Stokes equations known as Stoke's Problem. This problem is formulated as a viscous quiescent flow that comes under the influence of an oscillating wall. In the wall normal direction, since flow is considered to be one-dimensional, momentum can only by transported by viscous diffusion. Hence a decaying exponential multiplied by a sine wave with a phase shift proportional to the distance from the wall describes the velocity profile. In the near wall region of the oscillating turbulent pipe flow, below the buffer layer, the viscous forces dominate the azimuthal flow and be approximated by the Stokes problem profile. The Stokes layer would be approximated by:

$$\delta^+ = 4.5 \left(\frac{T^+}{\pi} \right)^{1/2} \tag{1.2}$$

We hypothesize that the wall oscillations act upon the streamwise vorticity which suppresses the turbulent ejection and sweep events. Particularly it is presumed that previously mentioned mechanism of autogeneration of turbulent hairpins is suppressed or modified in a way that reduces the rate of ejections and sweeps.

Chapter 2

Pipe Flow Physics

Pipe flow is characterized by a mean pressure gradient driving an internal flow between walls. For a steady, fully developed flow in a pipe, driven by an end-to-end pressure drop, the temporally averaged force balance relates the pressure drop to the wall shear stress τ_{wall} Panton (1984):

$$(\Delta p)\pi R^2 = (\overline{\tau}_{wall})2\pi RL \tag{2.1}$$

This result is usually derived for laminar, steady, fully developed, incompressible flow analysis but it pertains quite well to steady, fully developed, incompressible turbulent flow.

2.1 Turbulent Pipe Flow Analysis

To ease the complications of analytically dealing a non-rectilinear geometry with cartesian coordinates and for the purposes of analysis only the Navier Stokes equations are presented in cylindrical coordinates here. However, all solutions of these equations acquired numerically are calculated on a cartesian grid with a numerical discretization of curved edges, as will be discussed later.

2.1.1 Governing Equations

Incompressible continuity defines the conservation of mass in the domain.

$$\frac{1}{r}\frac{\partial}{\partial r}(rv_r) + \frac{1}{r}\frac{\partial}{\partial \theta}(v_\theta) + \frac{\partial}{\partial x}(v_x) = 0 \tag{2.2}$$

Where (r, θ, x) are the radial, azimuthal, and axial coordinates. The corresponding velocity components are (v_r, v_θ, v_x). In full, the cylindrical coordinate Navier-Stokes Equations are as follows:

$$\frac{\partial v_r}{\partial t}+v_r\frac{\partial v_r}{\partial r}+\frac{v_\theta}{r}\frac{\partial v_r}{\partial \theta}-\frac{v_\theta^2}{r}+v_x\frac{\partial v_r}{v_x} = -\frac{1}{\rho}\frac{\partial p}{\partial r}+\nu\left\{\frac{\partial}{\partial r}\left[\frac{1}{r}\frac{\partial}{\partial r}(rv_r)\right]+\frac{1}{r^2}\frac{\partial^2 v_r}{\partial \theta^2}+\frac{\partial^2 v_r}{\partial z^2}-\frac{2}{r^2}\frac{\partial v_\theta}{\partial \theta}\right\} \tag{2.3}$$

$$\frac{\partial v_\theta}{\partial t}+v_r\frac{\partial v_\theta}{\partial r}+\frac{v_\theta}{r}\frac{\partial v_\theta}{\partial \theta}-\frac{v_\theta v_r}{r}+v_x\frac{\partial v_\theta}{v_x} = -\frac{1}{r\rho}\frac{\partial p}{\partial \theta}+\nu\left\{\frac{\partial}{\partial r}\left[\frac{1}{r}\frac{\partial}{\partial r}(rv_\theta)\right]+\frac{1}{r^2}\frac{\partial^2 v_\theta}{\partial \theta^2}+\frac{\partial^2 v_\theta}{\partial z^2}-\frac{2}{r^2}\frac{\partial v_r}{\partial \theta}\right\} \tag{2.4}$$

$$\frac{\partial v_x}{\partial t}+v_r\frac{\partial v_x}{\partial r}+\frac{v_\theta}{r}\frac{\partial v_x}{\partial \theta}+v_x\frac{\partial v_\theta}{v_x} = -\frac{1}{\rho}\frac{\partial p}{\partial z}+\nu\left\{\frac{1}{r}\frac{\partial}{\partial r}\left[r\frac{\partial}{\partial r}v_x\right]+\frac{1}{r^2}\frac{\partial^2 v_x}{\partial \theta^2}+\frac{\partial^2 v_\theta}{\partial z^2}\right\} \tag{2.5}$$

On *average* the flow must be axisymmetric, the mean continuity equation reduces to

$$\frac{1}{r}\frac{\partial(r\overline{v_r})}{\partial r}+\frac{\partial \overline{v_x}}{\partial x} = 0 \tag{2.6}$$

This requires $\overline{v_r}$ to be zero everywhere because the fully developed criterion means that at every radial coordinate, the gradient of streamwise velocity is 0 in the streamwise direction, and thus so is the mean radial velocity radial derivative. This forces the mean radial velocity to be constant, which then (by impermeability of the wall) requires that constant to be zero.

The time averaged momentum equations reduces to only two, one for streamwise shear and one for radial velocity fluctuations.

$$\overline{\tau} = \rho\overline{u'_x u'_r} + \mu\frac{\partial u_x}{\partial y} \tag{2.7}$$

$$\frac{1}{r}\frac{dr\overline{\tau}}{dr} - \frac{\partial \overline{p}}{\partial x} = 0 \tag{2.8}$$

$$\frac{d\overline{v'^2_r}}{dr} + \frac{\overline{v'^2_r} - \overline{v'^2_x}}{r} + \frac{1}{\rho}\frac{d\overline{p}}{dr} \tag{2.9}$$

In equation 2.8 $\overline{\tau}$ represents all stresses acting to accelerate the streamwise momentum: viscous and turbulent. Lumping the two together is a matter of convenience. Equation 2.9 gives the mean transport of radial fluctuations. However it is only necessary for the purposes of justifying the simulation method that the streamwise shear is given by equation 2.10.

$$\overline{\tau} = \frac{d\overline{p_w}}{dx}\frac{r}{2} \tag{2.10}$$

This is because if one integrates the equation for the radial distribution of pressure it can be seen that deviation from the wall pressure is very small due to the mean square fluctuations being small. Hence, the *average* wall shear stress and mean pressure gradient are directly related by

$$\frac{d\overline{P_w}}{dx} = 2\frac{\overline{\tau}_{wall}}{R} \tag{2.11}$$

2.1.2 Solution to Stokes Oscillating plate

For large enough Reynolds number, the laminar region of the flow is very thin compared to the pipe curvature. As such the behavior in the near wall region can appear to behave like a flow past a flat wall. Let $y = R - r$ be the coordinate perpendicular to the wall then for

all turbulent wall bounded flows the laminar sublayer is $y^+ \approxeq 10$ in height. This compared to the overall radius of curvature which is $R^+ > 100$ in height. Thus the laminar sublayer is less than 5% of the radius is laminar and the near wall region can be treated as a flat wall.

Using this assumption, the laminar flow created by an oscillating pipe wall has a transverse velocity give by 2.12.

$$U_\theta(Y) = \exp\left(-\frac{Y}{\sqrt{2}}\right)\sin\left(T - \frac{Y}{\sqrt{2}}\right) \tag{2.12}$$

where $Y = \frac{y}{\nu/\Omega}^{1/2}$, $T = t\Omega$, and $U_\theta = \frac{u_\theta}{u_{wall}}$. In this expression, ν is the fluid kinematic viscosity, Ω is the frequency of the wall oscillation, and U_θ is the amplitude of the wall velocity. This expression, when normalized by inner units will be shown to track the average azimuthal velocity in the pipe out to the total thickness of the Stokes layer.

The stokes layer is defined as the location at which the induced velocity in the fluid reaches 1% of the wall velocity. This location is given by $\delta = 4.5\left(\sqrt{\frac{2\nu}{\Omega}}\right)^{1/2}$.

2.2 Outer Parameters

Recalling the definition of the shear stress tensor

$$\tau_{ij} = \mu\left(\frac{\partial u_i}{\partial x_j} + \frac{\partial u_j}{\partial x_i}\right) \tag{2.13}$$

The force balance at the wall can be shown to be:

$$\begin{gathered} \tau_{\text{wall}} = \mu\frac{dv_x}{dr}|_{r=R} = -\frac{R}{2}\frac{dp}{dz} \\ \downarrow \\ 2\pi RL(\tau_{\text{wall}}) = \pi R^2(\Delta p) \end{gathered} \tag{2.14}$$

Let U_{bulk} be the outer scale for velocity and, along with the viscosity and pipe diameter, defines the bulk Reynolds number:

$$\mathbf{Re} = \frac{U_{bulk}\mathrm{D}}{\nu} \tag{2.15}$$

Outer scaling parameters follows:

- U_{bulk}; the bulk mean velocity and characteristic outer scale velocity
- D; the pipe diameter is the size order of the largest scale structures in the domain
- $\frac{\mathrm{D}}{U_{bulk}}$; the characteristic outer time scale of events
- ρU_{bulk}^2; the outer scale pressure term

As the name suggests, the outer scale variables describe the *largest* scales of motion. These are phenomena that occur at sizes of the order a pipe diameter, over time scales of the order of the time required for a particle to convect from the top to bottom of the pipe and with momentum on the order of the bulk mean velocity. These parameters act to normalized these outer scale quantities to O(1).

2.3 Inner Parameters

A set of variables is necessary to scale up the small values of velocity, pressure, and stress fluctuations. Such scaling parameters arise from the dissipation of energy due to viscous wall shear. Noting that a *shear velocity* can be formed from the square root of the stress per unit mass:

$$\mathrm{u}_\tau = \sqrt{\frac{\overline{\tau}_{wall}}{\rho}} \tag{2.16}$$

A second Reynolds Number, referred to as *Reynolds* τ to characterize the flow based on inner scalings:

$$\mathbf{Re}_\tau = \frac{\mathrm{u}_\tau \mathrm{R}}{\nu} \tag{2.17}$$

Taking note of the dimensions, we can see the beginning of a development of a complete set of inner scaling variables

- $\mathrm{u}_\tau = \sqrt{\frac{\tau_{wall}}{\rho}}$ is the shear velocity (previously stated)
- $l_\tau = \nu/\mathrm{u}_\tau$ is the viscous length scale
- $t_\tau = \nu/\mathrm{u}_\tau^2$ is the viscous time scale

Equation 2.20 allows for an a-priori approximation of inner scaling on length $l_\tau = \frac{\nu}{u_\tau}$ which shows that the ratio of outer to inner length scale is given by $\frac{R}{l_\tau} = \frac{u_\tau R}{\nu} = Re_\tau$. This length scale will be used shortly to demonstrate the viability of wall oscillations scaling with Reynolds number. A time scale is also available by, $t_\tau = \frac{l_\tau}{u_\tau}$.

Henceforth, anytime the following notation occurs (equation 2.18), the respective variable will have been non-dimensionalized in inner variables unless otherwise stated

$$(\mathbf{X})^+. \tag{2.18}$$

2.4 Wall Oscillation Scaling

For a range of bulk Reynolds numbers between $5000 \leq Re_{bulk} \leq 100000$ the equation by Blasius El Khoury *et al.* (2013) for smooth pipe friction factor gives an accurate prediction of Re_τ (equations 2.20).

$$Re_\tau = 0.099 Re_{bulk}^{0.875} \tag{2.19}$$

However, if we temporarily define $Re_\tau = \frac{u_\tau D}{\nu}$ then scaling collapses in the following way.

$$Re_\tau = 0.199 Re_{bulk}^{0.875} \tag{2.20}$$

Wall modifications are always prescribed in terms of inner parameters. From a review of Choi *et al.* (2002), an optimal (where optimal is defined as maximum drag and net energy savings) wall velocity and period in channel flow can be observed to be: $U_{wall} = 10u_\tau$ and $T_{wall} = 100t_\tau$.

This leads to a peak to peak wall displacement of $W_D = \frac{2000}{\pi} u_\tau t_\tau = \frac{2000}{\pi} l_\tau$. As a fraction of circumference this can be shown to be: $\frac{W_D}{C} = \frac{2000 l_\tau}{\pi^2 2R/} = \frac{2000}{\pi^2 Re_\tau}$. Applying the empirical correlation for Reynolds number as given by the Blasius relation (eq 2.20) we can see that $\frac{W_D}{C} \approx \frac{10000}{\pi^2 Re_{bulk}^{.875}}$.

Similarly for the time scale, as a fraction of a characteristic outer time scale, $\frac{T_{osc}}{T_O} = \frac{100 t_\tau u_{bulk}}{D_h} = 100 \frac{Re_{bulk}}{Re_\tau^2}$. Again, applying the Blasius approximation this yields: $\frac{T_{osc}}{T_O} = \frac{2500}{Re_{bulk}^{.75}}$.

Thus in terms of outer units we can see that the following relations roughly hold:

$$T_{osc} = \frac{2500 D_h}{u_{bulk} Re_{bulk}^{.75}} \tag{2.21}$$

$$W_D = \frac{20000 D_h}{\pi Re_{bulk}^{.875}} \tag{2.22}$$

Implying that at most, the wall displacement will scale with D_h^{125}

2.5 Statistical Calculations

2.5.1 Averaging

The average or expected value of a flow is the most useful property for understanding how a flow behaves at large scales. The average of a random variable (e.g. velocity) determines

the most likely state over all possible realizable states. This allows one to further generate other statistical quantities by defining a mean field with a fluctuating field superimposed. These fluctuations have the very useful property of being zero mean which allows for the development of central moments which allow for further characterization.

In order to define the expected value of a field an averaging operator must be defined. The gold standard of averaging is the *ensemble average* given by equation 2.23. Here $\mathbf{X}_i$ is a measured random variable where each measurement is identically distributed and independent. This gives the *true* expected value.

$$\overline{\mathbf{X}} = \lim_{N\to\infty} \frac{1}{N} \sum_{i=1}^{N} \mathbf{X}_i \tag{2.23}$$

Practically speaking, running simulations to achieve identically distributed independent data sets is not possible but it is also not necessary given the problem formulation. Two particular properties of pipe flow allow for convergence to the ensemble average without having to start the flow from an infinite number of initial conditions. These two properties are that the flow is homogeneous in two spatial directions and statistically stationary.

2.5.2 Spatial Homogeneity

Statistical homogeneity states that distribution of realizable states is invariant of location along the coordinate given by equation 2.24.

$$P(a \leq u(x_1) \leq b) = P(a \leq u(x_2) \leq b) \forall a, b \mid a < b \tag{2.24}$$

A fully-developed smooth pipe flow naturally exhibits azimuthal and streamwise homogeneity along with statistical stationarity. The implication of this properties is that all statistical quantities (averages, variances, distributions, etc) can be shown to be dependent on radial location alone and that this can employed to assist with convergence to the ensemble by integrating over all homogeneous directions.

2.5.3 Stationarity Principle

Similar to homogeneity, stationarity implies that the statistics are not changing in time as shown in equation 2.25.

$$P(a \leq u(t) \leq b) = P(a \leq u(t+\tau) \leq b) \forall a, b \mid a < b \tag{2.25}$$

As with homogeneity, temporal integration is employed to converge to the ensemble average.

2.5.4 Averaging Operators

Instead of attempting to perform an ensemble average, operators utilizing the previous two properties are defined that will converge towards the ensemble average. In the most general sense, an averaging operator is given by equation 2.26 where $\mathbf{X}$ is the random variable and the x_i is the coordinate of averaging.

$$\langle \mathbf{Q} \rangle_{x_i} = \frac{\int_{x_i} \mathbf{Q} dx_i}{\int_{x_i} dx_i} \tag{2.26}$$

Throughout the research presented, the random variable $\mathbf{Q}$ is most often the velocity however turbulent budget terms are also used at times to further characterize drag reduction. Most often, averaging will be performed in the azimuthal and streamwise directions along with in a time averaging. Hence, most common average will look like equation 2.27

$$\langle \mathbf{u}(r) \rangle_{\theta,x,t} = \frac{1}{2\pi L_x T} \int_0^{L_x} \int_0^{2\pi} \int_0^{T} \mathbf{u}(r, \theta, x, t) dt d\theta dx \tag{2.27}$$

Since the simulation is a set of discrete points, the averaging integral is transformed into a summation given by equation

$$\langle \mathbf{u}(r_l) \rangle_{\theta,x,t} \approx \frac{1}{N_x N_\theta N_t} \sum_{k=1}^{N_x} \sum_{j=1}^{N_\theta} \sum_{i=1}^{N_t} \mathbf{u}(r_l, \theta_j, x_k, t_i) \tag{2.28}$$

Here the summation is represented in the order over which averaging occurs, first in time, then azimuthal, then finally streamwise direction. If any variable is presented as $\overline{(\cdot)}$ that implies an average over all homogeneous dimensions available.

2.5.5 Fluctating Quantities

Although the statistics are stationary, the flow still changes through realizable states from timestep to timestep, a fluctuating velocity can be defined as an instantaneous realization of the flow minus the mean, i.e. equation 2.29

$$\mathbf{u}' = u - \langle u \rangle_{x_i} \tag{2.29}$$

These fluctuations characterize the nature of the turbulence in the flow and thus it is necessary to have a well defined averaging notation in order to accurately determine the behavior.

$$\overline{u} = \langle u \rangle_{\theta,x,t} \tag{2.30}$$

Fluctuation visualizations also obey equation 2.30. Likewise, single point statistics and distributions are presented as an average over streamwise and azimithal average along with time averaging, i.e. equation 2.28.

2.5.6 Conditional Averaging

A conditional average is defined as the average given that some condition is met regarding the coordinate system or flow configuration. The notation for such a conditional average is given by 2.31. Example 2.32 shows the usage of this conditional as applied to calculating the wall shear stress of the flow through a pipe. The average viscous shear stress is evaluated given that the radial location is at the wall (i.e. maximum laminar shear).

$$\langle u|\phi_j\rangle_{x_i} \tag{2.31}$$

$$\langle \tau_{zr}(r)|r=R\rangle_{r,\theta,z} = \frac{\int_0^L \int_0^{2\pi} \mu \frac{du_x}{dr} r \Big|_{r=R} d\theta dz}{\int_0^L \int_0^{2\pi} R d\theta dz} \tag{2.32}$$

The conditional average will be used to determine what will be referred to as the *phase averaged* quantities of the oscillated pipe. Equation 2.33 indicates the phase mean decomposition and figure 2.1 demonstrates the phenomenon graphically. It can be seen that if a random variable has deterministic behavior in time, then the standard long term time average will not subtract out the deterministic variance. Thus, in order to calculate the phase dependent turbulent fluctuations averaging must performed over a sufficiently small window of time around the phase or exactly at the phase. The research presented evaluates the statistics at the given phase (equation 2.33)

$$\langle u|t \mod (\frac{nT_{osc}}{N}) = 0\rangle, n = \{1, 2, \ldots N\} \tag{2.33}$$

This arises from the idea that there exists a triple decomposition of the flow field into a mean field, a sinusoidal fluctuation (induced by the wall), and a turbulent fluctuation (Hussain and Reynolds (1970)), i.e. equation, where u_ϕ is the sinusodal fluctuation and u' is the turbulent fluctuation. In that particular work, the authors sought a closure to determine the deterministic component of fluctuation but for the research presented the phase mean can be calculated directly by setting the averaging frequency to match the phase angle a-priori.

$$u = \langle u\rangle + u_\phi + u' \tag{2.34}$$

Hence, for the oscillating pipe, fluctuating quantities will be given as shown in equation 2.35

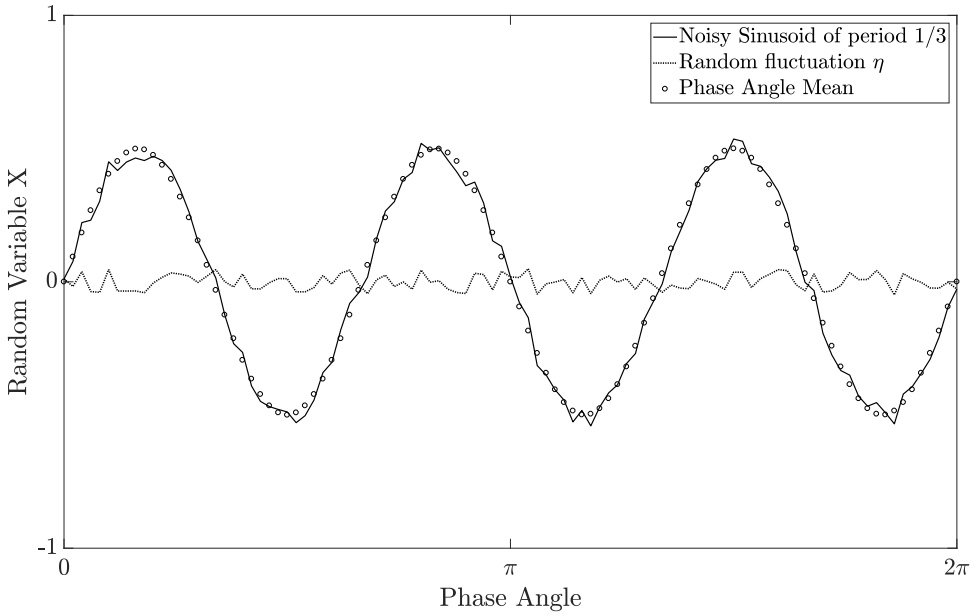

Figure 2.1: Demonstration of how phase averaging behaves using a well defined sinusoid $X(\phi) = 0.5\sin(3\phi) + \eta(\phi)$, here $\langle \mathbf{U} \rangle = 0$, $u_\phi = 0.5\sin(3\phi)$ thus if fluctuations where taken using the standard definition then a deterministic sinusoidal behavior would be superimposed onto the fluctuation statistics

$$u'(\mathbf{x}) = u(\mathbf{x}, t \mod (\frac{nT_{osc}}{N}) = 0) - \langle u | t \mod (\frac{nT_{osc}}{N}) = 0 \rangle, n = \{1, 2, \ldots N\} \tag{2.35}$$

Chapter 3

Simulation Method

This research utilizes a Direct Numerical Simulation approach to simulating fluid flow. No modeling appears except for the assumptions made regarding the Navier-Stokes equations. Particulary, those assumptions are:

1. Incompressible($\frac{D\rho}{Dt} = 0$)
2. Newtonian Fluid

Thus the equations being solved are the incompressible Navier-Stokes Equations in Cartesian Coordinates

$$\frac{\partial u_i}{\partial x_i} = 0 \tag{3.1}$$

$$\frac{\partial u_i}{\partial t} + u_j \frac{\partial u_i}{\partial x_j} = \frac{\partial p}{\partial x_i} + \frac{1}{Re} \frac{\partial^2 u_i}{\partial x_k^2} \tag{3.2}$$

3.1 Numerical Method

Spectral element code Nek5000 Deville *et al.* (2002) has been continually developed for more than 30 years. It is a fast, scalable and highly efficient high-order solver for compu-

tational fluid dynamics problems. Spectral element method (SEM) is similar in its form to finite element methods, but it utilizes high-order basis functions, specifically, high-order polynomials associated with the Gauss-Legendre-Lobatto quadrature points. It leverages the chosen polynomial approximation for a tensor-product efficiency that allows for a fast convergence.

The numerical scheme used in Nek5000 solves the incompressible Navier-Stokes equations with a backward-differentiation formula with time step δt and an explicit extrapolation for the convective term. Pressure p and velocity $\mathbf{u}$ are decoupled though a standard splitting operation in a following semi-discrete representation:

$$\begin{aligned} \frac{\beta_k \bar{\mathbf{u}}}{\delta t} - \frac{\mu}{\rho}\Delta\bar{\mathbf{u}} = -\sum_{j=1}^{k} \frac{\beta_{k-j}}{\delta t}\mathbf{u}^{n+1-j} \\ -\sum_{j=1}^{k} \alpha_j (\mathbf{u}\cdot\nabla\mathbf{u})^{n+1-j} - \frac{\nabla \bar{p}^{n+1}}{\rho}, \end{aligned} \tag{3.3}$$

$$\Delta(p^{n+1} - \bar{p}^{n+1}) = \nabla \cdot (\frac{\beta_k \bar{\mathbf{u}}}{\delta t}), \tag{3.4}$$

$$\mathbf{u}^{n+1} = \bar{\mathbf{u}} - \frac{\delta t}{\beta_k}\nabla\cdot(p^{n+1} - \bar{p}^{n+1}). \tag{3.5}$$

Here n is the time step index, ρ is the density of the fluid, μ is the dynamic viscosity, $\bar{\mathbf{u}}$ and $\bar{p}^{n+1} = 2p^n - p^{n-1}$ are the intermediate velocity and extrapolated pressure at $n+1$ time step, respectively. The terms β and α represent the coefficients of the backward difference and extrapolation schemes of a given convergence order k. In the current study, k is set to 2, corresponding to a second order accuracy in time both for velocity and pressure (Deville *et al.* (2002); Fischer (1997)).

Three-halves de-aliasing is applied to the convective terms to ensure that spurious energy is not cascaded from higher order modes to resolved modes. This may not have been totally necessary given the highly resolved nature of the simulation but it is a safer practice. Additionally, the highest order mode was attenuated with a filter weight of $\alpha = 0.01$. This attenuation is applied as given in Fischer and Mullen (2001) and can be thought of as a smooth projection from $N \rightarrow N-1$ space.

Nek5000 works purely in cartesian coordinates and thus for cylindrical/curvilinear domains, it is necessary to introduce a Jacobian tensor for all the deformed elements. The Jacobian tensor describes the skewness and volumetric change of an element in terms of a mapping from $(x_i) \rightarrow (\xi_i)$ where x_i is the deformed geometry and ξ_i is the undeformed computational domain given by equations 3.6.

$$J(\mathbf{r}) = \det\left(\frac{\partial x_i}{\partial r_j}\right) \tag{3.6}$$

Derivatives can then be represented using chain rule as in equation 3.7

$$\frac{\partial}{\partial x_k} = \frac{\partial}{\partial \xi_i}\frac{\partial \xi_i}{\partial x_k} \tag{3.7}$$

The derivatives in collocation form can be written as

$$\frac{\partial u}{\partial \xi_i} \mid_{klm} = \sum_{p=0}^{N} \hat{D}_{kp} u_{plm}, k, l, m \in 0, ..., N^3 \tag{3.8}$$

Where $\hat{D}$ is the spectral derivative matrix. To make the solution consistent with the geometry, a weighting matrix G_{ij} is introduced that contains the geometric mappings where

$$G_{ij} = \left[p \sum_{k=1}^{3} \frac{\partial \xi_i}{\partial x_k}\frac{\partial \xi_j}{\partial x_k} J(\mathbf{r}) \right]_{\xi_k, \xi_l, \xi_m} \rho_k \rho_l \rho_m \tag{3.9}$$

In equation 3.9 the terms ρ_i are the quadrature weights and p is just a coefficient.

3.2 Simulation Parameters

The simulations compared are $Re_\tau = \frac{u_\tau R}{\nu} = 170$ and $Re_\tau = 360$ based on the friction velocity. These correspond to bulk Reynolds of number of 5000 and 11700 respectively.

3.2.1 Fluid Properties

Parameter	Description	$Re_\tau = 170$	$Re_\tau = 360$
ρ	Fluid Density $\frac{\text{kg}}{\text{m}^3 s}$	1.0	1.0
ν	Kinematic Viscosity $\frac{m^2}{s}$	$2(10^{-4})$	$8.55(10^{-5})$

3.2.2 Domain Properties

Parameter	Description	$Re_\tau = 170$	$Re_\tau = 360$
D	Pipe Diameter (m)	1	1
L	Pipe Length (m)	12	12

3.2.3 Flow Parameters

Parameter	Description	$Re_\tau = 170$	$Re_\tau = 360$
U_{bulk}	Bulk mean velocity $^{\text{m}}/_{\text{s}}$	1.00	1.00
u_τ	Wall Friction velocity $^{\text{m}}/_{\text{s}}$	$6.800(10^{-2})$	$6.154(10^{-2})$
$\frac{dp}{dx}$	Pressure Gradient $^{\text{pa}}/_{m}$	$\frac{4\rho \text{u}_\tau^2}{D} = 0.0185$	0.0151

3.2.4 Simulation Parameters

Parameter	Description	$Re_\tau = 170$	$Re_\tau = 360$
T_{osc}	Wall oscillation period	4.32s	2.26s
dt	Simulation Time Step	$\frac{4.32}{(32)(250)}$s	$\frac{2.26}{(32)(250)}$s

3.2.5 Simulation Outer Scaling

Using the outer scaling relations from section 2.2 we can see that the following parameters apply

Parameter	Description	$Re_\tau = 170$	$Re_\tau = 360$
ρ	$\frac{\rho}{\rho_0}$	1.0	1.0
ν	$\frac{\nu}{U_{bulk}D}$	0.0002	$8.55(10^{-5})$

All flows are driving by a constant forcing function to maintain a constant long-term time average wall shear stress between the oscillated and non-oscillated pipe. The forcing function is given by solving $\frac{\Delta P}{L}$ as given in equation 2.1. It can be shown that the constant average pressure gradient is given by 3.10

$$f_i = \frac{\partial \overline{P}}{\partial x} = 2\frac{\overline{\tau}_{wall}}{R} \tag{3.10}$$

3.2.6 Mesh Parameters

The mesh was generated using the built in meshing utility to create a circular mesh of radius 0.5 for the $Re_\tau = 170$ case while the much finer mesh in the $Re_\tau = 360$ case had to be developed using a meshing utility known as HyperMesh. Grading near the wall is applied to achieve 5 grid points $R^+ < 1$. Table 3.1 lists all the mesh parameters for the current study.

Figures 3.1 and 3.2 illustrate the mesh densities for the the $Re_\tau = 170$ and 360 cases respectively. The figures also illustrate the implementation of grading near the wall to achieve the necessary grid resolution without wasting computational resources.

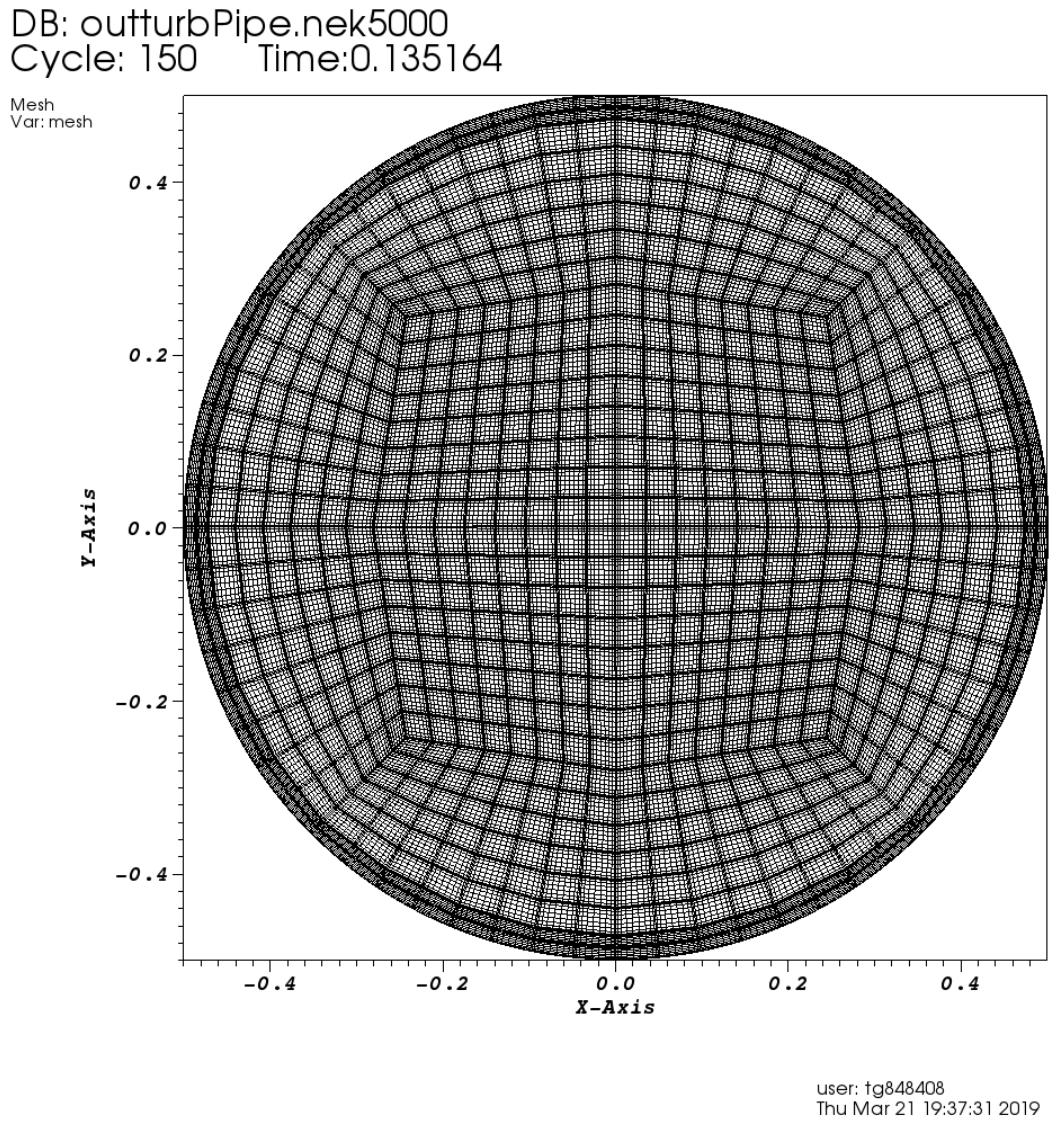

Figure 3.1: Mesh for the $Re_\tau = 170$ case

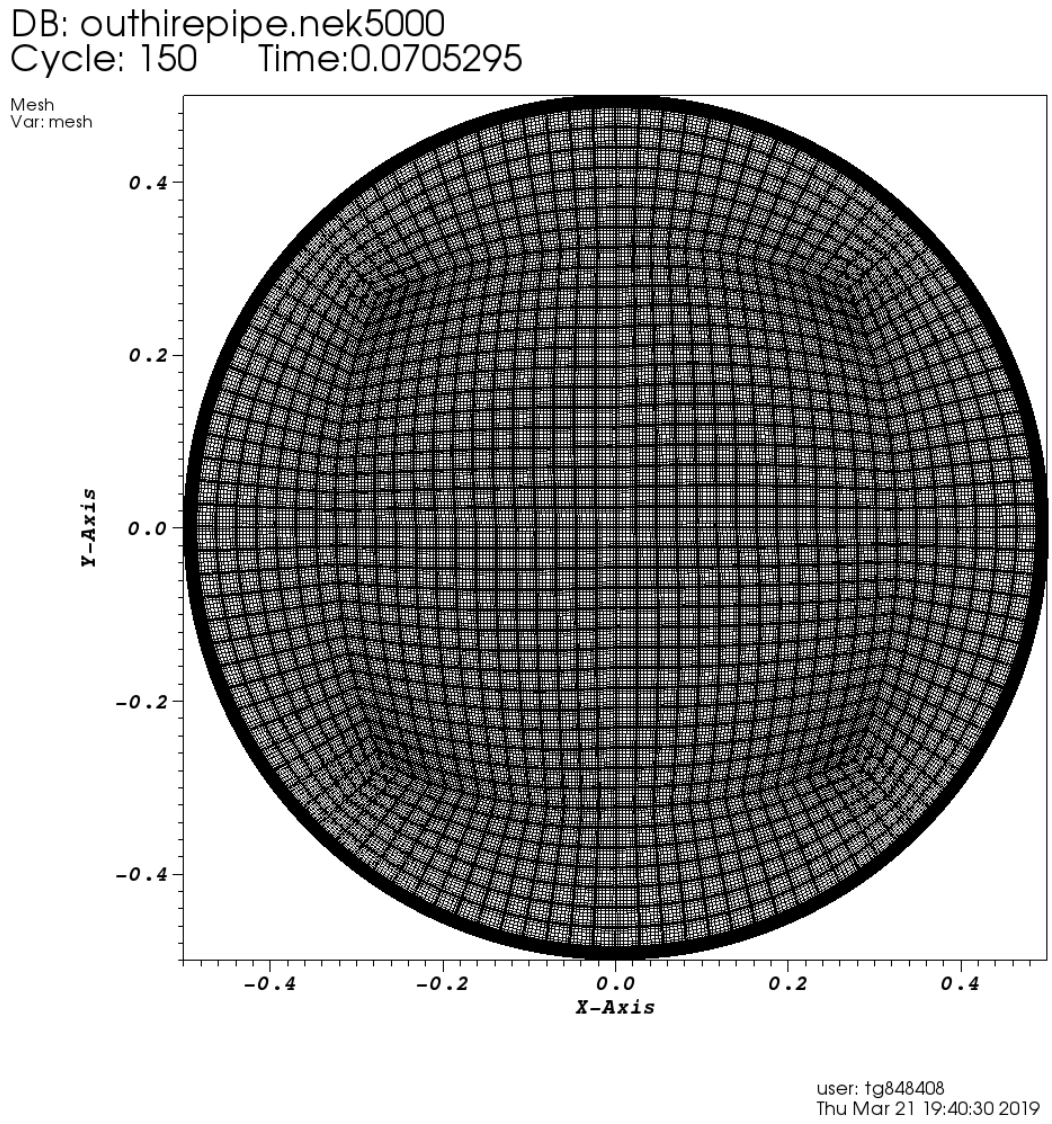

Figure 3.2: Mesh for the $Re_\tau = 360$ case

Re_τ	$N_{el,r-\theta}$	$N_{el,z}$	$N_{el,tot}$	$N_{gridpoints}$	Δr^+ min/max	$\Delta(r\theta)^+$ min/max	Δz^+ min/max
170	768	48	36864	36864000	.1/1.6	.67/2.75	3.4/14.05
360	2128	112	238336	173746944	.15/2.5	.81/3.30	2.9/11.90

Table 3.1: Mesh parameters of the two Reynolds number cases. Grid resolution is finest near the wall and near element boundaries. Due to GLL point distribution largest mesh spacing occurs at half an element thickness radius from the core and spaced even in the streamwise direction. The $Re_\tau = 170$ case used a 9^{th} order polynomial approximation while the $Re_\tau = 360$ utilized an 8^{th} order polynomial

3.3 Validation of Non-Oscillated Pipe by Comparison to Experimental and Numerical Data

To validate that all scales of motion are resolved to at least single point second order moments along with providing a baselines for data comparison, validation of mesh resolution is performed by simulating the standard turbulent pipe of length $24R$ and gathering temporally, azimuthally, and streamwise averaged turbulent statistics.

The simulation was started using the initial conditions from Sprague *et al.* and mapped into cylindrical coordinates.

$$\begin{aligned} \mathrm{u}_s/\mathrm{U}_{\mathrm{bulk}} &= 5(1-r^4)/4 + 0.3\cos(24\pi)\theta)e^{0.5-32.5(1-r)^2}(1-r) \\ \mathrm{u}_r/\mathrm{U}_{\mathrm{bulk}} &= 0 \\ \mathrm{u}_\theta/\mathrm{U}_{\mathrm{bulk}} &= 21.6\sin(12(2\pi)x)e^{-32.4(1-r)^2}(1-r) \end{aligned} \tag{3.11}$$

The radial and azimuthal velocities were mapped back into Nek5000's native rectilinear coordinate system:

$$\mathrm{u}_x = \mathrm{u}_r\cos(\theta) - \mathrm{u}_\theta\sin(\theta)$$

$$\mathrm{u}_y = \mathrm{u}_r\sin(\theta) + \mathrm{u}_\theta\cos(\theta)$$

$$\mathrm{u}_z = \mathrm{u}_s$$

From this initial condition, the $Re_\tau = 170$ simulation was run for 20 flow through

times ($\frac{L}{\mathrm{U}_{bulk}}$) to allow turbulence to become fully developed. After which time was reset, and statistics were gathered for another 20 flow through times. Figure 3.3 illustrates the agreement with well established literature at a similar Reynolds number. For the moderate Reynolds number case, a turbulent solution was mapped to the higher resolution grid and was allowed to develop the new scales of turbulence. This greatly reduced the cost of allowing turbulence to develop from an analytical initial condition.

Turbulent statistics presented are mean flow quantities along with the root mean square and co-variance of single-point fluctuation terms. These quantities arise the the Reynolds Averaged Navier-Stokes (RANS) equations in which Reynolds Decomposition $u_i = \overline{U}_i + u_i'$ is used, where u_i' is the turbulent fluctuation about the mean. The quantities are presented as profiles in the wall normal direction (following the convention that at the wall $y^+ = 0$). Statistics are averaged over time and azimuthal and streamwise directions.

To allow for turbulence to develop more quickly, the turbulent flow field from the lower Reynolds number case was interpolated to the higher resolution grid. From these initial conditions, the average wall shear stress was monitored until the flow ceased accelerating. As with the $Re_\tau = 170$ case, the timer was reset and statistics were gathered for another 20 flow through times. Figure 3.4 shows the validation of the average stresses in the flow.

Good Agreement is observed with other simulations as well as experimental data for both Reynolds numbers indicating that mean first order quantities are well converged indicating that average fluctuations are being well resolved.

This validation is further confirmed when comparing the quadrant analysis of the pipe flow when compared with a similar Reynolds number channel flow as shown in figure 3.5. Normalized by the local total Reynolds Stress ($\langle u_x' u_r' \rangle_{x,\theta,t}$), both the Re_τ170 and 360 case collapse to agreement with turbulent channel data (with slight deviation in the near wall region) from Kim *et al.* (1987) and Brodkey *et al.* (1974). The deviation of Brodkey's data is discussed in both his paper along with Kim's. The difference is attributed to data

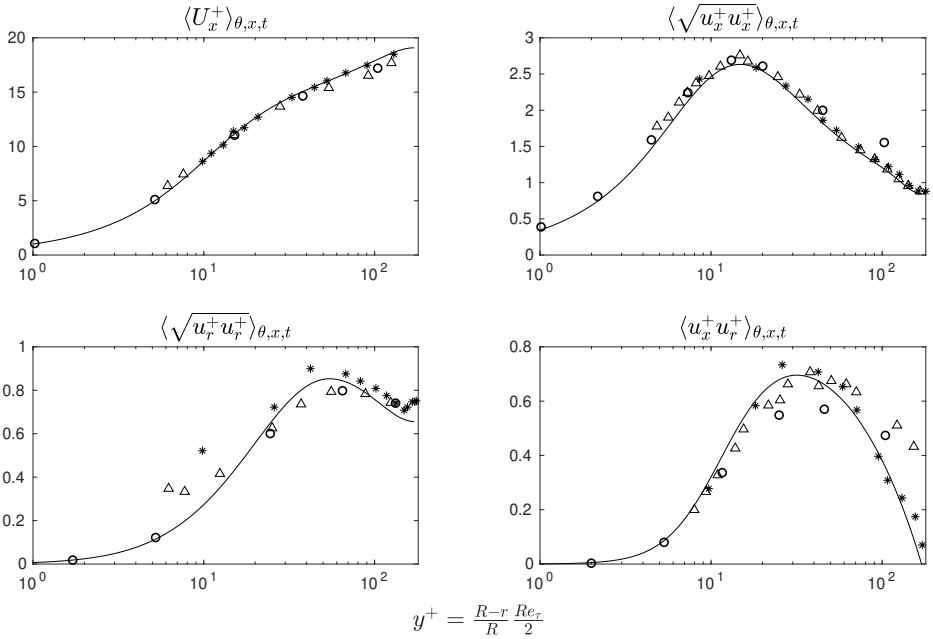

Figure 3.3: Validation of the Average Reynolds Stresses compared with literature − indicates the research presented, ∘ is the work of El Khoury *et al.* (2013), △ comes from the work of Wu and Moin (2008) and ⋆ is the work of Eggels *et al.* (1994). The first two compared data sets are direct numerical simulations at $Re_\tau = 180$ with the former using the same solver Nek5000 and the latter using a 2nd Order Finite Difference Scheme. Good agreement in all the primary stresses can be observed. The work of **?** was a comparison of experimental data to DNS data. Velocity Fluctuations are measured using particle Image Velocimetry

processing and reduction.

Taking u'_x to be the x-axis and $u'_y = -u'_r$ (taken to be negative because a negative radial fluctuation is away from the wall) to be the y-axis the quadrants can be defined as follows:

- $u'_x > 0, u'_y > 0$: Quadrant 1
- $u'_x < 0, u'_y > 0$: Quadrant 2
- $u'_x < 0, u'_y < 0$: Quadrant 3
- $u'_x > 0, u'_y < 0$: Quadrant 4

Quadrants 2 and 4 are the ejection and sweep events respectively, as fluctuations in

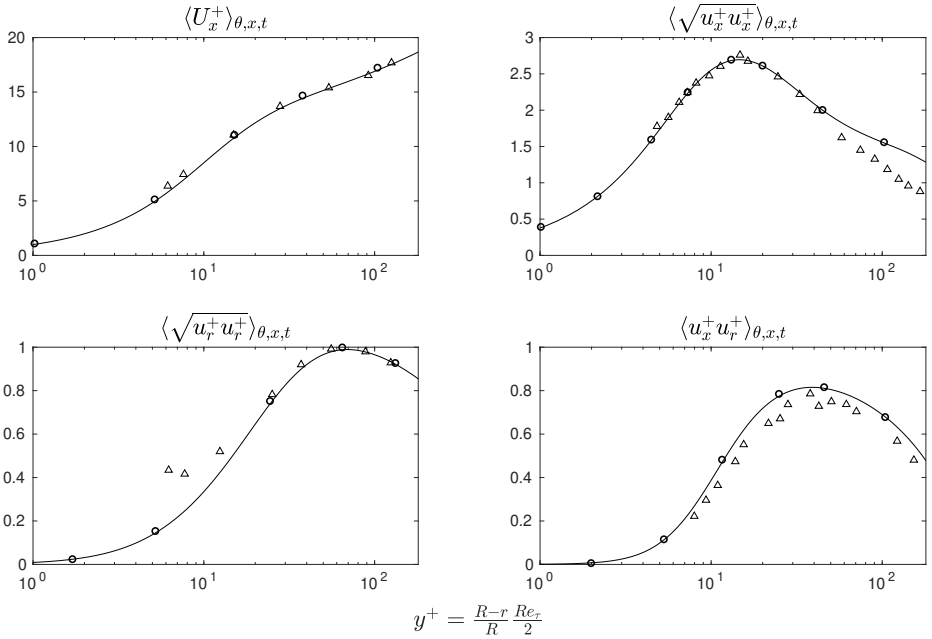

Figure 3.4: Validation of the Average Reynolds Stresses compared with literature − indicates the research presented, ∘ is the work of El Khoury *et al.* (2013) and △ comes from the work of Den Toonder and Nieuwstadt (1997). As before the former of the two is a direct numerical simulation now at $Re_\tau = 360$ the latter is an experimental study at $Re_\tau = 310$ which would explain the slightly decreased stress and smaller magnitude of fluctuations away from the wall.

these quadrants contribute to a negative $u'_x u'_y$ product in Reynolds Stress. The Conditional Average for each can then be considered as

$$\int \int_{Q_i} u'_x u'_y f_{u'_x u'_y} du'_x du'_y = \langle u'_x u'_y | Q_i \rangle_{x,\theta,t} \tag{3.12}$$

Finally, to ensure that gradients are well resolved, The turbulent kinetic energy budget was calculated for both Reynolds number and compared with simulation data available. By virtue of the formulation of the Spectral Element method, the simulation only guarantees that the velocity, pressure, and any passive scalar fields will be continuous and smooth across element boundaries but not necessarily the gradients. It is critical in a direct numerical simulation that the gradients are smooth and continuous because instabilities in the linear region drive the turbulence.

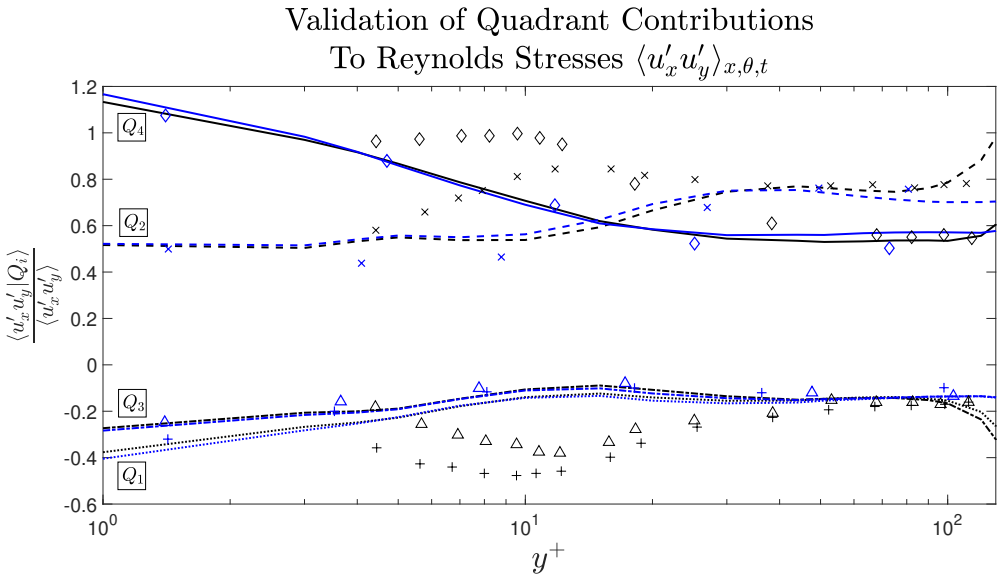

Figure 3.5: Validation of Quadrant Contribution at $Re_\tau = 170$ and 360
·····: Q1 $Re_\tau = 170$; - - -: Q2 $Re_\tau = 170$; -·-·-: Q3 $Re_\tau = 170$; ——: Q4 $Re_\tau = 170$; ·····: Q1 $Re_\tau = 360$; - - -: Q2 $Re_\tau = 360$; -·-·-: Q3 $Re_\tau = 360$; ——: Q4 $Re_\tau = 360$; +: Q1, ◇: Q2, △: Q3, ×: Q4 - Brodkey *et al.* (1974); +: Q1, ◇: Q2, △: Q3, ×: Q4 - Kim *et al.* (1987)
Both Reynolds Numbers show good agreement when collapsed using the local Reynolds Stress $-\langle u'_x u'_r \rangle_{x,\theta,t}$

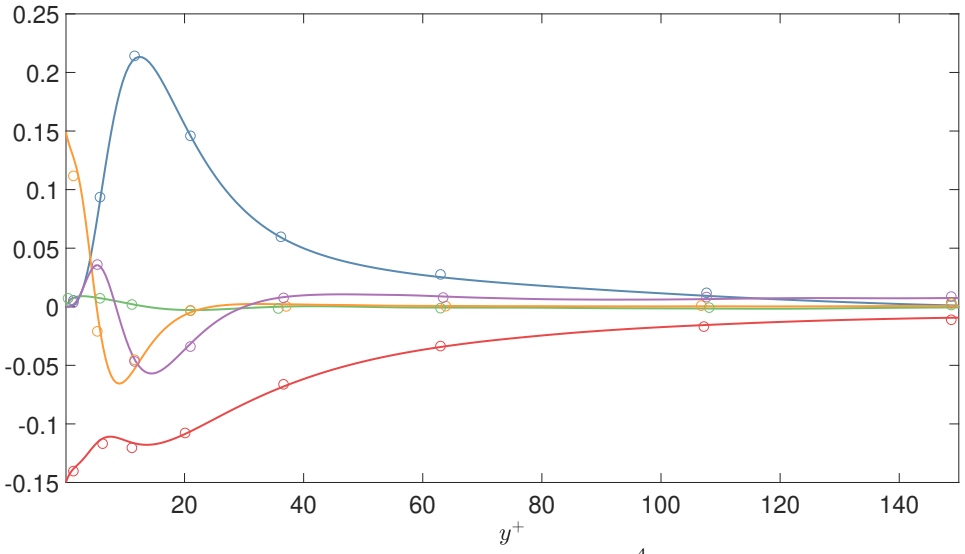

Figure 3.6: Turbulent Budget terms normalized by $\frac{u_\tau^4}{\nu}$ for $Re_\tau = 170$, Lines are from data collected and markers are from El Khoury *et al.* (2013) — Production; — Viscous Dissipation; — Pressure Diffusion; — Viscous Diffusion; — Turbulent Diffusion

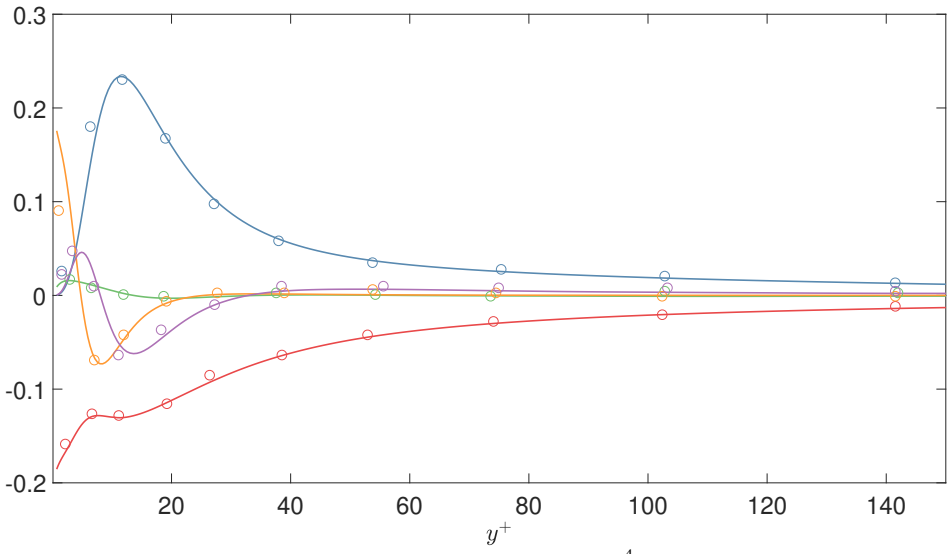

Figure 3.7: Turbulent Budget terms normalized by $\frac{u_\tau^4}{\nu}$ for $Re_\tau = 360$, Lines are from data collected and markers are from El Khoury *et al.* (2013) — Production; — Viscous Dissipation; — Pressure Diffusion; — Viscous Diffusion; — Turbulent Diffusion

Figures 3.6 and 3.7 both show good agreement for all Kinetic Energy terms both in the near wall region and with a decay to zero turbulence production in the wake region of the pipe indicating that gradients and mean turbulent production is in good agreement with literature.

Chapter 4

Temporal Evolution of the Flow from startup to Fully-Developed in the Oscillated Pipe at Both Reynolds Numbers

4.1 Bulk Quantities

Figure 4.1 indicates the development of the volume averaged streamwise velocity as the oscillations are applied. The low reynolds number case indicates an overshoot in which will be explained later. The moderate reynolds number simulation experiences a damped growth over a slightly longer time period. The skin friction coefficient indicates the force necessary to drive with a given amount of kinetic energy. The definitions is given by $C_f = \frac{2\overline{\tau}_{wall}}{\rho \overline{U}^2_{bulk}}$, it can be observed that in the steady-state the skin friction coefficient is reduced by $\approx 26\%$.

A question that needed to be answered was whether or not the initial conditions might

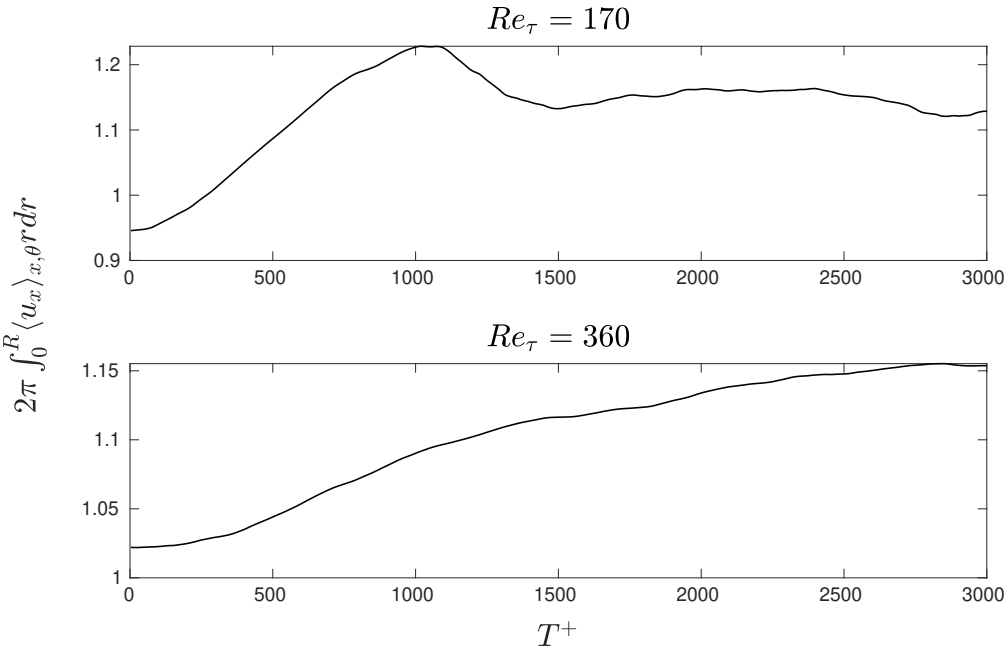

Figure 4.1: Comparison of the bulk mean streamwise velocity in the two pipe from the initialization of the wall oscillations to $30T_{osc}$ or roughly the new steady-state. The low turbulence level in the $Re_\tau = 170$ case (top) results in an over shoot and almost re-laminarization where as the moderate Reynolds number obeys more over-damped dynamics

inflict a bias in the results. In theory there ought to be no bias given that the sinusoidal forcing of the wall has zero mean. However, given the abrupt application of wall oscillations it is necessary to convince oneself that any transients have decayed to zero. Furthermore, a determination of sampling frequency of the phase averaging was necessary to be determined.

To achieve this end, spatial averaging in both the azimuthal and streamwise direction was applied to show such a decay over time of the transient bias in the flow. Of most importance here is to observe if there exists a net angular momentum in the velocity field characterized by a non-zero azimuthal velocity when averaged in the azimuthal direction and integrated in the radial direction. Figure 4.2 shows a development of the angular momentum in the domain. The behavior here indicates an overall zero net torque in the long time average, however phase to phase variation shows that the wall oscillations are imparting significant

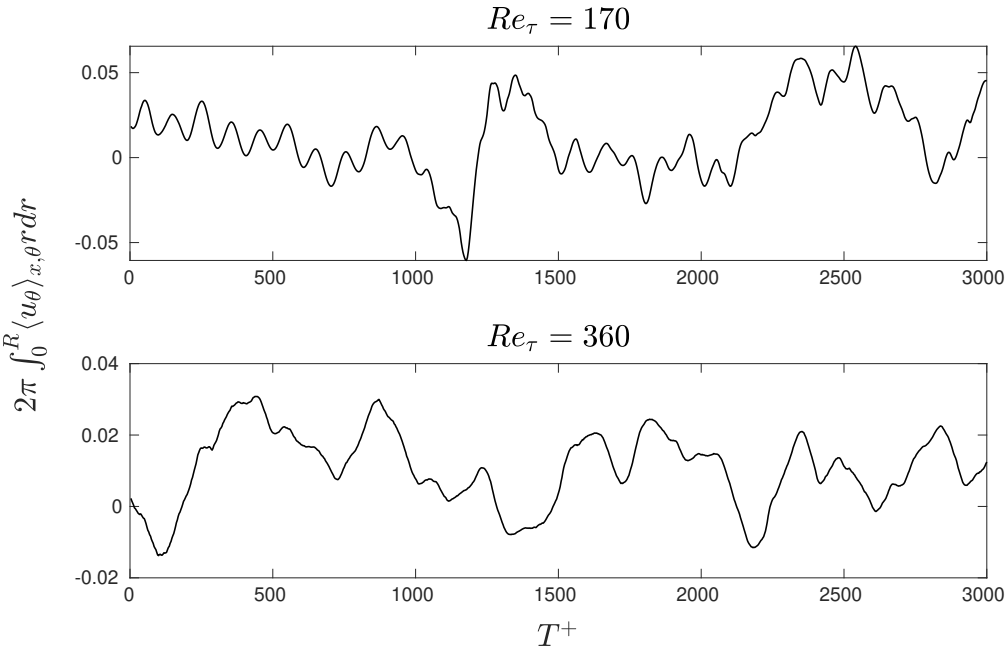

Figure 4.2: Development of the net angular momentum averaged in the streamwise and azimuthal direction integrated to over the radial direction as a function of time. Normalized by the non-oscillated friction velocity. Sinusoidal but otherwise zero mean temporal profile indicates that the wall oscillations do not impart a net torque on the flow despite the bias towards an initially positive wall velocity.

energy into the domain. Taking note of the lack of visible wall oscillations imposed on the mean angular momentum on the moderate Reynolds number flow is likely due to the increased domain size relative to the region which the wall oscillation effects.

Figures 4.3 and 4.4 contour the azimuthally and streamwise averaged azimuthal velocity as a function of wall distance y^+. Both low and moderate Reynolds number flows experience a stokes layer solution below $y^+ = 25.4$ (the stokes layer height). The result of this is that all near wall structures, particularly quasi-streamwise vorticity, will experience a modulation due to the imposed wall velocity.

Figures 4.5 and 4.6 contour the azimuthally and streamiwse averaged streamwise velocity as it develops from the standard pipe to the oscillated pipe

Figures 4.3 through 4.6 indicate why phase averaging is necessary. At locations $y^+ < 30$

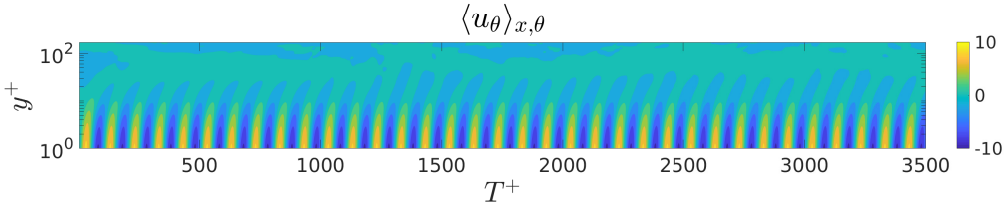

Figure 4.3: Contour of the streamwise-azimuthal average of the azimuthal velocity component from start-up to steady-state at $Re_\tau = 170$. Above $y^+ = 30$ the flow becomes invariant of wall oscillations but the flow below can be observed to respond almost immediately to the oscillations. Additionally, the flow obeys a stokes layer solution below the stokes layer

show a deterministic oscillation that follows the wall oscillation frequency for the azimuthal velocity and a doubling of the wall oscillation frequency for the streamwise component. Ignoring such an oscillation would result in over prediction of turbulent RMS quantities.

If one were to naively average over a long period of time two phenomenon would appear in the flow: 1) a bias in mean velocity quantities as a result of not considering the averaging time as a function of oscillation period and 2) an superposition of an RMS fluctuation as a result of the deterministic sinusoid imposed at the boundaries. One would not be observing the true nature of the turbulence.

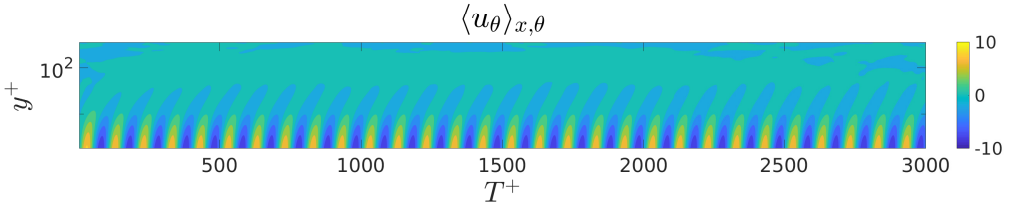

Figure 4.4: Contour of the streamwise-azimuthal average of the azimuthal velocity component from start-up to steady-stateat $Re_\tau = 360$. Above $y^+ = 30$ the flow becomes invariant of wall oscillations but the flow below can be observed to respond almost immediately to the oscillations. Additionally, the flow obeys a stokes layer solution below the stokes layer. The dynamics are identical to figure 4.3

4.1.1 Development of the Reynolds Shear Stress $\langle u'_x u'_r \rangle_{x,\theta}$

Presented is the streamwise-azimuthal average of the Reynolds Shear Stress, $\langle u'_x u'_r \rangle_{x,\theta}$. The following figures illustrate the decay and regeneration of drag enhancing turbulence in the domain. The fluctuations are normalized the standard pipe friction velocity to illustrate the relative change.

Figures 4.8 and 4.9 illustrate the development of the Reynolds Stress as function of time and wall coordinate. Remarkably, immediately after wall oscillations the flow is characterized by low Mean reynolds stress, however this is only temporary and the flow redevelops to a full turbulent, albeit with reduced streamwise-radial fluctuation state.

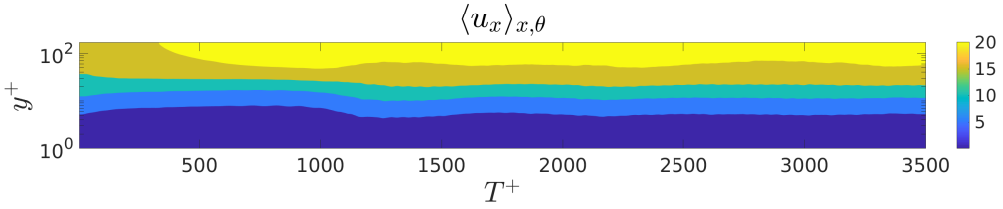

Figure 4.5: Contour of the streamwise-azimuthal average of the streamwise velocity component from start-up to steady-state at $Re_\tau = 170$. The major effect observed is the extension of the linear region further from the wall allowing for the outer region to be shifted up by roughly $3.5u_\tau$ (see figure 5.2)

4.1.2 Startup Velocity Fluctuations

In this section contour maps of the velocity fluctuations are presented. Due to the nature of temporal evolution, the fluctuation is defined to be $u' = u - \langle u \rangle_{x,\theta}$, that is the instantaneous velocity minus the average over the streamwise and azimuthal directions. Discussion of the development of the structures is provided at key times noted in the previous section. Particularly, the initial conditions, minimum (and maximum for $Re_\tau = 170$) drag, and the new steady-state are the snapshots of interest.

Notably, in figure 4.5 there is a period of relatively high streamwise velocity at $10T_{osc}$. Visualizing the field at this time 4.11 and comparing with the initial level of turbulence 4.10. The fluctuations are highly diminished. This same phenomenon was not observed at the moderate Reynolds number case, likely due to the much stronger levels of turbulence.

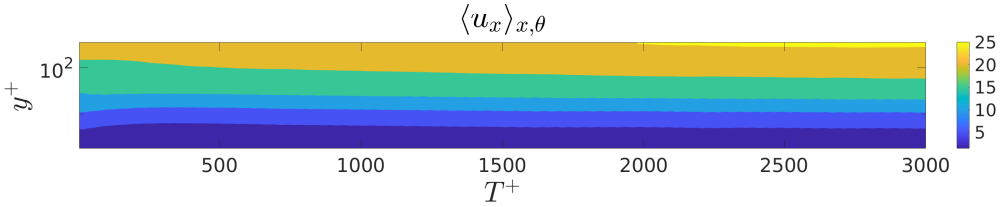

Figure 4.6: Contour of the streamwise-azimuthal average of the streamwise velocity component from start-up to steady-state at $Re_\tau = 360$. Dynamics are similar to $Re_\tau = 170$ (figure 4.5) where the high speed region can be seen to extend further down towards the wall. This is a result of the linear region extending further away from the wall (see figure 5.2)

Finally, $2000t^+$ after startup figure 4.12 illustrates the turbulence in the low reynolds number pipe flow. A "cloud" of turbulence can be observed in the unwrapped pipe angled in an anti-clockwise direction. The structures are transient and reverse directions given a long enough time span.

$Re_\tau = 170$

$Re_\tau = 360$

4.1.3 Startup Vorticity Fluctuations

Presented are the streamwise vorticity fluctuations at various y^+ coordinates. Fluctuations are defined as the instantaneous minus the streamwise-azimuthal average.

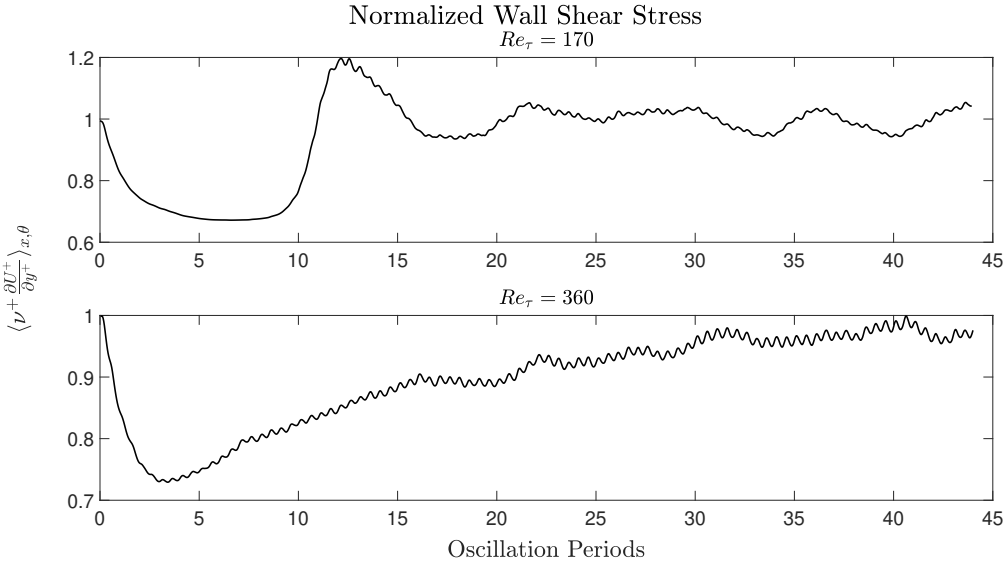

Figure 4.7: Streamwise-azimuthal average wall velocity gradient in inner units shows the behavior of the flow to initially drop to $\approx 70\%$ of standard pipe and then climb as structures reorganize. In the low Reynolds number case, this is visualized in figure 4.15 where turbulent spots can be seen to almost disappear in the near wall region. Similarly figure 4.19 shows that this behavior is similar however the extent to which is not nearly as drastic despite the similarity in initial drag reduction

$Re_\tau = 170$

At the linear and buffer layer locations ($y^+ = 10, 30$) there are long streaky streamwise vortical structures. These are associated with the legs of the hairpins which act as pumps for ejecting fluid away from the wall. The initial vorticity fluctuations can be observed to obey this behavior (figures 4.14 and 4.14). At $625t^+$ (figure 4.15) the vorticity is observed to be very minimal. This behavior is only transient but it illuminates how disruption of the near wall vortical structures has a drastic effect on the whole flow region.

Figure 4.17 illustrates the new steady-state behavior. Like in the velocity fluctuations a helical structure can be observed in the alignment of the streamwise packets. Additionally, the packets of vorticity below the stokes layer respond directly to the wall oscillations showing small scale oscillations that track the azimuthal velocity.

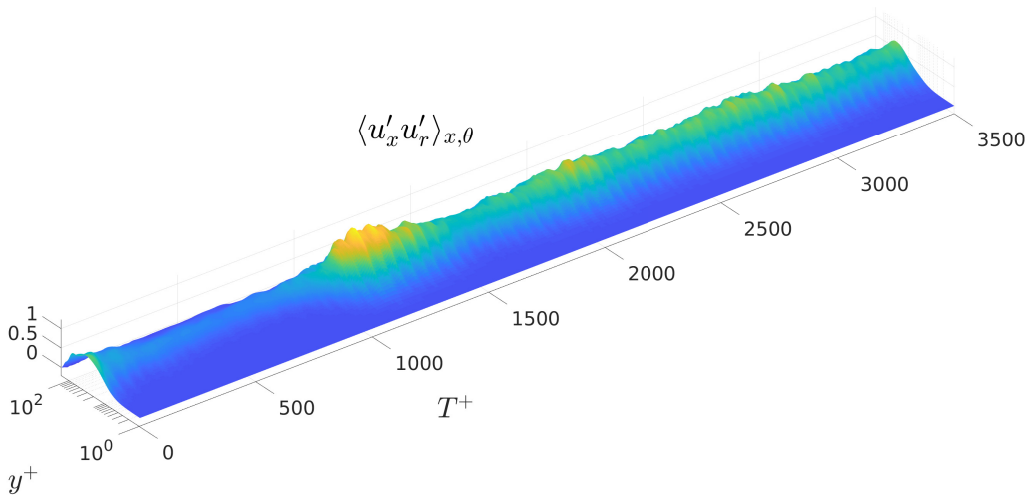

Figure 4.8: Development of the $\langle u'_x u'_r \rangle_{x,\theta}$ component of Reynolds Stress in the low Reynolds ($Re_\tau = 170$) number pipe flow . The flow appears to re-laminarize for approximately $400t^+$ and then redevelops its turbulence. The new steady-state is reached $\approx 2500t^+$ after the oscillations start

$Re_\tau = 360$

Dynamics oserved are similar to the low reynolds number case. However, the wall drag period does not have nearly as reduced turbulence (figure 4.19). The near quiescent field at the low Reynolds number is likely just a Reynolds number effect. However, all other dynamics are similar. Below the Stokes' layer the vorticity packets oscillate with the wall and helical structures can be observed (figures 4.20 4.21).

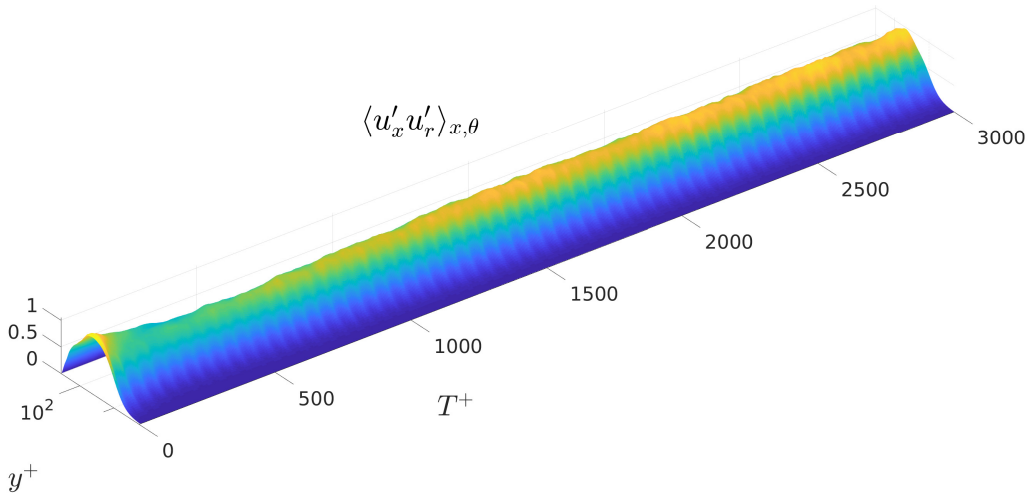

Figure 4.9: Development of the $\langle u'_x u'_r \rangle_{x,\theta}$ component of Reynolds Stress in the moderate Reynolds ($Re_\tau = 360$) number pipe flow. Like the low Reynolds number flow, for approximately $400t^+$ the flow behaves as a very low mean Reynolds Stress and then redevelops its turbulence. The new steady-state is reached $\approx 2500t^+$ after the oscillations start

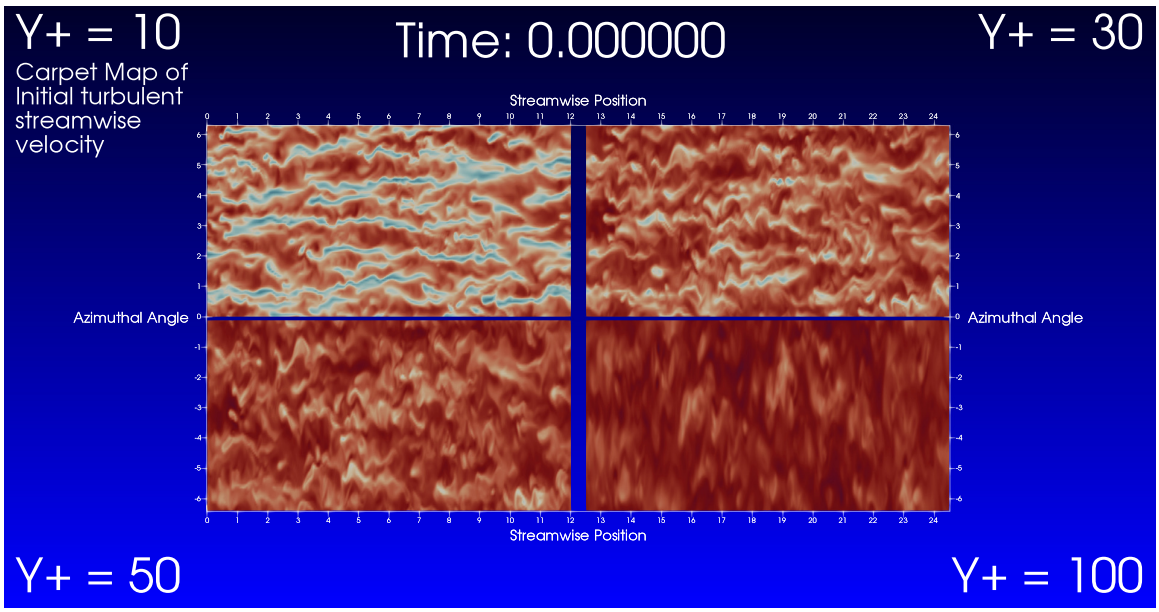

Figure 4.10: Initial turbulent streamwise velocity fluctuations in the Oscillated pipe at $Re_\tau = 170$. Characteristic of wall bounded turbulence, long streaky structures are observed in the linear region of the flow

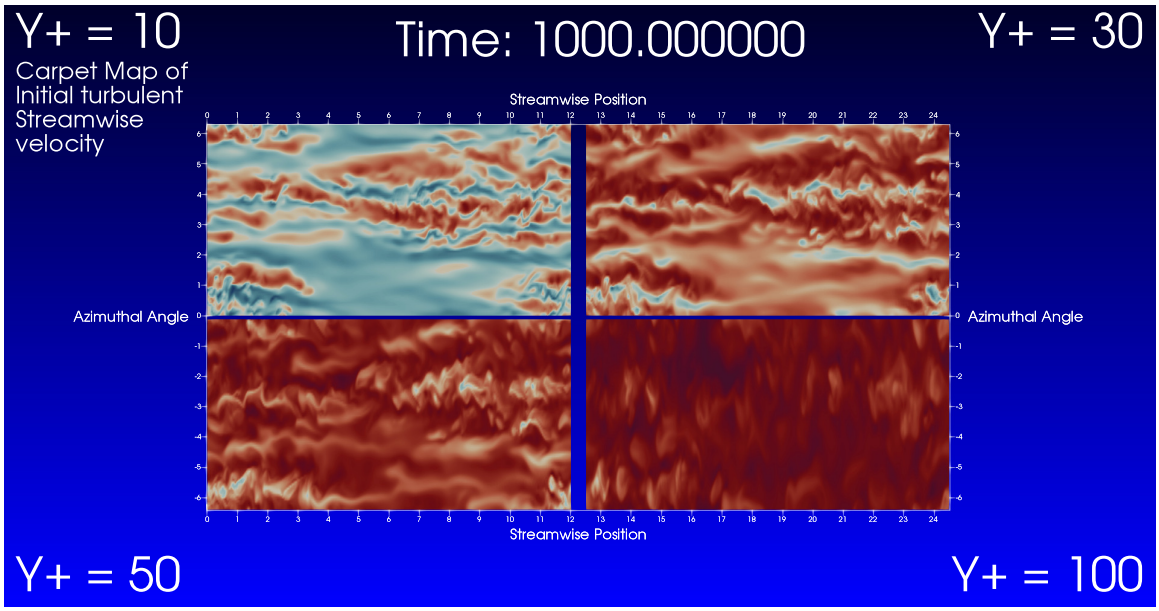

Figure 4.11: Visualization of the instantaneous Streamwise velocity in the oscillated pipe $10T_{osc}$ after initializing the boundary modification. At this time a peak in $\langle u_x \rangle_{x,\theta}$ component of velocity is observed and this shows in the observation that turbulent spots are are almost non-existent in the linear region of the flow

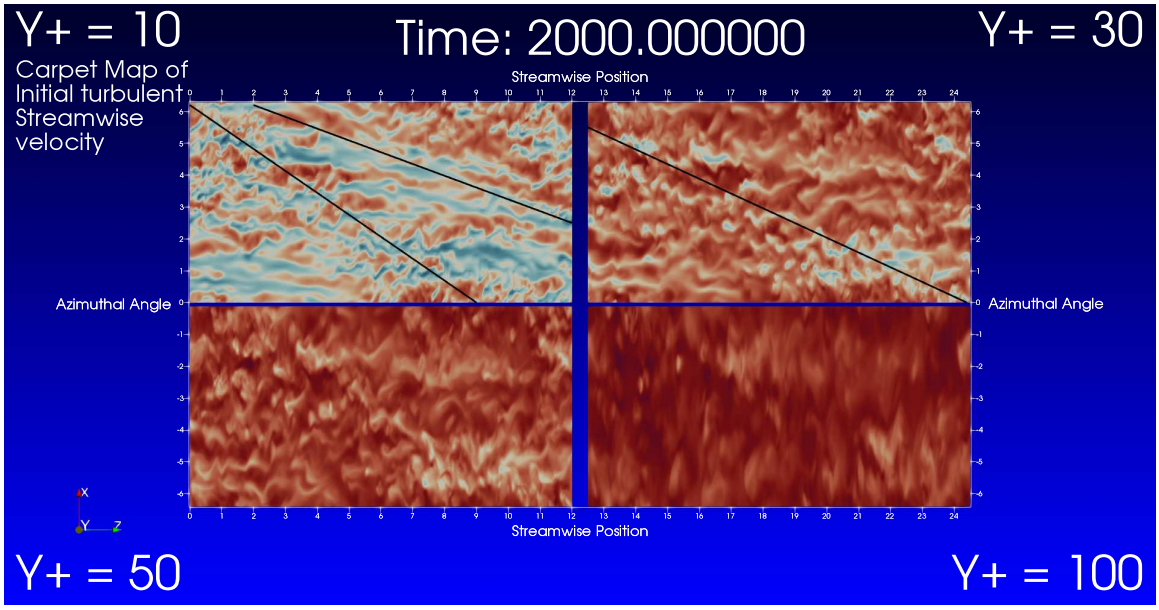

Figure 4.12: Visualization of the instantaneous streamwise velocity in the oscillated pipe $20T_{osc}$ after initializing the boundary modification ($Re_\tau = 170$). Clouds of streamwise velocity can be seen to be cohering in a helical pattern around the pipe as indicated by the black lines

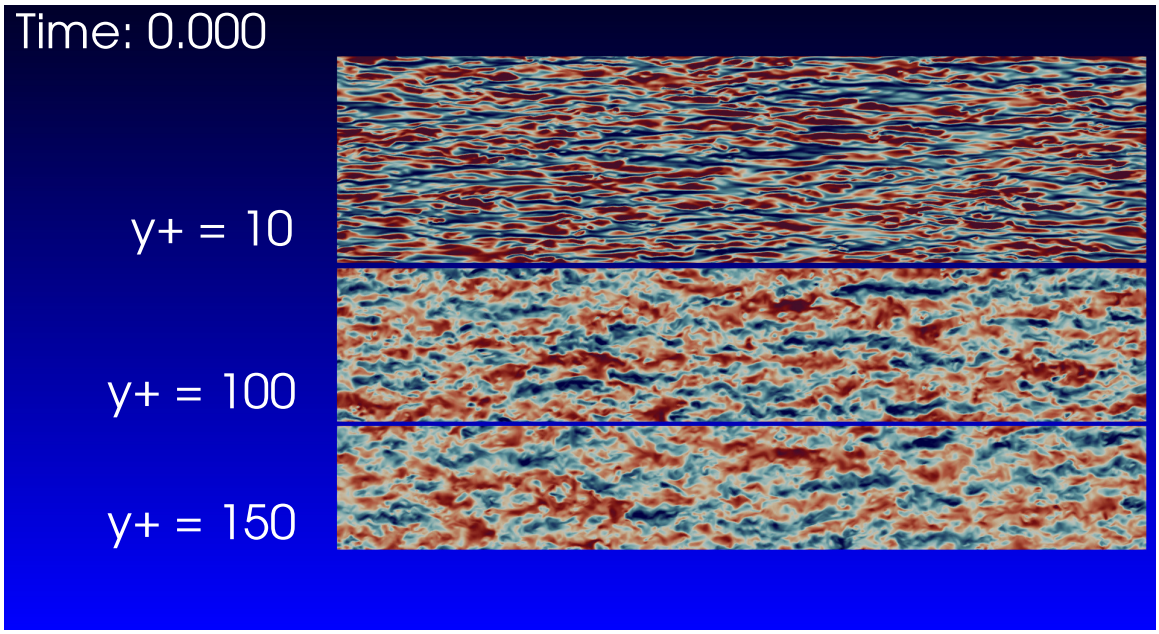

Figure 4.13: Initial Streamwise velocity fluctuation field (given by $u'_x = u_x - \langle u_x \rangle_{x,\theta}$) in the Oscillated pipe at $Re_\tau = 170$. Characteristic of wall bounded turbulence, long streaky structures are observed in the linear region of the flow associated with the streaky structures shown in figure 4.10. From top to bottom $y^+ = 10, 30, 50$

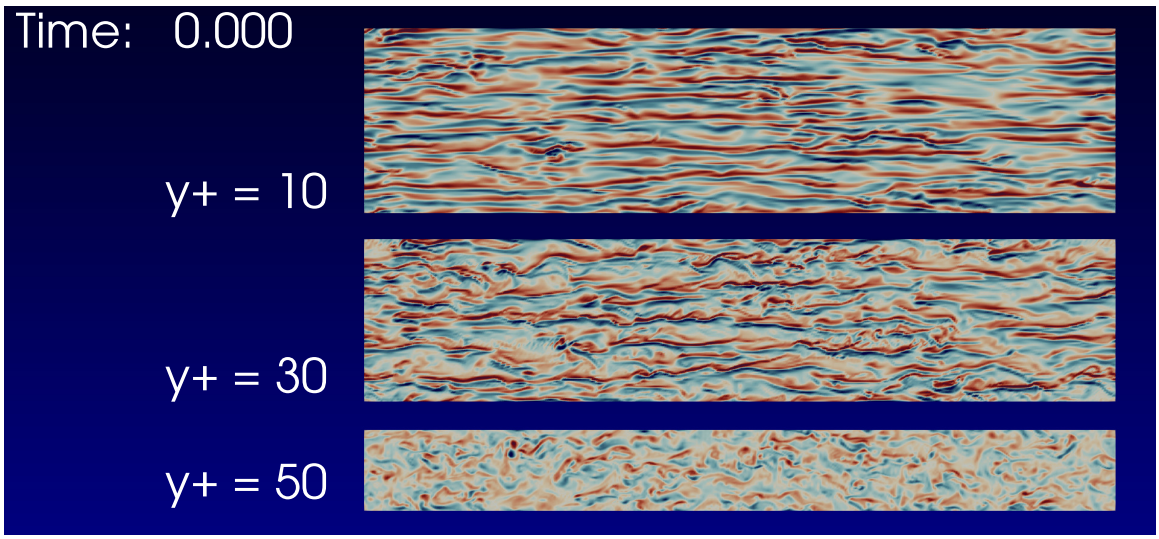

Figure 4.14: Initial Vorticity field in the Oscillated pipe at $Re_\tau = 170$. Characteristic of wall bounded turbulence, long streaky structures are observed in the linear region of the flow associated with the streaky structures shown in figure 4.10. From top to bottom $y^+ = 10, 30, 50$

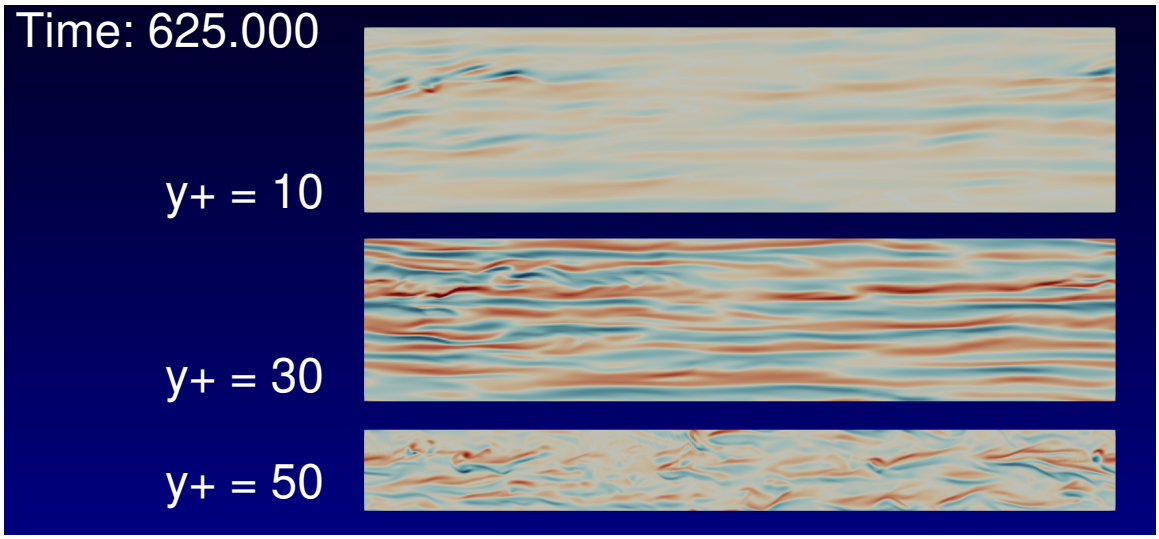

Figure 4.15: Vorticity fluctuations in the oscillated pipe $6.25T_{osc}$ after initializing the boundary modification. At this point the vorticity in the near wall is minimized and corresponds with the low drag seen in figure 4.7. Streamwise vorticity is reduced to just a few turbulent spots

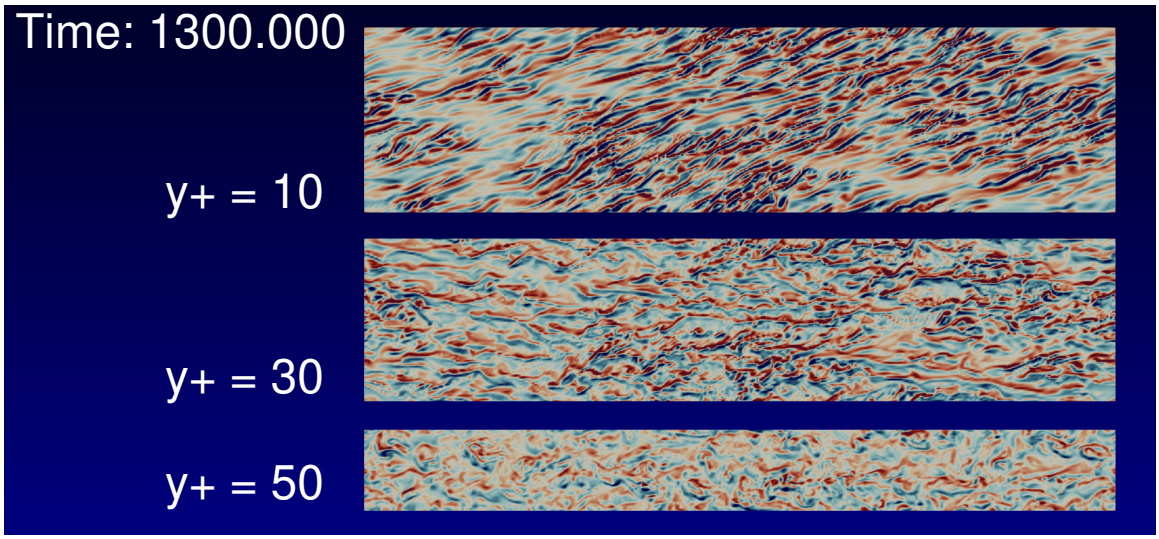

Figure 4.16: Vorticity fluctuations in the oscillated pipe at $Re_\tau = 170$ and $13T_{osc}$ after initializing the boundary modification. At this point the vorticity in the near wall is maximized and corresponds with the high drag seen in figure 4.7. Streamwise vorticity does not, however, cohere in the way that the standard pipe does. Long streaky structures are no where to be found and can be seen to correlate to the wall oscillations

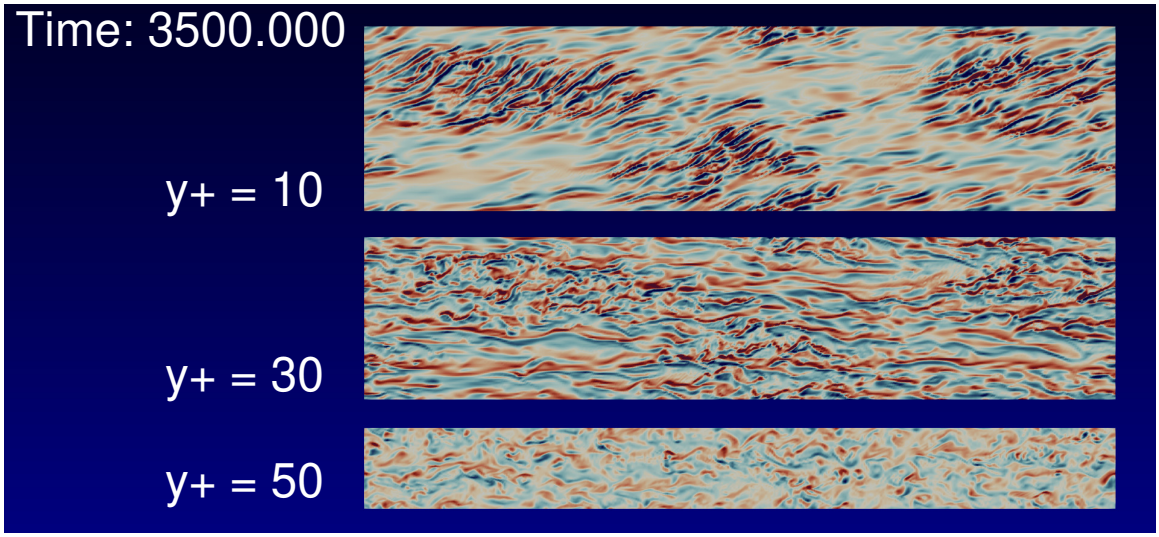

Figure 4.17: Vorticity flucuations in the oscillated pipe at $Re_\tau = 170$ and $35T_{osc}$ after initializing the boundary modification. At this point the vorticity in the near wall can be assumed to to have reached its new steady-state. It can be observed here as in figure 4.12 that the turbulent spots tend to align and cohere in a helical fashion. This

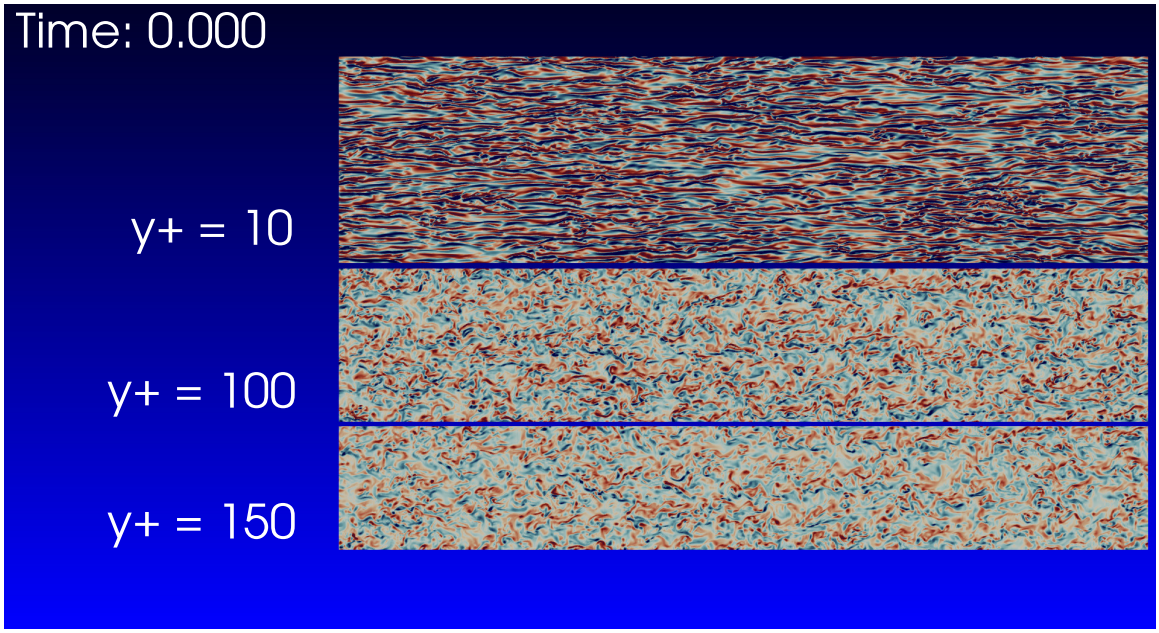

Figure 4.18: Initial Vorticity field in the Oscillated pipe at $Re_\tau = 360$. Characteristic of wall bounded turbulence, long streaky structures are observed in the linear region of the flow associated with the streaky structures shown in figure 4.13. From top to bottom $y^+ = 10, 100, 150$

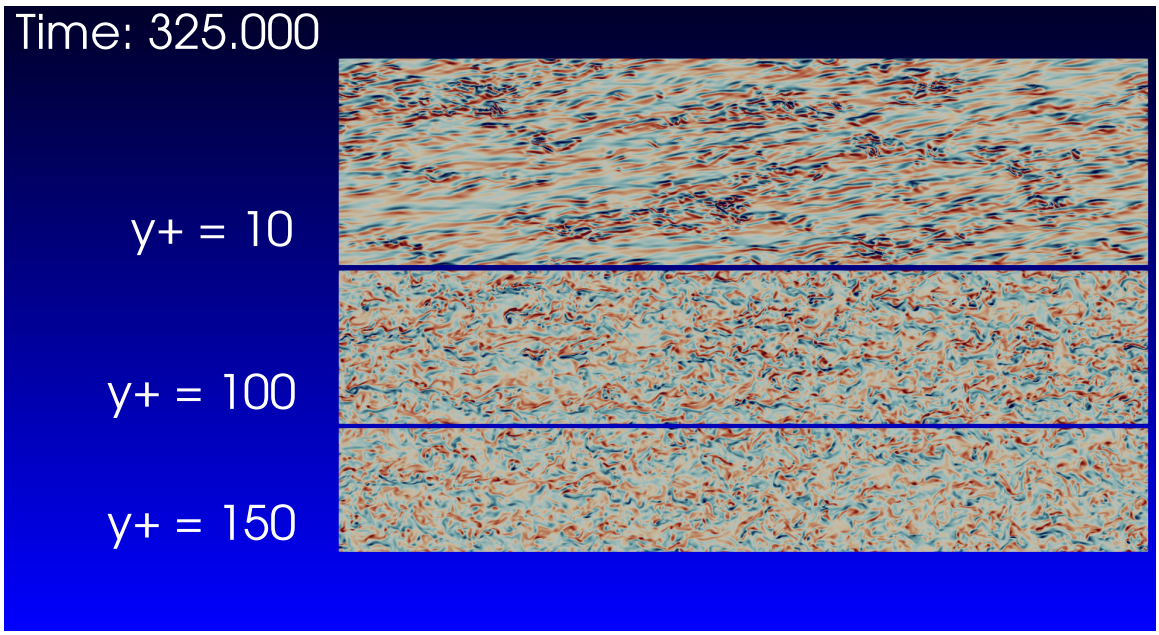

Figure 4.19: Vorticity field in the Oscillated pipe at $Re_\tau = 360$ after $3.25T_{osc}$. This time corresponds to roughly the minimum drag as shown in figure 4.7. In contrast with the low Reynolds number flow, the streaky structures are not nearly as attenuated. However, the decay of streamwise vorticity about the field is observable. From top to bottom $y^+ = 10, 100, 150$

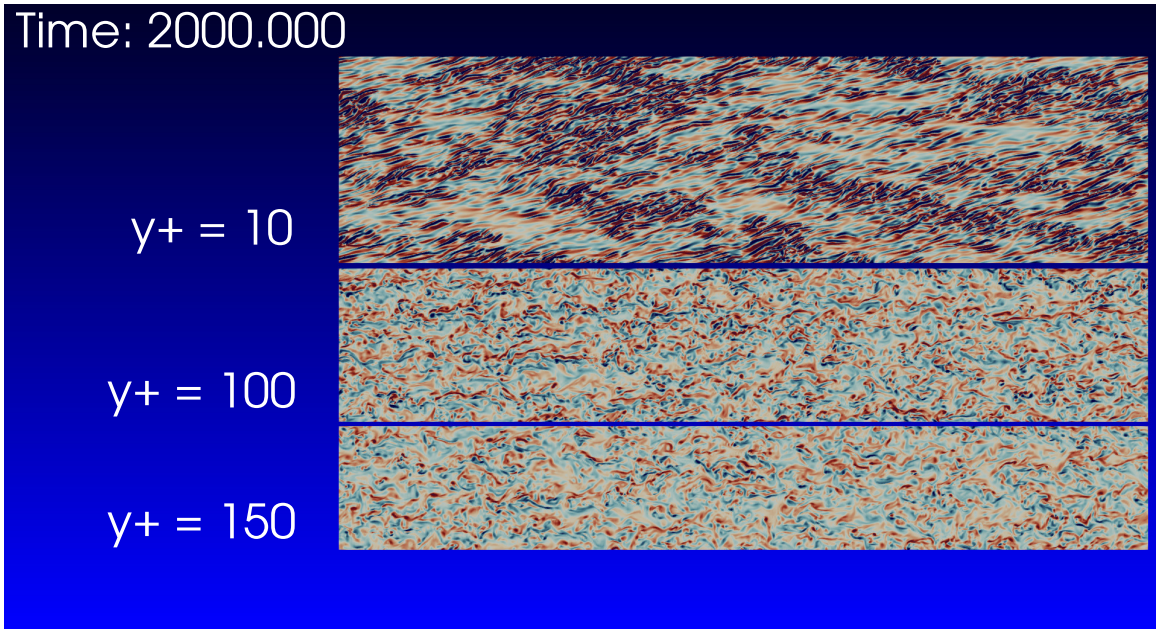

Figure 4.20: Vorticity fluctation field in the Oscillated pipe at $Re_\tau = 360$ after $20T_{osc}$. Contrasting with the low Reynolds pipe flow there is no observable overshoot in the drag. This is likely due to the higher levels of turbulence acting as a damper against the over-acceleration of the fluid. From top to bottom $y^+ = 10, 100, 150$

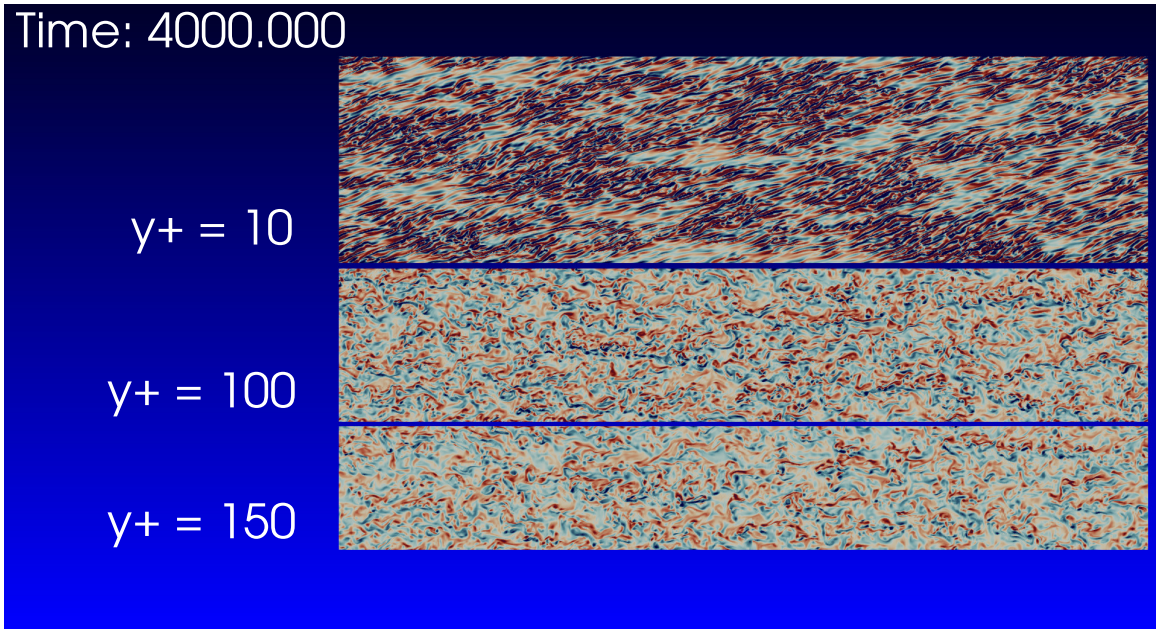

Figure 4.21: Fluctuating Vorticity field in the Oscillated pipe at $Re_\tau = 360$ after $40T_{osc}$. Wall oscillations have modified the streamwise vorticity to be inclined with the wall oscillation. From top to bottom $y^+ = 10, 100, 150$

Chapter 5

Comparison of Standard and Oscillated Pipe Fully Developed Statistics at $Re_\tau = 170$ and 360

In this chapter the effects of periodic oscillations on fully developed flow is investigated by comparing the mean velocities, select Reynolds Stresses and Energy budgets of the turbulence in the standard pipe to those in the oscillated pipe. The oscillated pipe presents two averages: $\langle Q \rangle_{\theta,x,t}$ and conditional averages given the phase $\langle Q|\phi(t)\rangle_{\theta,x,t}$. The ϕ average is found by ensemble averageing samples taken at the same phase angle over many cycles. The average over all time is then the concatenation of these phase averages.

In periodic flows, it is not clear the Reynolds' decomposition provides the best decomposition of the flow because the fluctuation $u_i' = u_i - \overline{u_i}$ contains a periodic time varying component associated with the oscillation. This can be removed by defined a fluctuation about the phase conditioned average instead of the long term average:

$$u_i'' = u_i = \langle u_i|\phi(t)\rangle = u_i' - \langle (u_i - \overline{u_i})|\phi\rangle \tag{5.1}$$

All fluctuations in the following section for the oscillated pipe use the definition given by equation 5.1. For simplicity we shall denote u_i'' as u_i^+

5.1 Mean Velocities and Reynolds Stresses

The following sections illustrates similarities of effect on statistics of the two Reynolds numbers when normalized by the proper quanities. Furthermore, differences are shown between the non-oscillated and oscillated cases for each Reynolds number. The effects of wall oscillations on the turbulent stresses are shown to

Presented are the Reynolds stresses that characterize the turbulence in terms of first and second order moments of velocity. Figure 5.1 and 5.2 illustrate the mean change in the Reynolds stresses as a result of the wall oscillations. The effects of drag reduction are marked by the increased flow rate illustrated by the shift upwards of the log layer by $3.5u_\tau$ starting from $y^+ > 35$ in both simulations. This is coupled with a decrease in root mean square streamwise (RMS) fluctuations between $y^+ > 1$ and $y^+ < 30$ and mean square radial fluctuations between $y^+ > 20$ and $y^+ < 100$. The reduction of the radial fluctuations is apparent despite the boundary modifications being contained to a region below $y^+ = 25$ (as evidenced by the stokes layer solution of azimuthal velocity) the effects on turbulent fluctuations extends well into the log region of the flow. This observation is further enforced with the RMS of streamwise fluctuations which show reduction all the way to twice the stokes layer height ($y^+ = 50$).

As with the total time averages, the phase to phase behavior of the main Reynolds Stresses is nearly indistinguishable (between the two reynolds numbers) by profile when normalized by wall shear and vary only in magnitude. Notably, just below $y^+ = 10$ is the

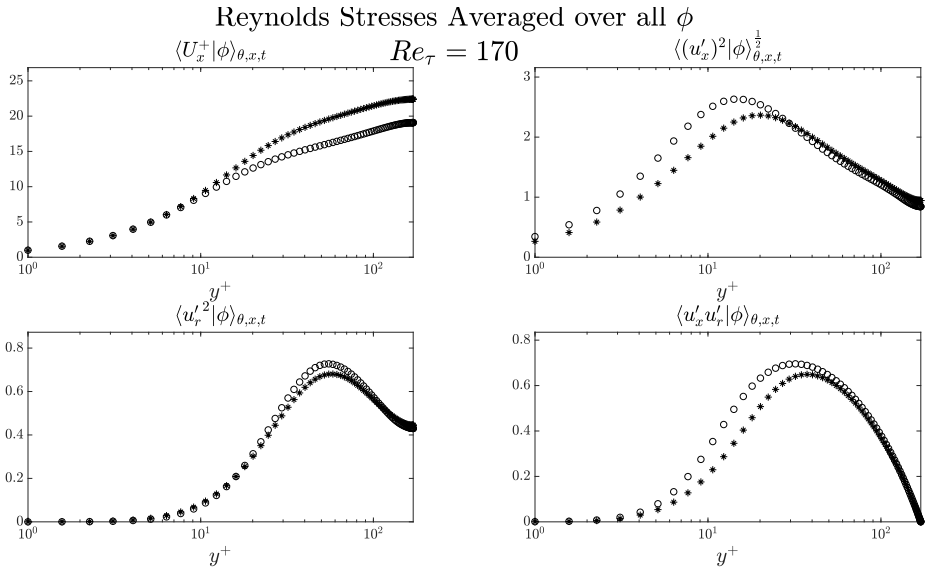

Figure 5.1: Single Point statistics averaged over all time for the $Re_\tau = 170$ simulation $*$: Oscillated Pipe; $\circ$: standard pipe. Marked changes in the Streamwise velocity profile show shift up in the log layer indicating an increased flow rate. This is coupled with a decreased RMS streamwise velocity fluctuation along with a decreased mean squared radial fluctuation at higher y^+ coordinates. This is indicative of a change in the dynamics of Q2/Q4 events which will be presented later

oscillatory behavior as a function of phase despite the azimuthal velocity not appearing in the term for $\langle u_x' u_r' \rangle$ itself. However, analyzing the transport equation indicates that the spanwise velocity has the effect of reducing the rate of streamwise-radial fluctuation transport. In particular this has the effect of moving the location of peak reynolds stress up and down, albeit very slightly.

Furthermore, despite the subtraction of phase velocities, there is still a distinct periodicity in the behavior of the Reynolds Stresses below the stokes layer. This is indicative of a fundamental change in the nature of the turbulence which was assumed to have a behavior that appeared much like 2.1 where by phase averaging the turbulent fluctuations without a sinusoidal bias can be isolated. This indicates that despite being uncorrelated as shown in Hussain and Reynolds (1970), the wall oscillations are modifying the statistical distribution of the fluctuating quantities.

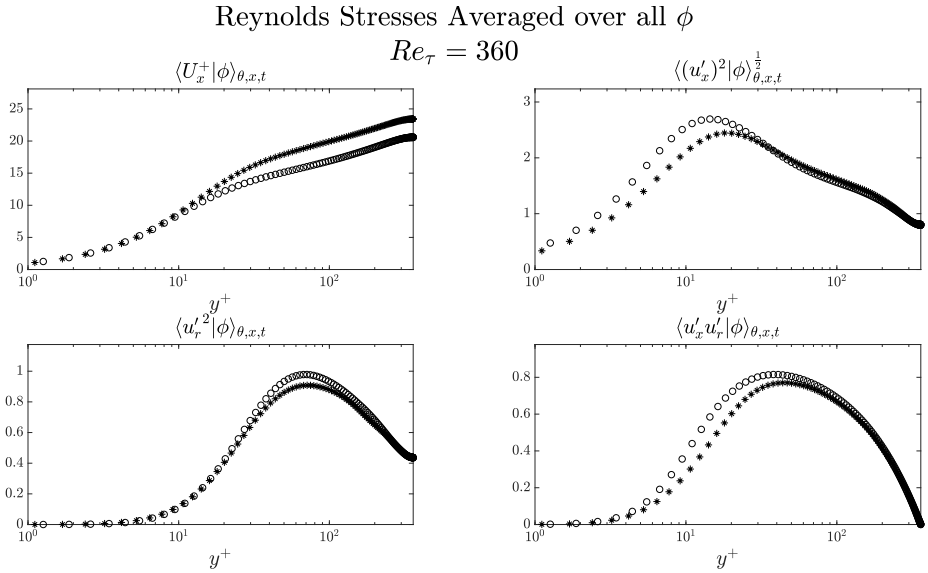

Figure 5.2: Single Points averaged over all homogeneous coordinates for $Re_\tau = 360$ simulation $*$: Oscillated Pipe; $\circ$: standard pipe. Marked changes in the Streamwise velocity profile show shift up in the log layer indicating an increased flow rate. Trends are similar to that of the lower Reynolds number case with a constant displacement of the mean streamwise velocity, decrease in streamwise and radial fluctuations and decrease in streamwise-radial fluctuations

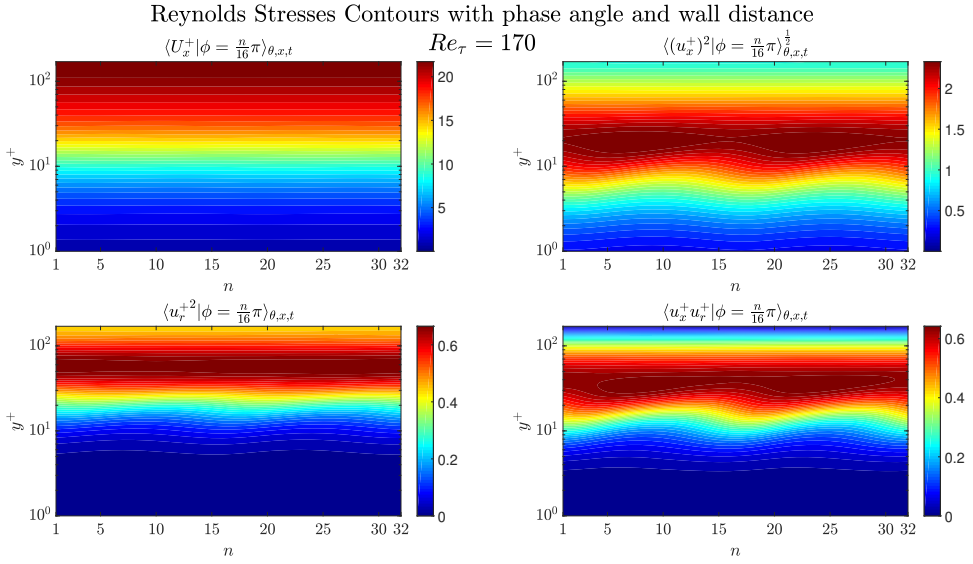

Figure 5.3: Contours of the Reynolds stresses as a function of wall oscillation phase for $Re_\tau = 170$. At low $y+$ levels modifications to the mean can be oberserved as a function of phase. This is indicative of a coupling of the streamwise and radial fluctuations to the phases despite their geometric orthogonality. A fundamental change in turbulence has occured

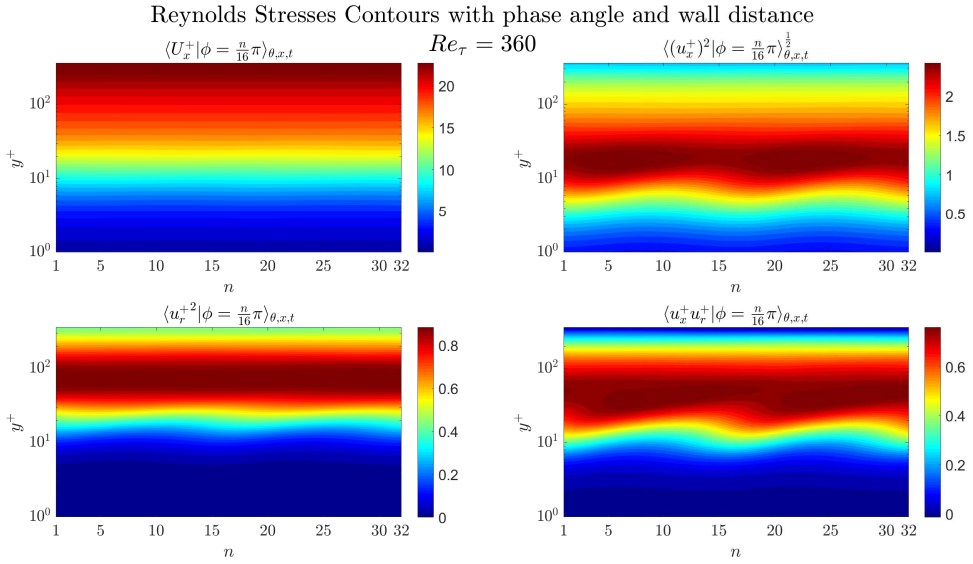

Figure 5.4: Contours of the Reynolds stresses as a function of wall oscillation phase for $Re_\tau = 360$. As in the low Reynolds number flow, the near wall mean turbulent fluctuations vary periodically indicating a change in behavior in the region where streamwise vorticity lies

5.2 Quadrant Analysis

Observing only the mean Reynolds Stress does not indicate well what is occurring with the turbulence; only whether or not the mean stress producing fluctuations are reduced. To further quantify what is happening to the turbulence between the two pipes a conditional average of the fluctuations is taken such that the fluctuation are in given quadrant of the (u'_x, u'_r) plane.

Using equation 3.12 and normalizing by mean wall shear stress yields figures 5.5 and 5.6. Normalization by total average wall shear stress is used rather than local Reynolds Stress because the average wall shear is constant between the two simulations and does a better job of illuminating how the turbulence is changing.

Figures 5.5 and 5.6 show the dynamics of the quadrant average Reynolds Stress contribution. It can be conclusively determined that the effects are *not* to increase the Q1/Q3

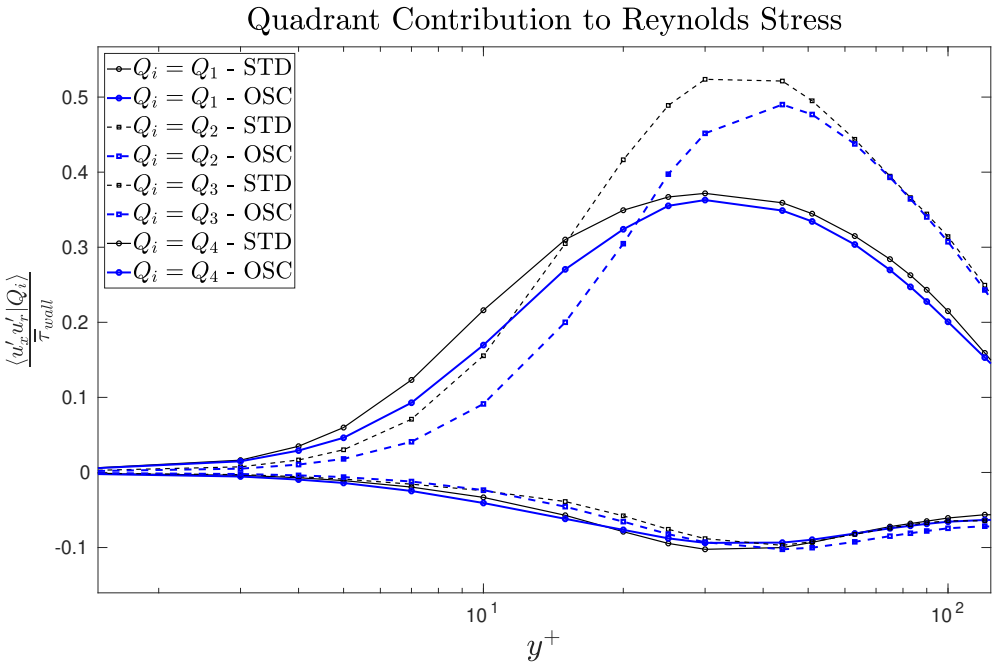

Figure 5.5: $Re_\tau = 170$, black Lines indicate Standard Pipe and blue lines Oscillated Pipe,
$-\langle u_x' u_r' \rangle > 0$
-⊡- - Q2 Standard Pipe -⊡- Q2 Oscillated Pipe —⊙— Q4 Standard Pipe —⊙— Q4 Oscillated Pipe
$-\langle u_x' u_r' \rangle < 0$
—⊙— Q1 Standard Pipe —⊙— Q1 Oscillated Pipe -⊡- Q3 Standard Pipe -⊡- Q3 Oscillated Pipe

events but instead to interrupt the mechanism of ejection and sweep events. This can be seen by the grossly reduced Q2/Q4 contributions of to the Reynolds stress starting all the way from $y^+ = 1$ and all the way up to roughly $y^+ = 60$. This is in spite of the fact that the stokes layer was previously shown to end around $y^+ = 25$ as predicted by laminar solutions to an oscillated wall.

Most notably is the effect of reducing Q2 events and shifting the intersection of Q4 to Q2 dominant events outwards from $y^+ \approx 15$ to $y^+ = 21$. This is indicative of suppression of ejection events. However, Q4 events remain relatively unaffected though there is some suppression both below $y^+ = 10$ and above $y^+ = 30$.

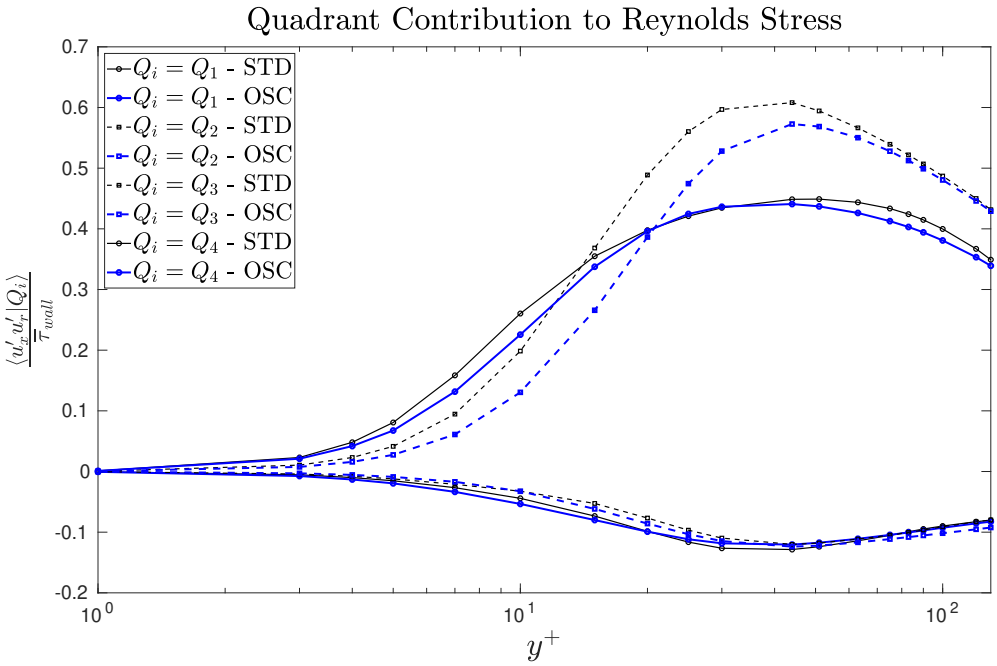

Figure 5.6: $Re_\tau = 360$, black Lines indicate Standard Pipe and blue lines Oscillated Pipe,
$-\langle u_x' u_r' \rangle > 0$
-⊡- Q2 Standard Pipe -⊡- Q2 Oscillated Pipe —○— Q4 Standard Pipe —○— Q4 Oscillated Pipe
$-\langle u_x' u_r' \rangle < 0$
—○— Q1 Standard Pipe —○— Q1 Oscillated Pipe -⊡- Q3 Standard Pipe -⊡- Q3 Oscillated Pipe

5.3 Turbulent Kinetic Energy Budget

In order to begin answering why the quadrant 2 and 4 energy is decreased, it is necessary to observe the effects on overall turbulence and its transport in the pipe. Turbulent Kinetic Energy (TKE), $k = \frac{3}{2}\overline{u_j' u_j'}$, characterizes the mean turbulence levels in the wall normal direction. The budget are the terms that determine the transport of TKE as given by the RANS equation for TKE transport. The terms are given by:

1. Production: $-\overline{u_i' u_j'} \frac{\partial \overline{u_i}}{\partial x_j}$
2. Viscous Dissipation: $\nu \overline{\frac{\partial u_i'}{\partial x_j} \frac{\partial u_i'}{\partial x_j}}$
3. Pressure Diffusion: $\frac{1}{\rho_0} \frac{\partial \overline{u_i' p'}}{\partial x_i}$

4. Viscous Diffusion: $\nu\frac{\partial^2 k}{\partial x_i^2}$

5. Turbulent Transport: $\frac{1}{2}\frac{\partial\overline{u_j' u_j' u_i'}}{\partial x_i}$

It is necessary here to point out that again, the notation follows that which is described in the beginning of this chapter. The turbulent budget, in the oscillated case, is calculated using the flucuations given by phase averaging. However, standard Reynolds Decomposition applies to the standard pipe.

Figures 3.6 and 3.7 illustrated the validation of gradients in the simulation by comparing the budget to literature. Taking note of the production term, if one considers a simple channel flow, the turbulence production can be seen to be generated from $\overline{u_1' u_2'}\frac{\partial\overline{U}_1}{\partial x_2}$, where subscript 1 is the streamwise direction and 2 is the wall normal direction. In the standard pipe, all other terms in production average to zero. However, the same cannot be said for an oscillated wall case due to the unsteady nature of the flow. In particular, the production term can be seen to be modulated by the azimuthal and radial fluctuations as the radial gradient of the azimuthal mean velocity is non-zero along with the azimuthal-radial covariance (figures B.1 and B.2).

Furthermore, it can be argued that due to the temporally varying mean azimuthal velocity, so too will the fluctuations in the azimuthal direction increase, particularly at points of maximum mean azimuthal acceleration. This increase in fluctuation magnitude will have an effect on increasing the overall turbulent kinetic energy in the region where the Stokes layers sees a maximum slope (most drastic change in azimuthal velocity) and thus increase the gradients in turbulent kinetic energy, enhancing diffusion of overall turbulent kinetic energy.

Figure 5.7 and 5.8 clearly show that effects on turbulent budget are similar between the two reynolds number when normalized properly. The normalization factor is as in validation $f = \frac{u_\tau^4}{\nu}$ production being reduced in the near wall region indicating that the

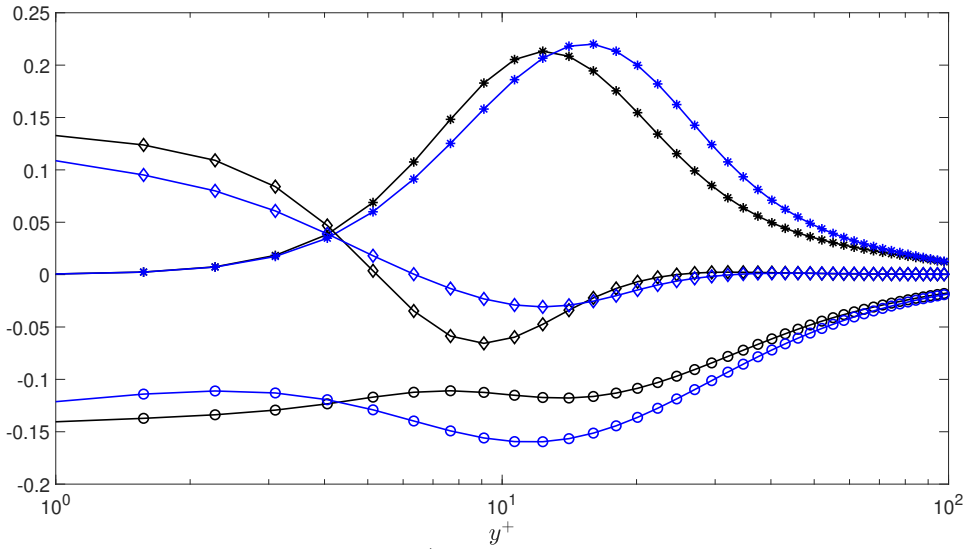

Figure 5.7: $Re_\tau = 170$ normalized by $\frac{u_\tau^4}{\nu}$; Standard Pipe ——; Oscillated Pipe ——
$\star$: Production, $\circ$: Viscous Dissipation, $\diamond$: Viscous Diffusion. The average behavior is to push the production further from the wall, increase dissipation and reduce diffusion. The decrease in diffusion is likely due to the overall reduction in turbulent fluctuations as shown by figures 5.1 and 5.2. The production peak is roughly the same but shifted out by the wall oscillations and balanced more aggressively by the dissipation of TKE

contribution of radial-azimuthal fluctations act to impede the production of turbulence. In the regions of maximum production dissipation is enhanced so in spite of the slightly higher peak production, the enhanced dissipation acts to diminish the overall TKE productions

Figure 5.9a and 5.9b show the average effects of turbulent transport, which moves turbulent fluctuations away from the wall and into the bulk flow. Clearly in the region below $y^+ = 10$ turbulent transport is enhanced and then is decreased everywhere beyond.

Figure 5.10 shows the modulation of the turbulent transport term as a function of wall phase. Clearly, between the region most affected ($0 < y^+ < 40$) the modulation must be coming from the average azimuthal and radial fluctuations. If one considers the transport in the radial gradient direction of azimuthal turbulent kinetic energy then it can be seen that transport as a production sink in the regions where production is maximized, that energy of radial and streamwise fluctations are likely being converted into azimuthal fluctuations

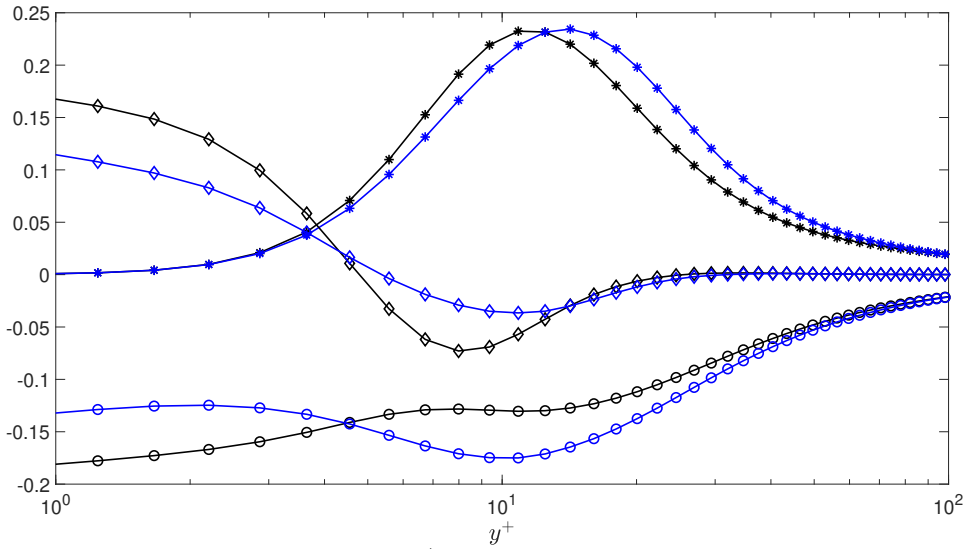

Figure 5.8: $Re_\tau = 360$ normalized by $\frac{u_\tau^4}{\nu}$; —: Standard Pipe; —: Oscillated Pipe $\star$: Production, $\circ$: Viscous Dissipation, $\diamond$: Viscous Diffusion. Behavior is identical to that described in figure 5.7

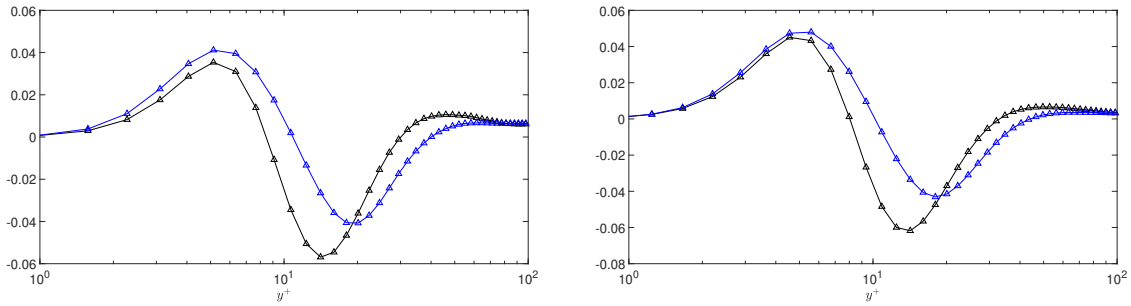

(a) Turbulent Transport term $Re_\tau = 170$ (b) Turbulent Transport term $Re_\tau = 360$

Figure 5.9: Turbulent transport term of TKE budget. —: Standard Pipe; —: Oscillated Pipe; In the region between $10 < y^+ < 20$ the transport of turbulent kinetic energy has been suppressed. Given the triple product of this term, it is difficult to tell what is causing the decrease in this region

that have no direct effect on sweep and ejections events. This is the beginning of the answer to why Q2 and Q4 events are suppressed, the TKE in the streamwise direction is acting as a sink to the production of more turbulence.

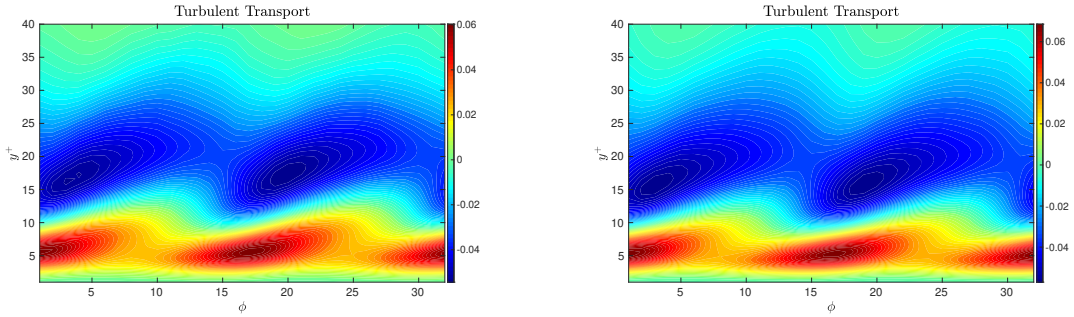

(a) Turbulent Transport term $Re_\tau = 170$ (b) Turbulent Transport term $Re_\tau = 360$

Figure 5.10: Turbulent transport term of TKE budget phase variation. It is evident that the modulation of the transport term is coming from the Azimuthal Velocity Fluctuations and azimuthal-radial fluctuations (figures B.1 and B.2 top and bottom right) as the behavior of this term is in roughly the radial gradient of those profiles

5.4 Velocity Distributions

This section presents joint probability density functions, the pre-multiplied joint PDFs and tabulated values of optimal disturbances. An optimal disturbance here is considered the to be the flucations event (u'_x, u'_r) associated with a maximum contribution to the Reynolds Stress and is given by

$$\left((u'_x, u'_r) \mid \max_{u'_x, u'_r} u'_s u'_r P(u'_x, u'_r) \right)$$

This has been shown to be associated with the near wall hairpins Moin *et al.* (1987) which pump low momentum fluid away from the wall and entrain high momentum fluid into the near wall region. It has already been shown in figures 5.5 and 5.6 that the Reynolds Stress in Quadrants 2 and 4 is diminished below $y^+ = 60$. It is expected that below this range either the angle of the optimal disturbance will decrease or the magnitude will decrease. Either effect will reduce the Reynolds Stress term and in the presence of wall oscillations ought to decrease the likelihood that an optimal disturbance will grow and produce turbulence from a perturbed turbulent mean velocity profile.

From the statistics provided it can be seen that the effects of wall oscillations is to vary the angle of the optimal sweep event away from the un-modified pipe. However, the

Case	$\sigma^+_{u_s}$	$\sigma^+_{u_r}$	$\frac{u_s}{\sigma_{u_s}}$	$\frac{u_r}{\sigma_{u_r}}$	θ	$\frac{u_s u_r}{\sigma_{u_s}\sigma_{u_r}}$
STD $Re_\tau = 170$	2.244	0.678	1.089	-0.92	-14.37	-1.006
	–	–	-1.945	1.416	167.60	-2.755
OSC $Re_\tau = 170$	2.197	0.630	1.195	-0.971	-13.12	-1.161
	–	–	-1.389	1.053	167.73	-1.463
STD $Re_\tau = 360$	2.111	0.693	1.157	-0.99	-15.70	-1.146
	–	–	-1.667	1.274	165.90	-2.124
OSC $Re_\tau = 360$	2.056	0.661	1.249	-1.090	-15.67	-1.361
	–	–	-1.364	1.142	164.95	-1.557

Table 5.1: Optimal Disturbances at $y^+ = 30$. Presented are the mean Optimal Disturbances in the pipe both with and without wall oscillations At this wall distance the mean phase disturbance is reduced for ejection events but not for sweeps. However, sweep disturbances are misaligned by 1.25 degrees indicating a deviation from the optimal due to wall oscillations

Case	$\sigma^+_{u_s}$	$\sigma^+_{u_r}$	$\frac{u_s}{\sigma_{u_s}}$	$\frac{u_r}{\sigma_{u_r}}$	θ	$\frac{u_s u_r}{\sigma_{u_s}\sigma_{u_r}}$
STD $Re_\tau = 170$	1.885	0.811	0.981	-0.97	-22.98	-0.948
	–	–	-1.688	1.405	160.29	-2.371
OSC $Re_\tau = 170$	1.910	0.767	1.144	-0.954	-18.51	-1.091
	–	–	-1.523	1.223	162.13	-1.862
STD $Re_\tau = 360$	1.832	0.826	1.066	-1.01	-23.06	-1.074
	–	–	-1.456	1.133	160.66	-1.649
OSC $Re_\tau = 360$	1.841	0.790	1.185	-1.058	-20.95	-1.254
	–	–	-1.378	1.145	160.37	-1.579

Table 5.2: Optimal Disturbances at $y^+ = 44$ It can be observed that for all phases the angle is reduced for sweep events and both angle and magnitude are reduced for ejection events. Notably the RMS of the radial fluctuations are decreased indicating that the overall transfer to and from the wall is being impeded

oscillations do not effect the magnitude of optimal sweep event Reynolds Stress despite a clear drop in the Quadrant Analysis shown in figures 5.5 and 5.6. The lowered angle indicates less momentum entrainment despite a similar Reynolds Stress producing event. Ejection events see little in event angle, if they do it is always decrease in angle, indicating less momentum transfer away from the wall from the maximum Reynolds Stress Producing event.

These changes are mostly imperceptible in the Probability Density functions however included in the appendix are the contour plots of the phase average joint PDFs along with the pre-multiplied PDFs.

Chapter 6

Conditional Eddies

In the previous chapter, optimal disturbances were presented as a function of y^+. Moin *et al.* (1987) tabulated the results from experimental data regarding the maximum Reynolds Stress producing event given a conditionally averaged field. Furthermore Zhou *et al.* (1999) showed a structure known as a turbulent hairpin was associated with such events. Using the method of Linear Stochastic Estimation outlined in Bonnet and Glauser (2012), it can be shown that a conditional average field can be approximated using a linear estimate constructed from the unconditionally averaged correlation function.

$$\hat{u}_i'(x') = L_{ij} u_j(x) \tag{6.1}$$

Here $\hat{u}_i'$ is the estimated fluctuating field at a location in the field, u_j is the conditional event at some location and L_ij is the linear stochastic estimator which can be constructed from the following correlation calculation

$$\langle u_j(x_i) u_k(x_i) \rangle_{x,\theta,t} L_{ij} = \langle u_i(x_i') u_k(x_i) \rangle_{x,\theta,t} \tag{6.2}$$

This is a tensor equation where x is the location of the prescribed event u_j' and x_i' is the

location of the velocity to be estimated. For estimating the fluctuating velocity field given a turbulent hairpin, the left hand side becomes the average correlation of fluctuating velocity at a given point x and the right hand side becomes the average two-point correlation tensor between the velocities.

Equation 6.3 gives the linear estimate of the total velocity at x'

$$\hat{u}_i = \overline{u}_i(x') + \hat{u}'_i(x') \tag{6.3}$$

Where $\hat{u}'_i$ is defined as in equation 6.1.

The estimators presented in this work were generated from the correlation functions in the standard pipe only, thus the definition of the fluctuating fields comes from the Reynolds Decomposition.

6.1 Influence of Wall Oscillation on Hairpin Growth and Auto-generation

Using the results presented in Table 5.2 velocity given Q2 event at $y^+ = 44$ was estimated for the non-oscillated pipe and it plus the mean turbulent velocity was used as an initial condition for the pipe flow. Figure 6.1 shows that the initial fields looks somewhat like a hairpin vortex and is allowed to grow and develop in a mean turbulent velocity profile over a period of $400t^+$ for both Reynolds numbers.

This means that a fluctuating event vector given by $\alpha\left(u'_r, u'_\theta, u'_x\right) = 3.0\left(u_{r,optimal}, 0, u_{x,optimal}\right)$ was chosen to define the conditional fluctuating field. Figure 6.1 shows a visualization of the initial conditions contoured on 10% of the maximum λ_{ci}. λ_{ci} is defined as the swirling strength criterion given by the complex part of the eigen values of the strain rate tensor for velocity Chakraborty *et al.* (2005).

6.1.1 Simulation of Conditional Field Growth

Figure 6.1 illustrates the initial conditions for the $Re_\tau = 170$ conditional eddy. Shown is a contour of λ_{ci} conditioned on 10% of the maximum in the domain. At $t = 0$ the wall velocity is zero and begins to move in the positive θ direction.

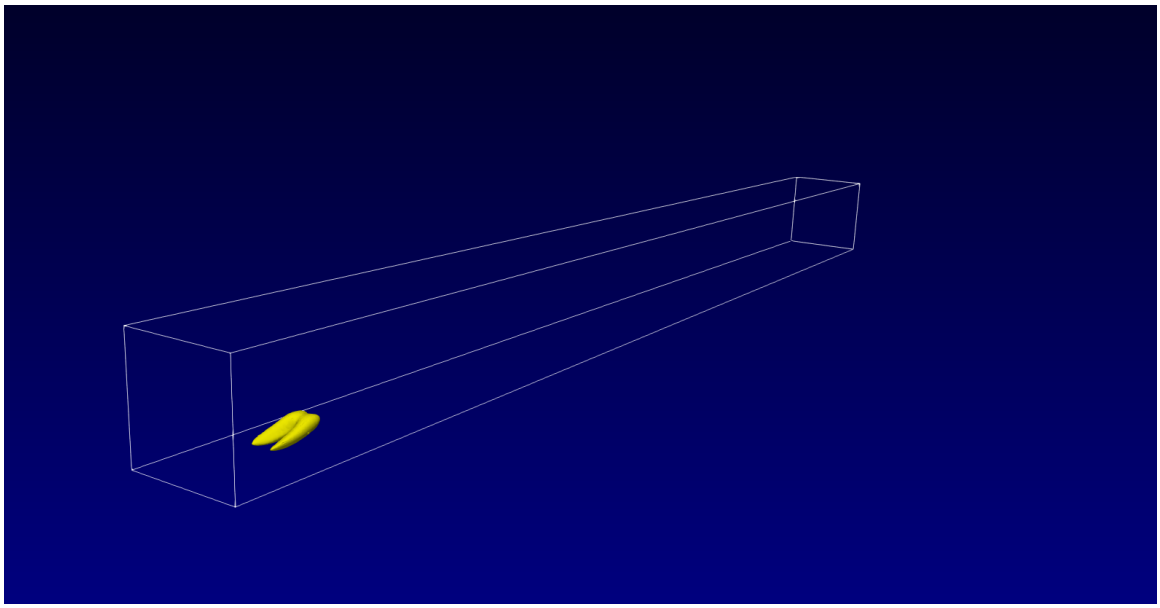

Figure 6.1: Hairpin Eddy visualized by λ_{ci} contours. Value is 10% of the maximum in the domain

This hairpin was allowed to grow for 4 oscillation periods or $400t^+$. Planar averages of Reynolds Stress were calculated to see the effects of wall oscillations on given a single hairpin. Figure 6.2 shows the development of average Reynolds stress as a function of time and wall location. Although the initial Reynolds stresses are identical, after $t^+ = 200$ the Reynolds stress in the oscillated pipe almost vanishes above $y^+ = 110$, and is reduced everywhere. Additionally, at $t^+ = 400$, the Reynolds Stress has been reduced all along the initial disturbance y^+ location, indicating that stress production is being reduced. Furthermore, above $y^+ = 110$ the Reynolds Stress almost vanishes. In the moderate Reynolds number case (figure 6.3), the fluctuations are merely suppressed by wall oscillations and do

not decay as rapidly in the wake. This is likely due to the initial disturbance starting far enough away from the stokes layer that only future hairpins are effected. Furthermore, it is also likely a Reynolds number effect that the overall turbulence decays from such a stable solution in the low Reynolds case

Figures 6.4 through 6.6 illustrate the development of when placed in an oscillating pipe versus a non-oscillating pipe. As time progresses the wall oscillation greatly distort the wake of the hairpin. Rather than generating directly behind the first hairpin the subsequents eddies "walk" up the wall of the pipe. Following hairpins will subsequently wrap further around the pipe. This helps to explain the observations made from figure 4.12. Over a long enough time period the eddies ought to walk back down the pipe.

Similar to the low Reynolds pipe, the moderate Reynolds number case exhibits similar properties. Figures 6.4 through 6.11 illustrate the similarity in behavior

It can be concluded here that the effects on the single hairpin is as follows:

1. The wall oscillations act to strength one hairpin leg and weaken the other (see figures 6.4 and 6.8)

2. As early times the wake of the hairpin is warped causing auto-generation to either a) be impeded or c) carry on at an angle oblique to the wake

3. As time progresses even further, auto-generation is very clearly suppressed at low Reynolds number (at least temporarily figure 6.6)

4. The wake of the hairpin is observed to, at least over $500t^+$ *walk* up the wall of the pipe despite the oscillations being sinusoidal

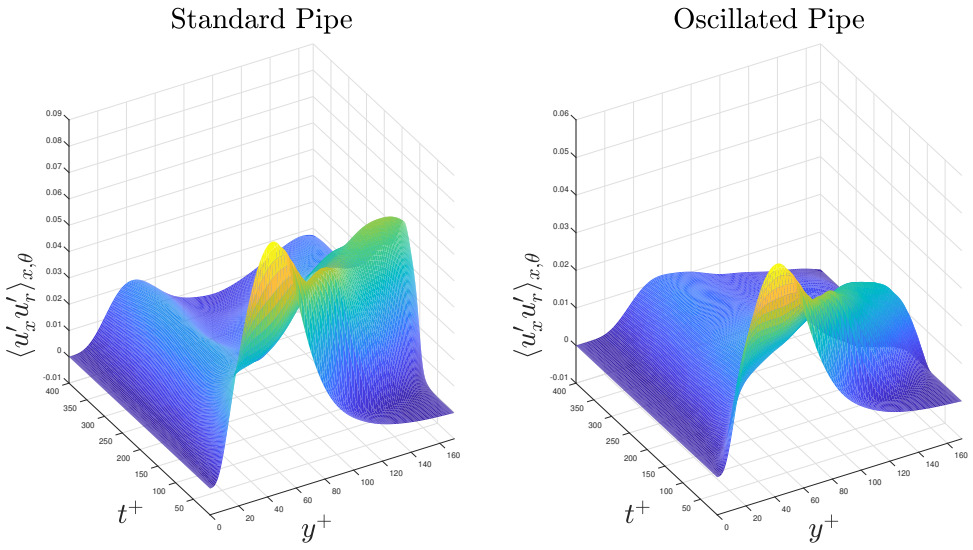

Figure 6.2: $Re_\tau = 170$ simulation; (left) No Oscillations (right) with oscillations. Reynolds Stress average over cyclindrical surfaces at $y^+ = R^+ - r^+ =$ constant. Clearly, at $t^+ = 400$ at the at location around $y^+ = 50$ of the given Q2 event well above the influence of the stokes layer the Reynolds Stress is diminished in the oscillated case. Additionally, after only $200t^+$ it can be observed that the head of the hairpin (which has lifted into the log layer is weakened as evidenced by the noticeable decrease in Reynolds Stress. The Reynolds Stress almost vanishes above $y^+ = 110$

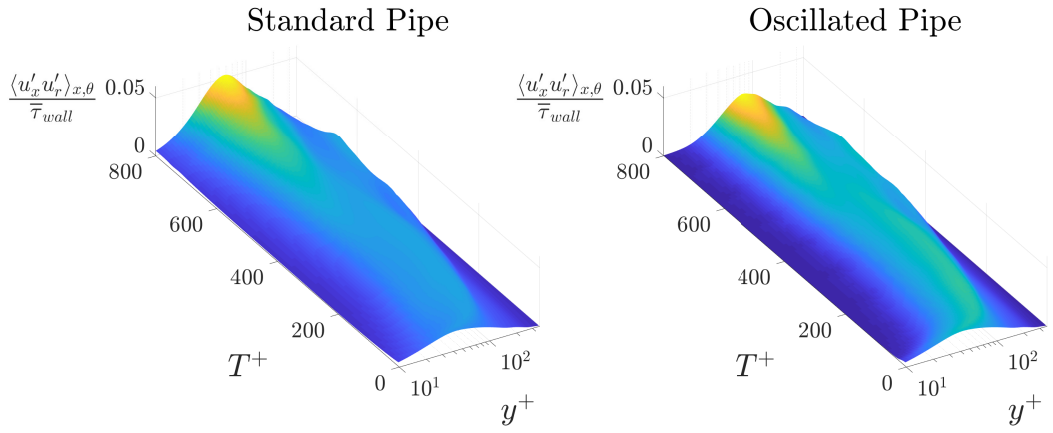

Figure 6.3: $Re_\tau = 360$ simulation; (left) No Oscillations (right) with oscillations. Reynolds Stress average over cyclindrical surfaces at $y^+ = R^+ - r^+ =$ constant. At this Reynolds number, the dynamics of the hairpin are markedly different. The main effects on the hairpin is to reduce the total streamwise-radial fluctuating quantity. This is most notable at $t^+ = 800$. However, through out the simulation Reynolds $\langle u_x' u_r' \rangle$ fluctations can be observed to be suppressed.

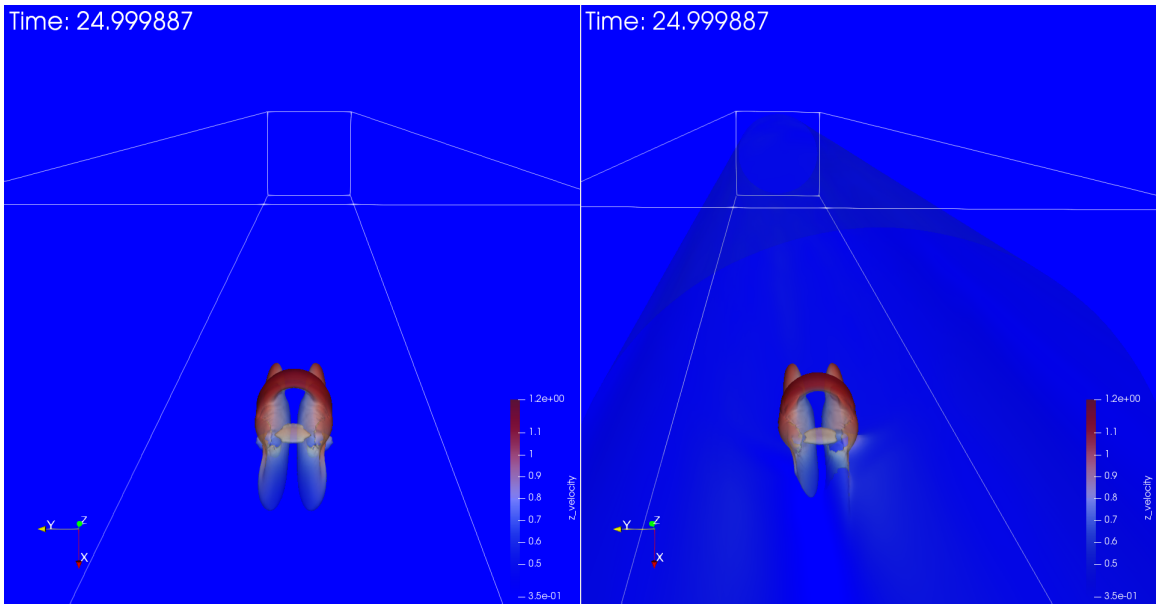

Figure 6.4: $Re_\tau = 170$ simulation; (Left) standard pipe; (Right) oscillated pipe. Comparison of the development at a quarter of an oscillation period at low Reynolds number $Re_\tau = 170$. Already the effects of wall oscillations can be observed to be effecting the right hairpin leg on the oscillated pipe

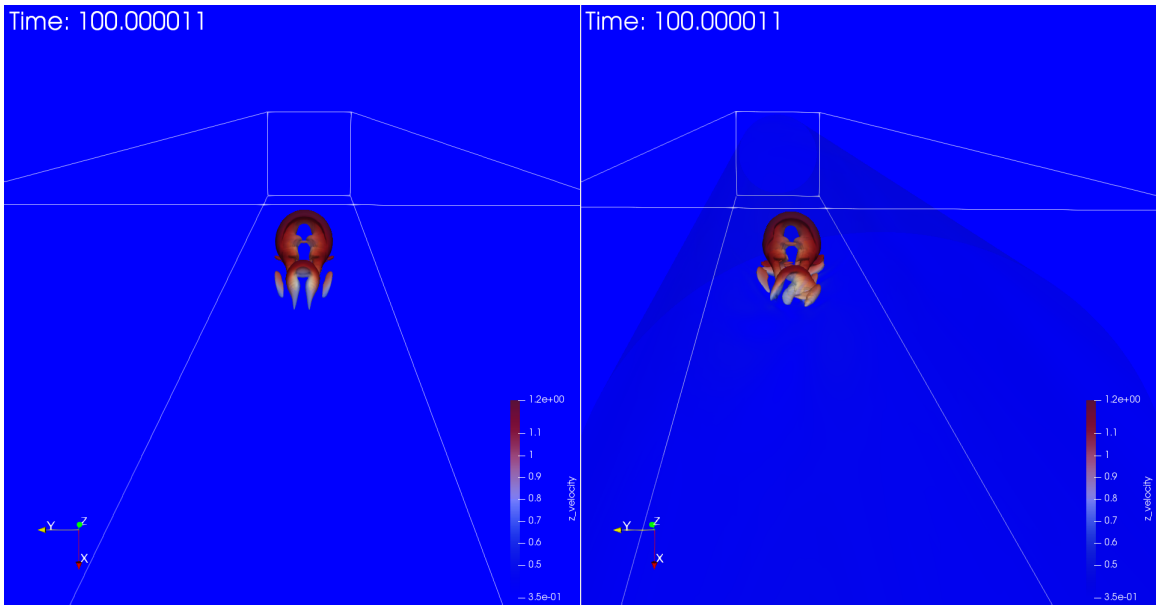

Figure 6.5: $Re_\tau = 170$ simulation; Comparison of the development after a full oscillation period at low Reynolds number $Re_\tau = 170$. Left: standard pipe; Right oscillated pipe. After $100t^+$ the wall oscillations can be observed to be distorting the generation of the eddy coming off the hairpin

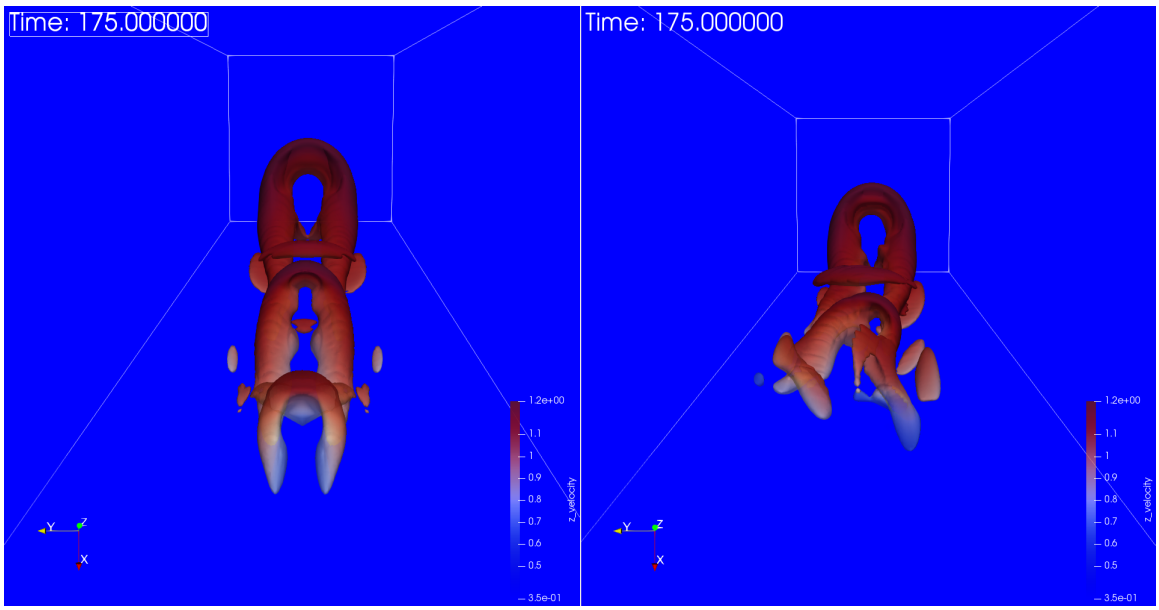

Figure 6.6: $Re_\tau = 170$ simulation; Comparison of the development after 1.75 oscillation period at low Reynolds number $Re_\tau = 170$. Left: standard pipe; Right oscillated pipe. At $150t^+$ the wall oscillations distort the secondary hairpin coming off the primary. The hairpin walkd up the wall and distorts the ejection of low momentum fluid. Furthermore, attenuation of generation of a third hairpin is also observed in the oscillated pipe.

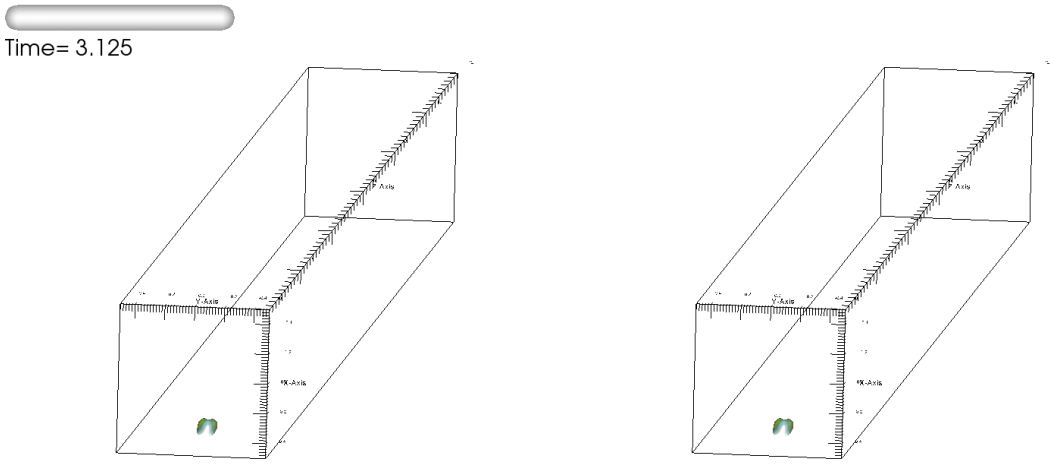

Figure 6.7: $Re_\tau = 360$ simulation; (left) Standard Pipe; (Right) Oscillated Pipe. Initial formation of the conditional eddy colored by streamwise velocity and contoured on swirling strength.

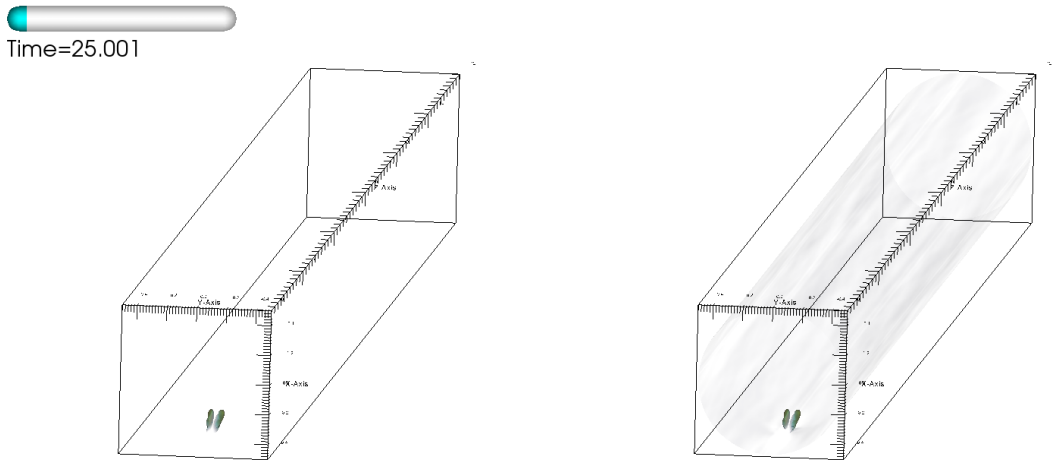

Figure 6.8: $Re_\tau = 360$ simulation; (left) Standard Pipe; (Right) Oscillated Pipe. Hairpin development after $25t^+$, already the legs are being skewed by the wall oscillations. The right leg is being strengthened while the left has disappeared

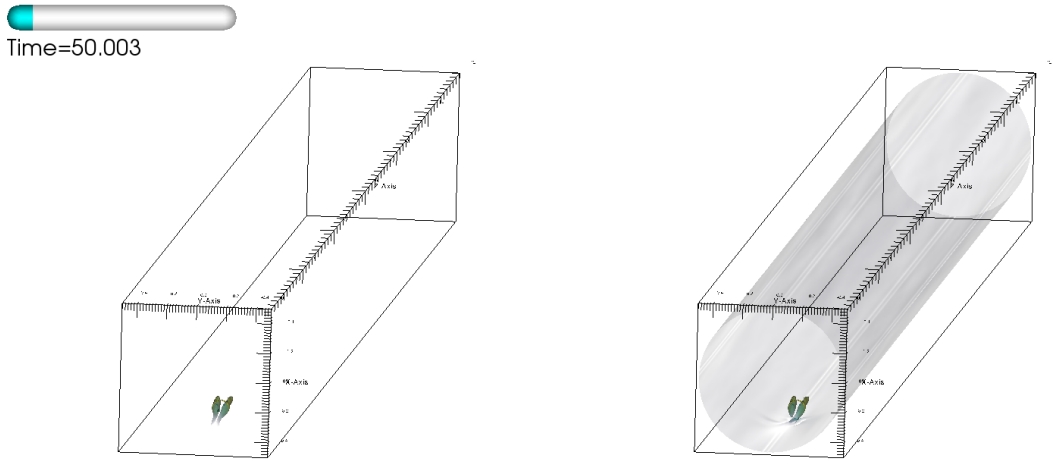

Figure 6.9: $Re_\tau = 360$ simulation; (left) Standard Pipe; (Right) Oscillated Pipe. Hairpin development after $50t^+$, The wake of the hairpin in the oscillated pipe can be observed to be skewed heavily by the pipe oscillations. However the head is remaining relatively unaffected

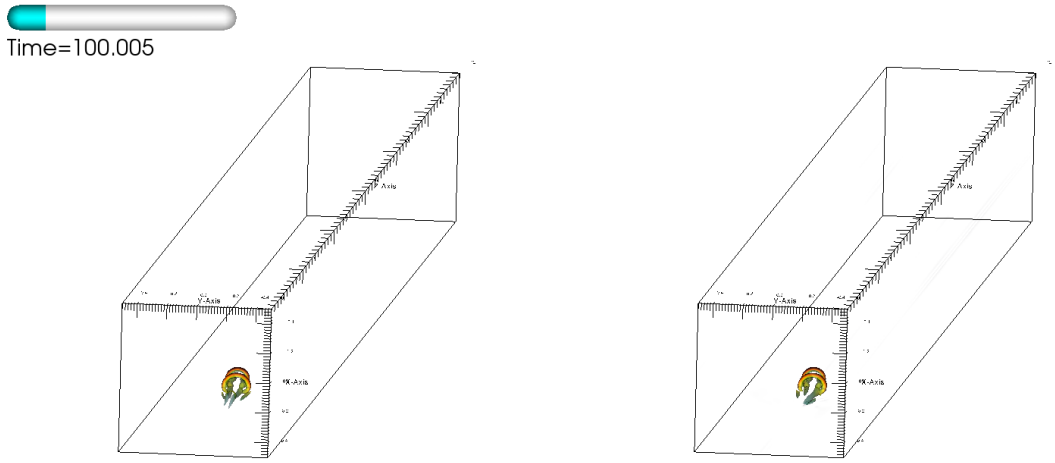

Figure 6.10: $Re_\tau = 360$ simulation; (left) Standard Pipe; (Right) Oscillated Pipe. Hairpin development after $100t^+$, clearly while the beginning of a secondary hairpin is can be seen just barely be seen in in the legs of the primary in the standard pipe, no such behavior is observable in the oscillated case instead, the left leg has been basically cut off

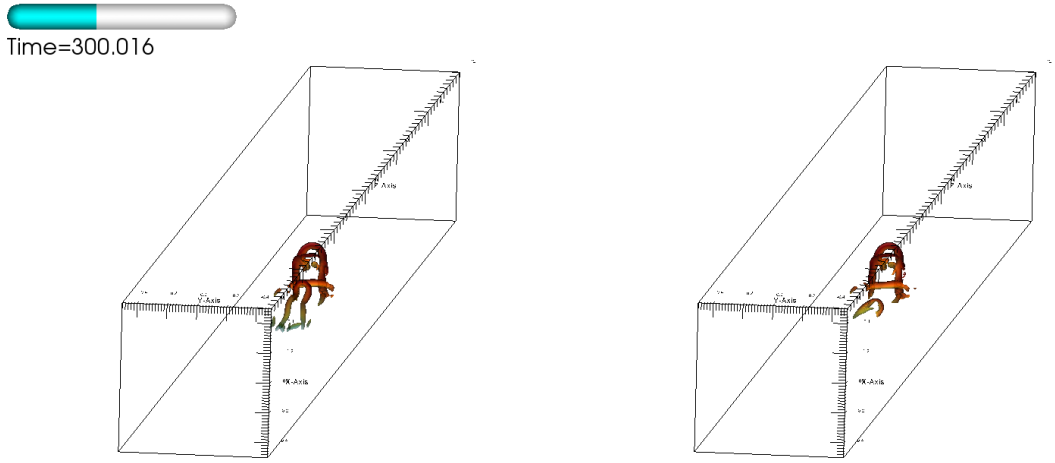

Figure 6.11: $Re_\tau = 360$ simulation; (left) Standard Pipe; (Right) Oscillated Pipe. Hairpin development after $300t^+$, The wake of the hairpin in the oscillated pipe is incoherent and the trailing eddies are completely detached and skewed off to one side. Meanwhile, a packet is beginning to form behind the hairpin in the standard pipe. A secondary hairpin is clearly visible in the standard pipes wake

Chapter 7

Conclusions

This research presents the results of two DNS Studies of drag reduced turbulent pipe flow with transverse wall oscillations. Comparisons of the turbulence were made to a standard pipe along with the collapse of the drag reduction effects when normalized with proper scaling.

Bulk parameters show that the mean quantities are exhibiting deterministic behavior near to the wall which necessitates implementing the phase averaged triple decomposition developed by Hussain and Reynolds (1970). Furthermore, it can be observed that there is no bias in the mean quantities of radial and azimuthal velocities in spite of initial transients.

Reynolds Stresses are much more telling of the changes in turbulence. Mean streamwise velocity is increased while the Reynolds stresses along with radial and streamwise fluctuations are reduced (figures 5.1 5.2). Phase to phase variation shows a fundamental change in the turbulence as observed by the periodic behavior of the stresses below the stokes layer (figures 5.3, B.1, 5.4, and 5.4). This indicates that the nature of the turbulence has changed to be, although statistically uncorrelated to the wall oscillations, linked with the wall oscillations. This makes sense when observing the turbulent budget 5.7. In particular the production is modulated by the non-zero azimuthal velocity gradient in the wall normal

direction. The change in turbulence all occurs to mainly suppress Q4 events (figures 5.5 and 5.6). Q2 events are suppressed somewhat as well but it is clear that most of the reduction in Reynolds Stress comes from the change in sweeps.

In order to fully understand the changes in the mechanisms a single disturbance was placed in the flow and allowed to grow. Figures 6.1 through 6.11 show this growth. Figure 6.2 shows that the Reynolds stress is being reduced, especially in the logarthimic region of the flow where it vanishes. This indicates that the mechanism of lifting of the head is being diminished as it is the azimuthal vorticity in the head that pumps fluid down towards the wall. Additionally in the region of the initial disturbance the Reynolds Stress is reduced indicating that the transport of fluctuations is reduced. The wake of the hairpin is heavily distorted and walks up the wall due to its relatively weaker vorticity. This reorients the sweep and ejection events which likely leads to sweeps colliding with ejections and cancelling out rather than just replacing the ejected fluid.

References

Adrian, R. J., "Hairpin vortex organization in wall turbulence", Physics of Fluids **19**, 4, 041301 (2007).

Baron, A. and M. Quadrio, "Turbulent drag reduction by spanwise wall oscillations", Applied Scientific Research **55**, 4, 311–326 (1995).

Bonnet, J.-P. and M. N. Glauser, *Eddy Structure Identification in Free Turbulent Shear Flows: Selected Papers from the IUTAM Symposium entitled:"Eddy Structures Identification in Free Turbulent Shear Flows" Poitiers, France, 12–14 October 1992*, vol. 21 (Springer Science & Business Media, 2012).

Brodkey, R. S., J. M. Wallace and H. Eckelmann, "Some properties of truncated turbulence signals in bounded shear flows", Journal of Fluid Mechanics **63**, 2, 209–224 (1974).

Chakraborty, P., S. Balachandar and R. J. Adrian, "On the relationships between local vortex identification schemes", Journal of fluid mechanics **535**, 189–214 (2005).

Choi, H., P. Moin and J. Kim, "Direct numerical simulation of turbulent flow over riblets", Journal of fluid mechanics **255**, 503–539 (1993).

Choi, H., P. Moin and J. Kim, "Active turbulence control for drag reduction in wall-bounded flows", Journal of Fluid Mechanics **262**, 75–110 (1994).

Choi, J.-I., C.-X. Xu and H. J. Sung, "Drag reduction by spanwise wall oscillation in wall-bounded turbulent flows", AIAA journal **40**, 5, 842–850 (2002).

Choi, K.-S., "European drag-reduction research—recent developments and current status", Fluid Dynamics Research **26**, 5, 325–335 (2000).

Choi, K.-S. and B. R. Clayton, "The mechanism of turbulent drag reduction with wall oscillation", International Journal of Heat and Fluid Flow **22**, 1, 1–9 (2001).

Company, A. P. S., "Transalaskan pipeline system — the facts", (2016).

Corino, E. R. and R. S. Brodkey, "A visual investigation of the wall region in turbulent flow", Journal of Fluid Mechanics **37**, 1, 1–30 (1969).

Den Toonder, J. and F. Nieuwstadt, "Reynolds number effects in a turbulent pipe flow for low to moderate re", Physics of Fluids **9**, 11, 3398–3409 (1997).

Deville, M. O., P. F. Fischer and E. H. Mund, *High-Order Methods for Incompressible Fluid FLow* (Cambridge University Press, 2002).

Eggels, J., F. Unger, M. Weiss, J. Westerweel, R. Adrian, R. Friedrich and F. Nieuwstadt, "Fully developed turbulent pipe flow: a comparison between direct numerical simulation and experiment", Journal of Fluid Mechanics **268**, 175–210 (1994).

El Khoury, G. K., P. Schlatter, A. Noorani, P. F. Fischer, G. Brethouwer and A. V. Johansson, "Direct numerical simulation of turbulent pipe flow at moderately high reynolds numbers", Flow, turbulence and combustion **91**, 3, 475–495 (2013).

Fischer, P., "An overlapping Schwarz method for spectral element solution of the incompressible Navier-Stokes equations", J. Comp. Phys. **133**, 84–101 (1997).

Fischer, P. and J. Mullen, "Filter-based stabilization of spectral element methods", Comptes Rendus de l'Académie des Sciences-Series I-Mathematics **332**, 3, 265–270 (2001).

Garcia-Mayoral, R. and J. Jimenez, "Drag reduction by riblets", Philosophical Transactions of the Royal Society of London A: Mathematical, Physical and Engineering Sciences **369**, 1940, 1412–1427 (2011a).

Garcia-Mayoral, R. and J. Jimenez, "Hydrodynamic stability and breakdown of the viscous regime over riblets", Journal of Fluid Mechanics **678**, 317–347 (2011b).

Goldshtik, M., V. Zametalin and V. Shtern, "Simplified theory of the near-wall turbulent layer of newtonian and drag-reducing fluids", Journal of Fluid Mechanics **119**, 423–441 (1982).

Goldstein, D. and T.-C. Tuan, "Secondary flow induced by riblets", Journal of Fluid Mechanics **363**, 115–151 (1998).

Hussain, A. K. M. F. and W. C. Reynolds, "The mechanics of an organized wave in turbulent shear flow", Journal of Fluid Mechanics **41**, 2, 241–258 (1970).

Kim, J., P. Moin and R. Moser, "Turbulence statistics in fully developed channel flow at low reynolds number", Journal of fluid mechanics **177**, 133–166 (1987).

Latorre, R. and V. V. Babenko, "Role of bubble injection technique drag reduction", in "Proceedings of the International Symposium on Seawater Drag Reduction", pp. 319–325 (1998).

Lumley, J. L., "Drag reduction by additives", Annual review of fluid mechanics **1**, 1, 367–384 (1969).

Madavan, N., S. Deutsch and C. Merkle, "Reduction of turbulent skin friction by microbubbles", The Physics of Fluids **27**, 2, 356–363 (1984).

Min, T., J. Y. Yoo, H. Choi and D. D. Joseph, "Drag reduction by polymer additives in a turbulent channel flow", Journal of Fluid Mechanics **486**, 213–238 (2003).

Moin, P., R. Adrian and J. Kim, "Stochastic estimation of organized structures in turbulent channel flow", in "6th Symposium on Turbulent Shear Flows", pp. 16–9 (1987).

Nakanishi, R., H. Mamori and K. Fukagata, "Relaminarization of turbulent channel flow using traveling wave-like wall deformation", International journal of heat and fluid flow **35**, 152–159 (2012).

Panton, R. L., *Incompressible flow* (Wiley Online Library, 1984).

Quadrio, M. and P. Ricco, "Critical assessment of turbulent drag reduction through spanwise wall oscillations", Journal of Fluid Mechanics **521**, 251–271 (2004).

Quadrio, M., P. Ricco and C. Viotti, "Streamwise-travelling waves of spanwise wall velocity for turbulent drag reduction", Journal of Fluid Mechanics **627**, 161–178 (2009).

Skote, M., "Comparison between spatial and temporal wall oscillations in turbulent boundary layer flows", Journal of Fluid Mechanics **730**, 273–294 (2013).

Sprague, M., M. Churchfield, A. Purkayastha, P. Moriarty and S. Lee, *Nek5000 Users Meeting* (National Renewable Energy Lab, 2010).

Tennekes, H., J. L. Lumley, J. Lumley *et al.*, *A first course in turbulence* (MIT press, 1972).

Tomiyama, N. and K. Fukagata, "Direct numerical simulation of drag reduction in a turbulent channel flow using spanwise traveling wave-like wall deformation", Physics of fluids **25**, 10, 105115 (2013).

Willmarth, W. and S. Lu, "Structure of the reynolds stress near the wall", Journal of Fluid Mechanics **55**, 1, 65–92 (1972).

Wu, X. and P. Moin, "A direct numerical simulation study on the mean velocity characteristics in turbulent pipe flow", Journal of Fluid Mechanics **608**, 81–112 (2008).

Yang, S.-Q., "Drag reduction in turbulent flow with polymer additives", Journal of Fluids Engineering **131**, 5, 051301 (2009).

Zhou, D. and K. S. Ball, "Turbulent drag reduction by spanwise wall oscillations", Internation Journal of Engineering **20**, 85–104 (2008).

Zhou, J., R. J. Adrian and S. Balachandar, "Autogeneration of near-wall vortical structures in channel flow", Physics of Fluids **8**, 1, 288–290 (1996).

Zhou, J., R. J. Adrian, S. Balachandar and T. Kendall, "Mechanisms for generating coherent packets of hairpin vortices in channel flow", Journal of fluid mechanics **387**, 353–396 (1999).

Appendix A

Raw Data

A.1 Optimal Disturbances for $Re_\tau = 170$

Case	$\sigma^+_{u_s}$	$\sigma^+_{u_r}$	$\frac{u_s}{\sigma_{u_s}}$	$\frac{u_r}{\sigma_{u_r}}$	θ	$\frac{u_s u_r}{\sigma_{u_s}\sigma_{u_r}}$
STD	0.343	0.007	1.465	-0.73	-0.56	-1.070
	–	–	-1.061	0.433	179.54	-0.459
OSC	0.266	0.009	0.727	-0.419	-1.14	-0.305
	–	–	-0.764	0.295	179.24	-0.226

Table A.1: Optimal Disturbances at $y^+ = 1$ over all Time

Case	$\sigma^+_{u_s}$	$\sigma^+_{u_r}$	$\frac{u_s}{\sigma_{u_s}}$	$\frac{u_r}{\sigma_{u_r}}$	θ	$\frac{u_s u_r}{\sigma_{u_s}\sigma_{u_r}}$
STD	0.979	0.045	1.580	-0.87	-1.45	-1.378
	–	–	-1.185	0.525	178.84	-0.622
OSC	0.680	0.059	0.648	-0.675	-5.15	-0.438
	–	–	-1.021	0.469	177.72	-0.479

Table A.2: Optimal Disturbances at $y^+ = 3$ over all Time

Case	$\sigma^+_{u_s}$	$\sigma^+_{u_r}$	$\frac{u_s}{\sigma_{u_s}}$	$\frac{u_r}{\sigma_{u_r}}$	θ	$\frac{u_s u_r}{\sigma_{u_s}\sigma_{u_r}}$
STD	1.234	0.068	1.577	-0.86	-1.72	-1.359
	–	–	-1.210	0.492	178.72	-0.596
OSC	0.840	0.095	0.700	-0.828	-7.64	-0.580
	–	–	-1.150	0.648	176.34	-0.744

Table A.3: Optimal Disturbances at $y^+ = 4$ over all Time

A.2 Optimal Disturbances for $Re_\tau = 360$

Case	$\sigma^+_{u_s}$	$\sigma^+_{u_r}$	$\frac{u_s}{\sigma_{u_s}}$	$\frac{u_r}{\sigma_{u_r}}$	θ	$\frac{u_s u_r}{\sigma_{u_s}\sigma_{u_r}}$
STD	1.460	0.091	1.629	-0.86	-1.89	-1.407
	–	–	-1.237	0.642	178.15	-0.794
OSC	0.985	0.137	0.730	-0.910	-9.82	-0.664
	–	–	-1.295	0.847	174.81	-1.097

Table A.4: Optimal Disturbances at $y^+ = 5$ over all Time

Case	$\sigma^+_{u_s}$	$\sigma^+_{u_r}$	$\frac{u_s}{\sigma_{u_s}}$	$\frac{u_r}{\sigma_{u_r}}$	θ	$\frac{u_s u_r}{\sigma_{u_s}\sigma_{u_r}}$
STD	1.880	0.145	1.581	-1.02	-2.84	-1.606
	–	–	-1.395	0.678	177.85	-0.946
OSC	1.291	0.203	0.843	-0.944	-10.01	-0.796
	–	–	-1.323	0.816	174.45	-1.080

Table A.5: Optimal Disturbances at $y^+ = 7$ over all Time

Case	$\sigma^+_{u_s}$	$\sigma^+_{u_r}$	$\frac{u_s}{\sigma_{u_s}}$	$\frac{u_r}{\sigma_{u_r}}$	θ	$\frac{u_s u_r}{\sigma_{u_s}\sigma_{u_r}}$
STD	2.269	0.235	1.538	-1.00	-3.85	-1.537
	–	–	-1.445	0.815	176.66	-1.178
OSC	1.684	0.276	1.136	-0.987	-8.09	-1.121
	–	–	-1.345	0.851	174.09	-1.145

Table A.6: Optimal Disturbances at $y^+ = 10$ over all Time

Case	$\sigma^+_{u_s}$	$\sigma^+_{u_r}$	$\frac{u_s}{\sigma_{u_s}}$	$\frac{u_r}{\sigma_{u_r}}$	θ	$\frac{u_s u_r}{\sigma_{u_s}\sigma_{u_r}}$
STD	2.560	0.372	1.347	-0.87	-5.35	-1.170
	–	–	-1.649	0.769	176.12	-1.268
OSC	2.168	0.346	1.631	-1.181	-6.59	-1.927
	–	–	-1.274	0.730	174.78	-0.931

Table A.7: Optimal Disturbances at $y^+ = 15$ over all Time

Case	$\sigma^+_{u_s}$	$\sigma^+_{u_r}$	$\frac{u_s}{\sigma_{u_s}}$	$\frac{u_r}{\sigma_{u_r}}$	θ	$\frac{u_s u_r}{\sigma_{u_s}\sigma_{u_r}}$
STD	2.532	0.461	1.251	-0.94	-7.81	-1.179
	–	–	-1.713	1.095	173.36	-1.876
OSC	2.317	0.418	1.444	-1.226	-8.71	-1.770
	–	–	-1.326	0.850	173.41	-1.127

Table A.8: Optimal Disturbances at $y^+ = 20$ over all Time

Case	$\sigma^+_{u_s}$	$\sigma^+_{u_r}$	$\frac{u_s}{\sigma_{u_s}}$	$\frac{u_r}{\sigma_{u_r}}$	θ	$\frac{u_s u_r}{\sigma_{u_s}\sigma_{u_r}}$
STD	2.248	0.678	1.087	-0.92	-14.37	-1.004
	–	–	-1.942	1.416	167.60	-2.750
OSC	2.197	0.630	1.190	-0.992	-13.45	-1.180
	–	–	-1.386	0.978	168.56	-1.355

Table A.9: Optimal Disturbances at $y^+ = 30$ over all Time

Case	$\sigma^+_{u_s}$	$\sigma^+_{u_r}$	$\frac{u_s}{\sigma_{u_s}}$	$\frac{u_r}{\sigma_{u_r}}$	θ	$\frac{u_s u_r}{\sigma_{u_s}\sigma_{u_r}}$
STD	1.887	0.811	0.980	-0.97	-22.98	-0.947
	–	–	-1.686	1.405	160.29	-2.368
OSC	1.910	0.767	1.145	-0.970	-18.80	-1.111
	–	–	-1.500	1.208	162.09	-1.812

Table A.10: Optimal Disturbances at $y^+ = 44$ over all Time

Case	$\sigma^+_{u_s}$	$\sigma^+_{u_r}$	$\frac{u_s}{\sigma_{u_s}}$	$\frac{u_r}{\sigma_{u_r}}$	θ	$\frac{u_s u_r}{\sigma_{u_s}\sigma_{u_r}}$
STD	1.750	0.844	1.025	-1.00	-25.28	-1.029
	–	–	-1.553	1.371	156.95	-2.130
OSC	1.790	0.807	1.110	-1.008	-22.25	-1.120
	–	–	-1.449	1.208	159.41	-1.751

Table A.11: Optimal Disturbances at $y^+ = 51$ over all Time

Case	$\sigma^+_{u_s}$	$\sigma^+_{u_r}$	$\frac{u_s}{\sigma_{u_s}}$	$\frac{u_r}{\sigma_{u_r}}$	θ	$\frac{u_s u_r}{\sigma_{u_s}\sigma_{u_r}}$
STD	1.556	0.843	1.081	-1.02	-27.07	-1.103
	–	–	-1.560	1.442	153.42	-2.248
OSC	1.617	0.810	1.135	-0.981	-23.41	-1.113
	–	–	-1.515	1.333	156.22	-2.019

Table A.12: Optimal Disturbances at $y^+ = 63$ over all Time

Case	$\sigma^+_{u_s}$	$\sigma^+_{u_r}$	$\frac{u_s}{\sigma_{u_s}}$	$\frac{u_r}{\sigma_{u_r}}$	θ	$\frac{u_s u_r}{\sigma_{u_s}\sigma_{u_r}}$
STD	1.432	0.824	1.115	-1.13	-30.27	-1.260
	–	–	-1.275	1.444	146.91	-1.841
OSC	1.494	0.795	1.134	-0.983	-24.76	-1.115
	–	–	-1.429	1.380	152.82	-1.972

Table A.13: Optimal Disturbances at $y^+ = 75$ over all Time

Case	$\sigma^+_{u_s}$	$\sigma^+_{u_r}$	$\frac{u_s}{\sigma_{u_s}}$	$\frac{u_r}{\sigma_{u_r}}$	θ	$\frac{u_s u_r}{\sigma_{u_s}\sigma_{u_r}}$
STD	1.313	0.791	1.224	-1.15	-29.51	-1.408
	–	–	-1.365	1.324	149.68	-1.807
OSC	1.371	0.765	1.100	-0.978	-26.39	-1.076
	–	–	-1.473	1.376	152.46	-2.028

Table A.14: Optimal Disturbances at $y^+ = 90$ over all Time

Case	$\sigma^+_{u_s}$	$\sigma^+_{u_r}$	$\frac{u_s}{\sigma_{u_s}}$	$\frac{u_r}{\sigma_{u_r}}$	θ	$\frac{u_s u_r}{\sigma_{u_s}\sigma_{u_r}}$
STD	1.243	0.767	1.139	-1.03	-29.25	-1.177
	–	–	-1.407	1.243	151.40	-1.748
OSC	1.297	0.745	1.072	-0.973	-27.52	-1.044
	–	–	-1.449	1.423	150.58	-2.063

Table A.15: Optimal Disturbances at $y^+ = 100$ over all Time

Case	$\sigma^+_{u_s}$	$\sigma^+_{u_r}$	$\frac{u_s}{\sigma_{u_s}}$	$\frac{u_r}{\sigma_{u_r}}$	θ	$\frac{u_s u_r}{\sigma_{u_s}\sigma_{u_r}}$
STD	1.093	0.722	1.094	-1.02	-31.50	-1.112
	–	–	-1.435	1.257	149.96	-1.805
OSC	1.165	0.708	1.012	-0.941	-29.49	-0.952
	–	–	-1.489	1.395	150.34	-2.078

Table A.16: Optimal Disturbances at $y^+ = 120$ over all Time

Case	$\sigma^+_{u_s}$	$\sigma^+_{u_r}$	$\frac{u_s}{\sigma_{u_s}}$	$\frac{u_r}{\sigma_{u_r}}$	θ	$\frac{u_s u_r}{\sigma_{u_s}\sigma_{u_r}}$
STD	1.013	0.695	0.971	-1.06	-36.84	-1.029
	–	–	-1.496	1.398	147.34	-2.093
OSC	1.101	0.686	1.024	-0.936	-29.67	-0.958
	–	–	-1.440	1.419	148.46	-2.044

Table A.17: Optimal Disturbances at $y^+ = 130$ over all Time

Case	$\sigma^+_{u_s}$	$\sigma^+_{u_r}$	$\frac{u_s}{\sigma_{u_s}}$	$\frac{u_r}{\sigma_{u_r}}$	θ	$\frac{u_s u_r}{\sigma_{u_s}\sigma_{u_r}}$
STD	0.871	0.598	0.996	-0.98	-34.03	-0.975
	–	–	-1.516	1.694	142.47	-2.568
OSC	0.974	0.598	1.101	-0.972	-28.46	-1.071
	–	–	-1.555	1.624	147.33	-2.526

Table A.18: Optimal Disturbances at $y^+ = 150$ over all Time

Case	$\sigma^+_{u_s}$	$\sigma^+_{u_r}$	$\frac{u_s}{\sigma_{u_s}}$	$\frac{u_r}{\sigma_{u_r}}$	θ	$\frac{u_s u_r}{\sigma_{u_s}\sigma_{u_r}}$
STD	0.845	0.594	0.993	-0.89	-32.16	-0.882
	–	–	-1.595	1.508	146.39	-2.405
OSC	0.936	0.595	1.099	-0.999	-30.02	-1.098
	–	–	-1.592	1.647	146.64	-2.622

Table A.19: Optimal Disturbances at $y^+ = 160$ over all Time

Case	$\sigma^+_{u_s}$	$\sigma^+_{u_r}$	$\frac{u_s}{\sigma_{u_s}}$	$\frac{u_r}{\sigma_{u_r}}$	θ	$\frac{u_s u_r}{\sigma_{u_s}\sigma_{u_r}}$
STD	0.341	0.008	1.252	-0.60	-0.65	-0.751
	–	–	-1.048	0.360	179.53	-0.377
OSC	0.273	0.010	0.837	-0.544	-1.35	-0.455
	–	–	-0.804	0.285	179.27	-0.229

Table A.20: Optimal Disturbances at $y^+ = 1$ over all Time

Case	$\sigma^+_{u_s}$	$\sigma^+_{u_r}$	$\frac{u_s}{\sigma_{u_s}}$	$\frac{u_r}{\sigma_{u_r}}$	θ	$\frac{u_s u_r}{\sigma_{u_s}\sigma_{u_r}}$
STD	0.962	0.053	1.571	-0.85	-1.70	-1.330
	–	–	-1.109	0.516	178.53	-0.572
OSC	0.713	0.063	0.813	-0.773	-4.79	-0.628
	–	–	-0.970	0.423	177.80	-0.410

Table A.21: Optimal Disturbances at $y^+ = 3$ over all Time

Case	$\sigma^+_{u_s}$	$\sigma^+_{u_r}$	$\frac{u_s}{\sigma_{u_s}}$	$\frac{u_r}{\sigma_{u_r}}$	θ	$\frac{u_s u_r}{\sigma_{u_s}\sigma_{u_r}}$
STD	1.205	0.079	1.461	-0.84	-2.15	-1.220
	–	–	-1.151	0.596	178.05	-0.686
OSC	0.882	0.099	0.937	-0.933	-6.40	-0.874
	–	–	-1.048	0.506	176.89	-0.530

Table A.22: Optimal Disturbances at $y^+ = 4$ over all Time

Case	$\sigma^+_{u_s}$	$\sigma^+_{u_r}$	$\frac{u_s}{\sigma_{u_s}}$	$\frac{u_r}{\sigma_{u_r}}$	θ	$\frac{u_s u_r}{\sigma_{u_s}\sigma_{u_r}}$
STD	1.416	0.104	1.627	-1.01	-2.61	-1.643
	–	–	-1.172	0.677	177.57	-0.794
OSC	1.033	0.140	0.975	-1.028	-8.11	-1.001
	–	–	-1.156	0.613	175.89	-0.709

Table A.23: Optimal Disturbances at $y^+ = 5$ over all Time

Case	$\sigma^+_{u_s}$	$\sigma^+_{u_r}$	$\frac{u_s}{\sigma_{u_s}}$	$\frac{u_r}{\sigma_{u_r}}$	θ	$\frac{u_s u_r}{\sigma_{u_s}\sigma_{u_r}}$
STD	1.805	0.165	1.636	-1.04	-3.31	-1.696
	–	–	-1.342	0.740	177.12	-0.993
OSC	1.344	0.203	1.144	-1.071	-8.06	-1.225
	–	–	-1.217	0.627	175.55	-0.763

Table A.24: Optimal Disturbances at $y^+ = 7$ over all Time

Case	$\sigma^+_{u_s}$	$\sigma^+_{u_r}$	$\frac{u_s}{\sigma_{u_s}}$	$\frac{u_r}{\sigma_{u_r}}$	θ	$\frac{u_s u_r}{\sigma_{u_s}\sigma_{u_r}}$
STD	2.166	0.260	1.540	-1.06	-4.73	-1.633
	–	–	-1.470	0.815	176.19	-1.198
OSC	1.718	0.277	1.391	-1.114	-7.35	-1.550
	–	–	-1.254	0.636	175.32	-0.798

Table A.25: Optimal Disturbances at $y^+ = 10$ over all Time

Case	$\sigma^+_{u_s}$	$\sigma^+_{u_r}$	$\frac{u_s}{\sigma_{u_s}}$	$\frac{u_r}{\sigma_{u_r}}$	θ	$\frac{u_s u_r}{\sigma_{u_s}\sigma_{u_r}}$
STD	2.404	0.399	1.273	-0.96	-7.15	-1.226
	–	–	-1.542	0.997	173.87	-1.537
OSC	2.108	0.376	1.479	-1.122	-7.71	-1.660
	–	–	-1.242	0.774	173.66	-0.961

Table A.26: Optimal Disturbances at $y^+ = 15$ over all Time

Case	$\sigma^+_{u_s}$	$\sigma^+_{u_r}$	$\frac{u_s}{\sigma_{u_s}}$	$\frac{u_r}{\sigma_{u_r}}$	θ	$\frac{u_s u_r}{\sigma_{u_s}\sigma_{u_r}}$
STD	2.359	0.481	1.127	-0.99	-10.14	-1.114
	–	–	-1.648	1.080	172.38	-1.779
OSC	2.184	0.453	1.376	-1.234	-10.54	-1.698
	–	–	-1.346	0.994	171.29	-1.339

Table A.27: Optimal Disturbances at $y^+ = 20$ over all Time

Case	$\sigma^+_{u_s}$	$\sigma^+_{u_r}$	$\frac{u_s}{\sigma_{u_s}}$	$\frac{u_r}{\sigma_{u_r}}$	θ	$\frac{u_s u_r}{\sigma_{u_s}\sigma_{u_r}}$
STD	2.111	0.693	1.157	-0.99	-15.70	-1.146
	–	–	-1.667	1.274	165.90	-2.124
OSC	2.056	0.661	1.213	-1.057	-15.65	-1.282
	–	–	-1.370	1.093	165.62	-1.497

Table A.28: Optimal Disturbances at $y^+ = 30$ over all Time

Case	$\sigma^+_{u_s}$	$\sigma^+_{u_r}$	$\frac{u_s}{\sigma_{u_s}}$	$\frac{u_r}{\sigma_{u_r}}$	θ	$\frac{u_s u_r}{\sigma_{u_s}\sigma_{u_r}}$
STD	1.832	0.826	1.066	-1.01	-23.06	-1.074
	–	–	-1.456	1.133	160.66	-1.649
OSC	1.841	0.790	1.156	-1.072	-21.68	-1.239
	–	–	-1.420	1.213	159.86	-1.722

Table A.29: Optimal Disturbances at $y^+ = 44$ over all Time

Case	$\sigma^+_{u_s}$	$\sigma^+_{u_r}$	$\frac{u_s}{\sigma_{u_s}}$	$\frac{u_r}{\sigma_{u_r}}$	θ	$\frac{u_s u_r}{\sigma_{u_s}\sigma_{u_r}}$
STD	1.739	0.868	1.151	-1.02	-23.81	-1.170
	–	–	-1.474	1.224	157.48	-1.804
OSC	1.761	0.831	1.146	-1.057	-23.53	-1.212
	–	–	-1.408	1.256	157.17	-1.768

Table A.30: Optimal Disturbances at $y^+ = 51$ over all Time

Case	$\sigma^+_{u_s}$	$\sigma^+_{u_r}$	$\frac{u_s}{\sigma_{u_s}}$	$\frac{u_r}{\sigma_{u_r}}$	θ	$\frac{u_s u_r}{\sigma_{u_s}\sigma_{u_r}}$
STD	1.614	0.886	1.213	-1.10	-26.50	-1.336
	–	–	-1.424	1.279	153.76	-1.821
OSC	1.649	0.849	1.191	-1.083	-25.08	-1.290
	–	–	-1.415	1.318	154.37	-1.865

Table A.31: Optimal Disturbances at $y^+ = 63$ over all Time

Case	$\sigma^+_{u_s}$	$\sigma^+_{u_r}$	$\frac{u_s}{\sigma_{u_s}}$	$\frac{u_r}{\sigma_{u_r}}$	θ	$\frac{u_s u_r}{\sigma_{u_s}\sigma_{u_r}}$
STD	1.533	0.888	1.185	-1.07	-27.66	-1.272
	–	–	-1.367	1.303	151.11	-1.781
OSC	1.575	0.852	1.160	-1.093	-27.02	-1.268
	–	–	-1.382	1.323	152.60	-1.829

Table A.32: Optimal Disturbances at $y^+ = 75$ over all Time

Case	$\sigma^+_{u_s}$	$\sigma^+_{u_r}$	$\frac{u_s}{\sigma_{u_s}}$	$\frac{u_r}{\sigma_{u_r}}$	θ	$\frac{u_s u_r}{\sigma_{u_s}\sigma_{u_r}}$
STD	1.455	0.880	1.218	-1.12	-29.15	-1.368
	–	–	-1.359	1.208	151.75	-1.642
OSC	1.501	0.847	1.220	-1.107	-27.13	-1.350
	–	–	-1.430	1.377	151.48	-1.969

Table A.33: Optimal Disturbances at $y^+ = 90$ over all Time

Case	$\sigma^+_{u_s}$	$\sigma^+_{u_r}$	$\frac{u_s}{\sigma_{u_s}}$	$\frac{u_r}{\sigma_{u_r}}$	θ	$\frac{u_s u_r}{\sigma_{u_s}\sigma_{u_r}}$
STD	1.413	0.871	1.188	-1.20	-31.95	-1.429
	–	–	-1.349	1.314	149.03	-1.773
OSC	1.459	0.841	1.257	-1.136	-27.51	-1.428
	–	–	-1.350	1.343	150.17	-1.814

Table A.34: Optimal Disturbances at $y^+ = 100$ over all Time

Case	$\sigma^+_{u_s}$	$\sigma^+_{u_r}$	$\frac{u_s}{\sigma_{u_s}}$	$\frac{u_r}{\sigma_{u_r}}$	θ	$\frac{u_s u_r}{\sigma_{u_s}\sigma_{u_r}}$
STD	1.342	0.848	1.200	-1.15	-31.25	-1.383
	–	–	-1.455	1.321	150.15	-1.922
OSC	1.387	0.823	1.229	-1.101	-28.00	-1.353
	–	–	-1.375	1.341	149.94	-1.843

Table A.35: Optimal Disturbances at $y^+ = 120$ over all Time

Case	$\sigma^+_{u_s}$	$\sigma^+_{u_r}$	$\frac{u_s}{\sigma_{u_s}}$	$\frac{u_r}{\sigma_{u_r}}$	θ	$\frac{u_s u_r}{\sigma_{u_s}\sigma_{u_r}}$
STD	1.305	0.821	1.175	-1.17	-32.17	-1.380
	–	–	-1.339	1.275	149.07	-1.707
OSC	1.348	0.800	1.235	-1.129	-28.49	-1.394
	–	–	-1.453	1.407	150.14	-2.044

Table A.36: Optimal Disturbances at $y^+ = 130$ over all Time

Case	$\sigma^+_{u_s}$	$\sigma^+_{u_r}$	$\frac{u_s}{\sigma_{u_s}}$	$\frac{u_r}{\sigma_{u_r}}$	θ	$\frac{u_s u_r}{\sigma_{u_s}\sigma_{u_r}}$
STD	1.208	0.678	1.260	-1.34	-30.89	-1.690
	–	–	-1.341	1.475	148.30	-1.978
OSC	1.251	0.668	1.250	-1.291	-28.88	-1.615
	–	–	-1.484	1.695	148.62	-2.516

Table A.37: Optimal Disturbances at $y^+ = 150$ over all Time

Case	$\sigma^+_{u_s}$	$\sigma^+_{u_r}$	$\frac{u_s}{\sigma_{u_s}}$	$\frac{u_r}{\sigma_{u_r}}$	θ	$\frac{u_s u_r}{\sigma_{u_s}\sigma_{u_r}}$
STD	1.179	0.672	1.133	-1.32	-33.58	-1.496
	–	–	-1.465	1.583	148.35	-2.319
OSC	1.224	0.662	1.252	-1.235	-28.06	-1.546
	–	–	-1.492	1.697	148.43	-2.531

Table A.38: Optimal Disturbances at $y^+ = 160$ over all Time

Appendix B

Figures

B.1 Stresses

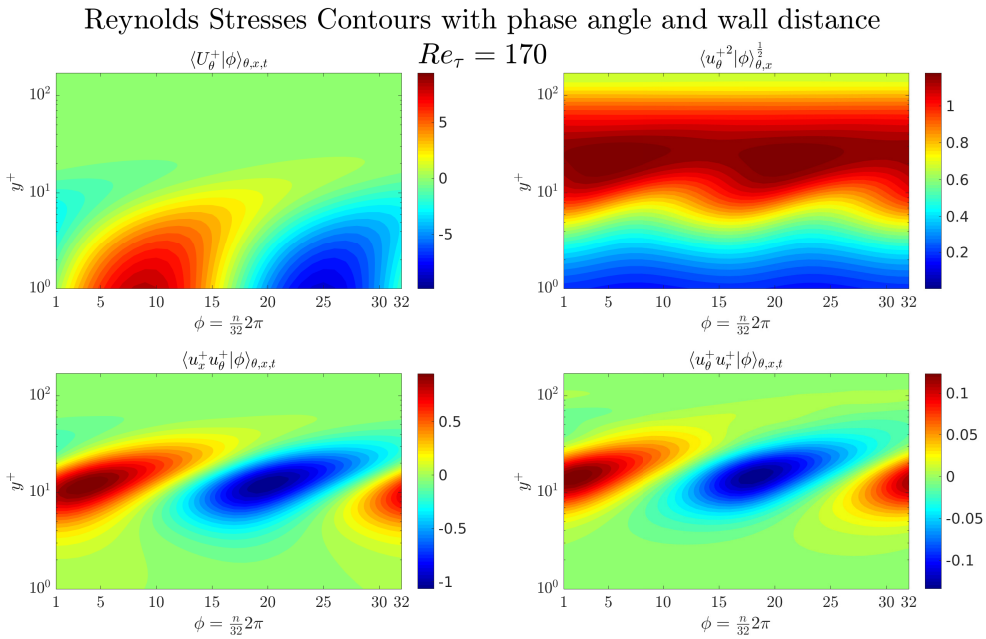

Figure B.1: Contours of the Reynolds stresses as a function of wall oscillation phase for $Re_\tau = 170$. Non-drag related statistics

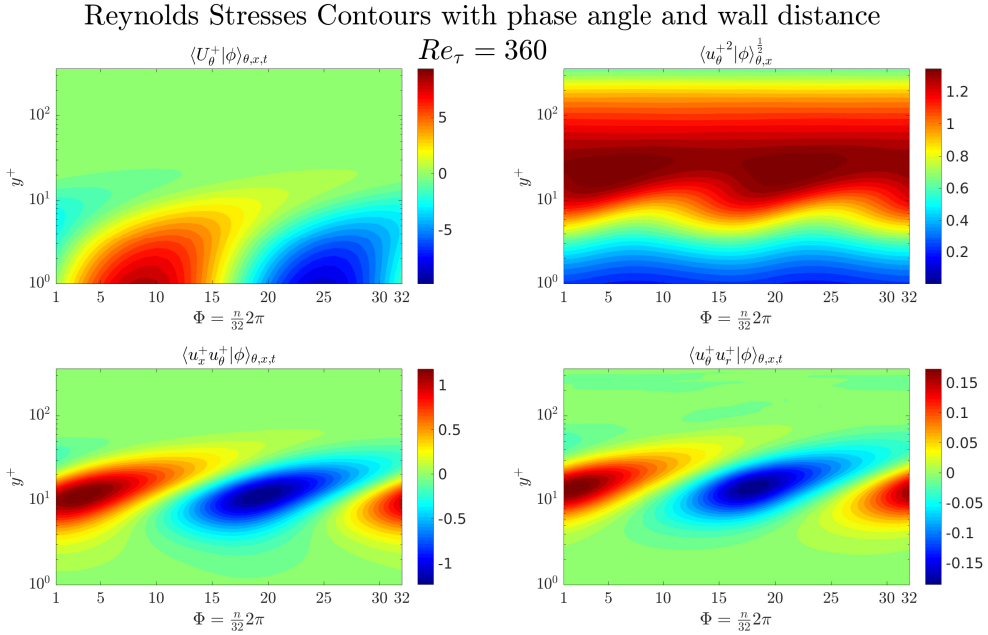

Figure B.2: Contours of the azimuthal components of Reynolds stresses as a function of wall phase for $Re_\tau = 360$. Non-drag related stresses

B.2 JOINT DISTRIBUTION OF STREAMWISE-RADIAL FLUCTUATIONS AT $RE_\tau = 170$

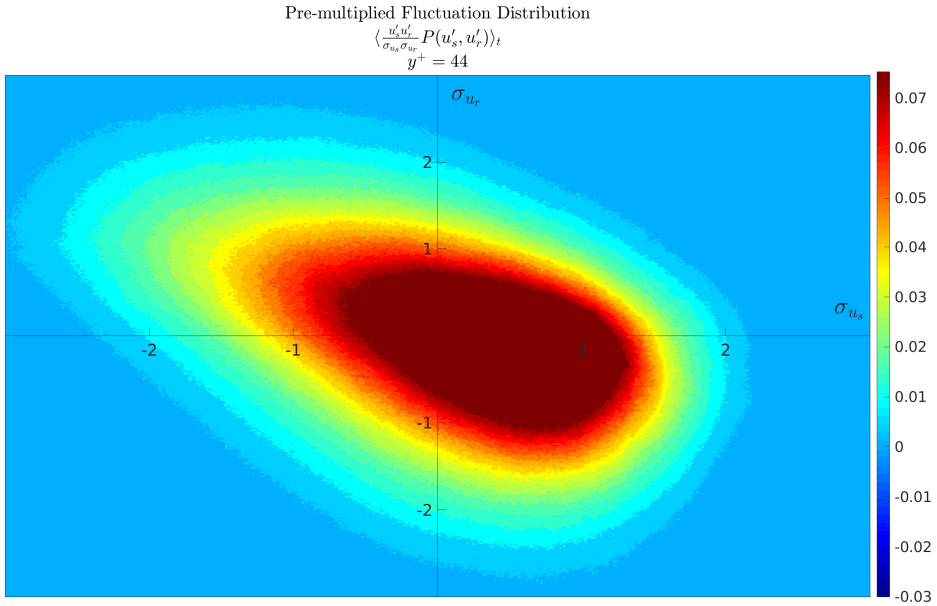

Figure B.3: Probability Distribution of the Streamwise and Azimuthal Fluctuations at $y^+ = 44$ for the standard pipe; $Re_\tau = 170$

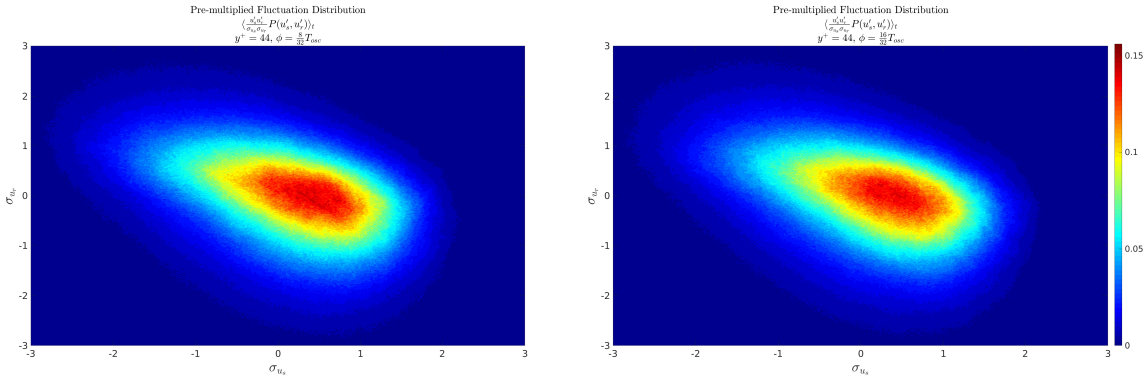

(a) Probability Distribution of the Streamwise and Azimuthal Fluctuations: $\phi = \frac{8}{32}\pi$

(b) Probability Distribution of the Streamwise and Azimuthal Fluctuations: $\phi = \frac{16}{32}\pi$

Figure B.4: Probability Density Function of (u'_x, u'_r) at $y^+ = 44$

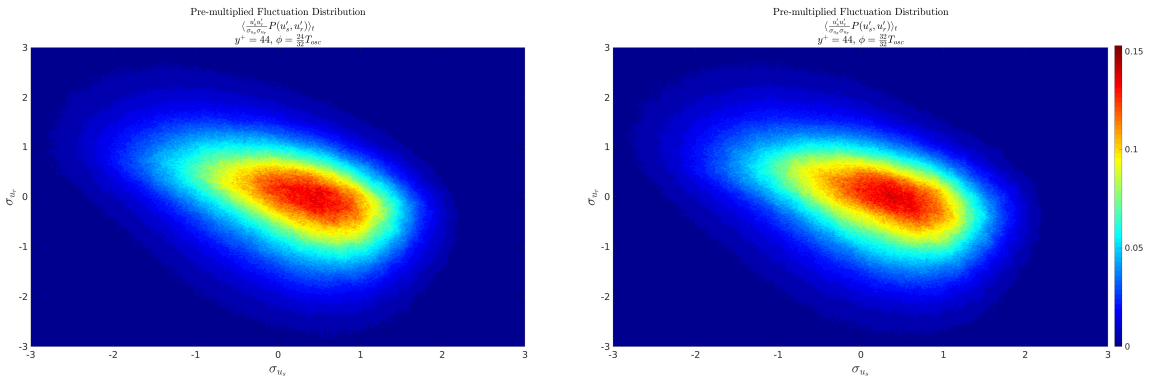

(a) Probability Distribution of the Streamwise and Azimuthal Fluctuations: $\phi = \frac{24}{32}\pi$

(b) Probability Distribution of the Streamwise and Azimuthal Fluctuations: $\phi = \frac{32}{32}\pi$

Figure B.5: Probability Density Function of (u'_x, u'_r) at $y^+ = 44$

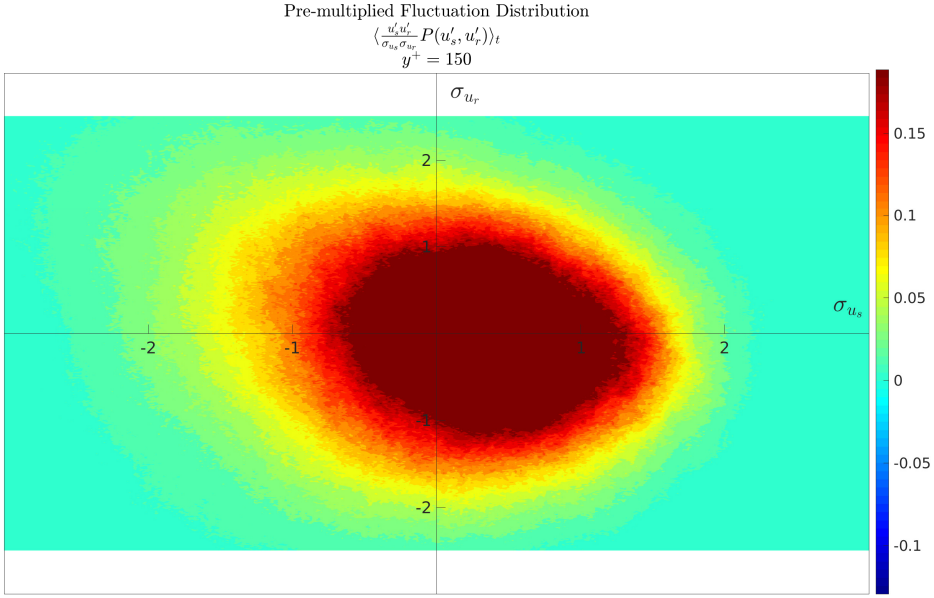

Figure B.6: Probability Distribution of the Streamwise and Azimuthal Fluctuations at $y^+ = 150$ for the standard pipe; $Re_\tau = 170$

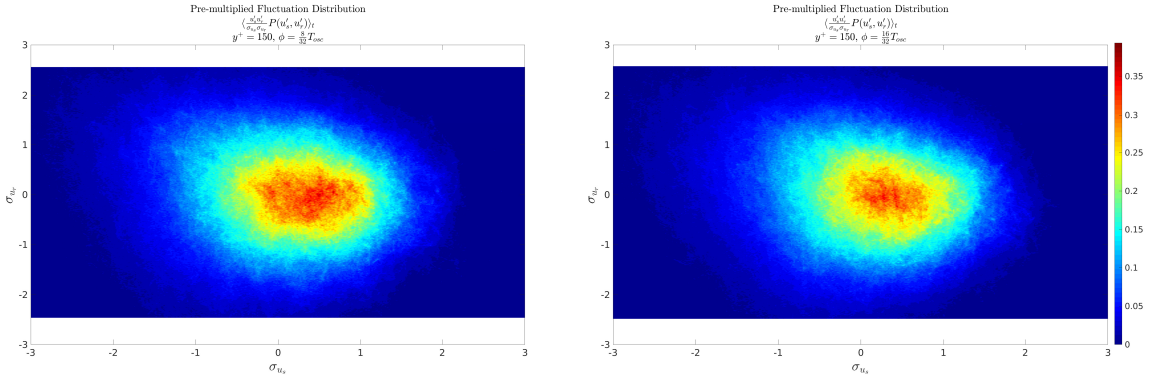

(a) Probability Distribution of the Streamwise and Azimuthal Fluctuations: $\phi = \frac{8}{32}\pi$

(b) Probability Distribution of the Streamwise and Azimuthal Fluctuations: $\phi = \frac{16}{32}\pi$

Figure B.7: Probability Density Function of (u'_x, u'_r) at $y^+ = 150$

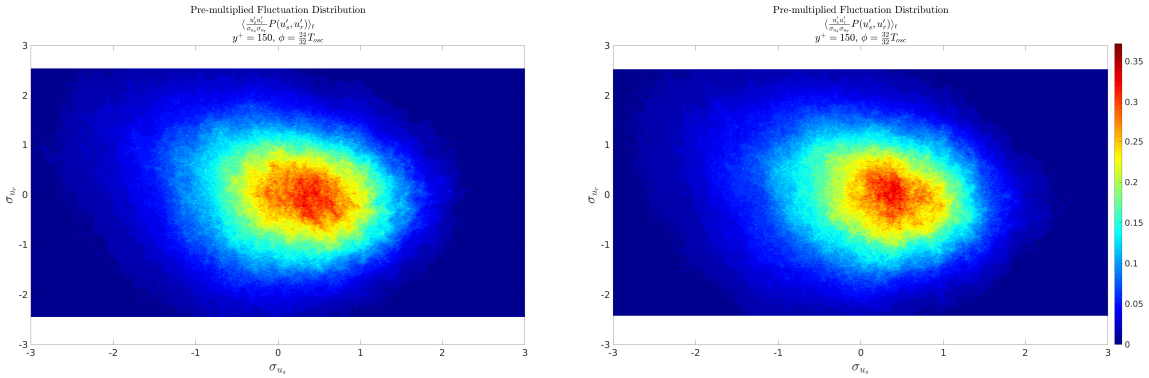

(a) Probability Distribution of the Streamwise and Azimuthal Fluctuations: $\phi = \frac{24}{32}\pi$

(b) Probability Distribution of the Streamwise and Azimuthal Fluctuations: $\phi = \frac{32}{32}\pi$

Figure B.8: Probability Density Function of (u'_x, u'_r) at $y^+ = 150$

B.3 DISTRIBUTION OF REYNOLDS STRESS $RE_\tau 170$

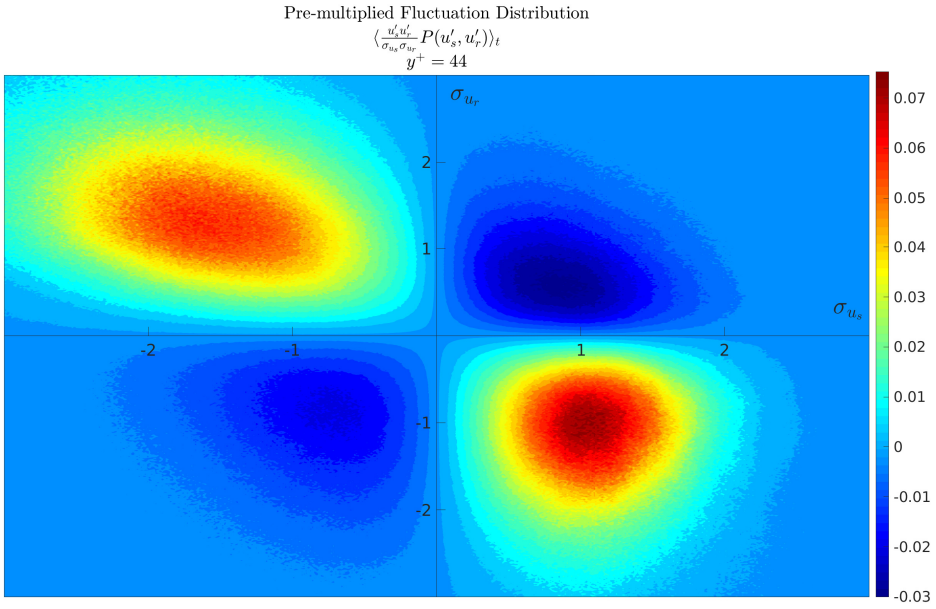

Figure B.9: Premultiplied Probability Distribution of the Streamwise and Azimuthal Fluctuations at $y^+ = 44$ for the standard pipe; $Re_\tau = 170$

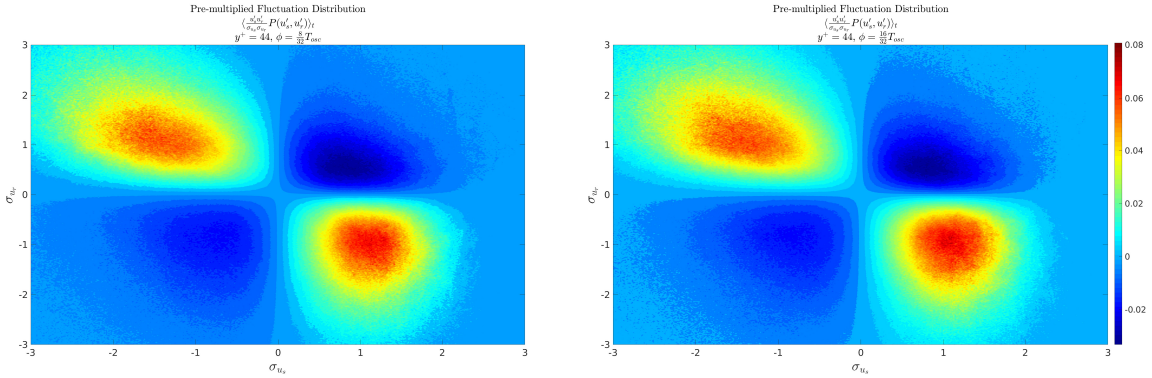

(a) Probability Distribution of the Streamwise and Azimuthal Fluctuations: $\phi = \frac{8}{32}\pi$

(b) Probability Distribution of the Streamwise and Azimuthal Fluctuations: $\phi = \frac{16}{32}\pi$

Figure B.10: Premultiplied Probability Density Function of (u'_x, u'_r) at $y^+ = 44$

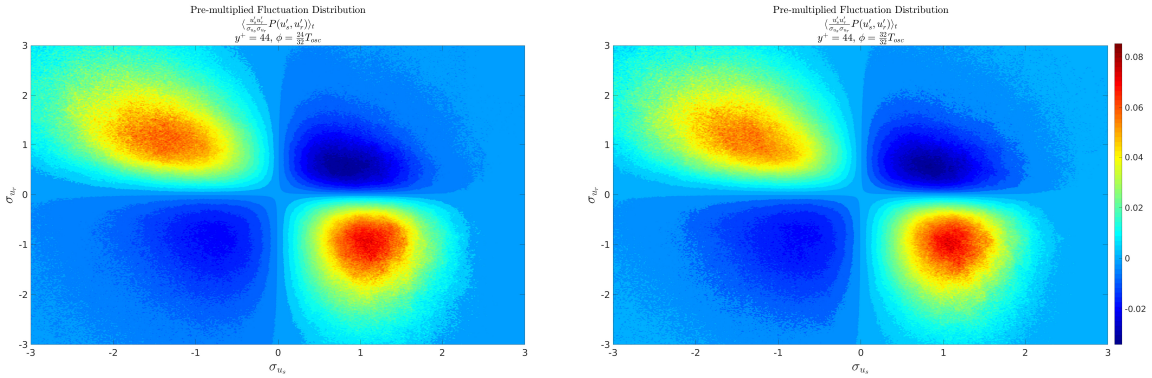

(a) Probability Distribution of the Streamwise and Azimuthal Fluctuations: $\phi = \frac{24}{32}\pi$

(b) Probability Distribution of the Streamwise and Azimuthal Fluctuations: $\phi = \frac{32}{32}\pi$

Figure B.11: Premultiplied Probability Density Function of (u'_x, u'_r) at $y^+ = 44$

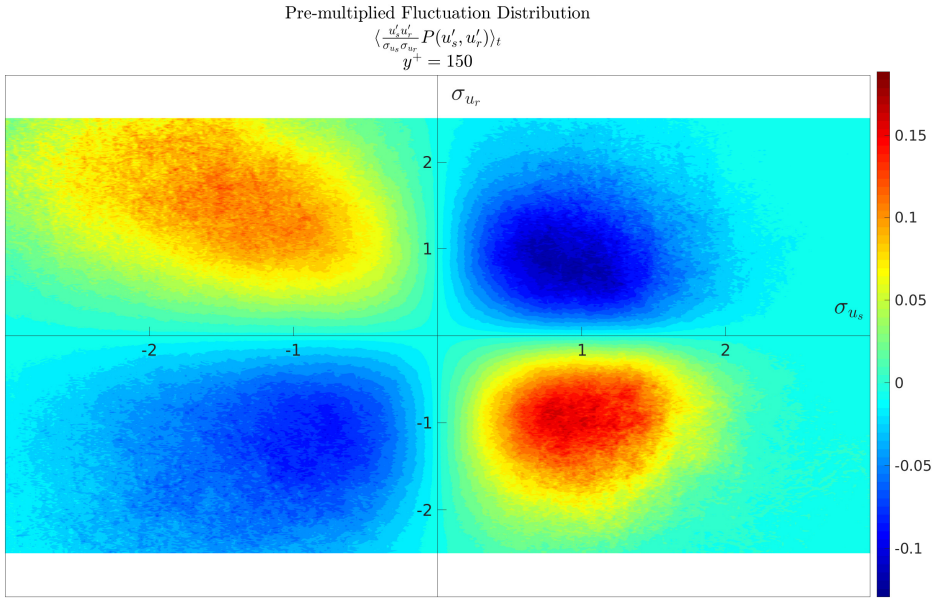

Figure B.12: Premultiplied Probability Distribution of the Streamwise and Azimuthal Fluctuations at $y^+ = 150$ for the standard pipe; $Re_\tau = 170$

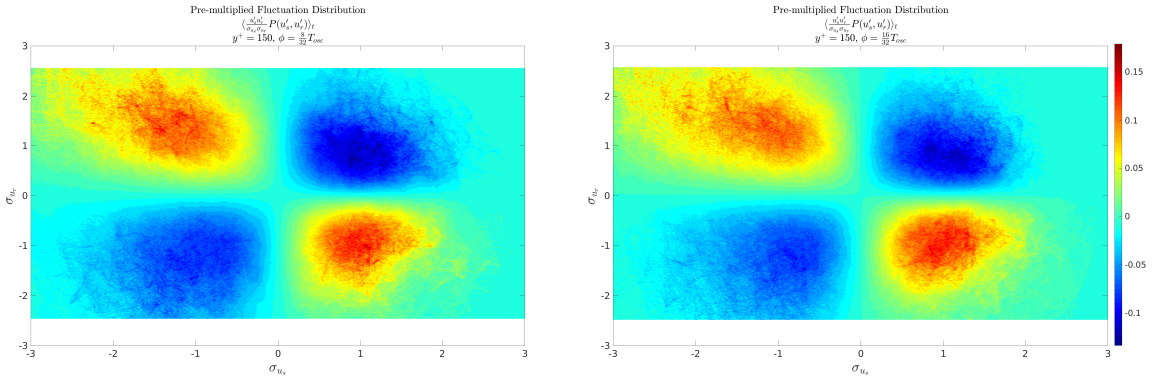

(a) Probability Distribution of the Streamwise and Azimuthal Fluctuations: $\phi = \frac{8}{32}\pi$

(b) Probability Distribution of the Streamwise and Azimuthal Fluctuations: $\phi = \frac{16}{32}\pi$

Figure B.13: Premultiplied Probability Density Function of (u'_x, u'_r) at $y^+ = 150$

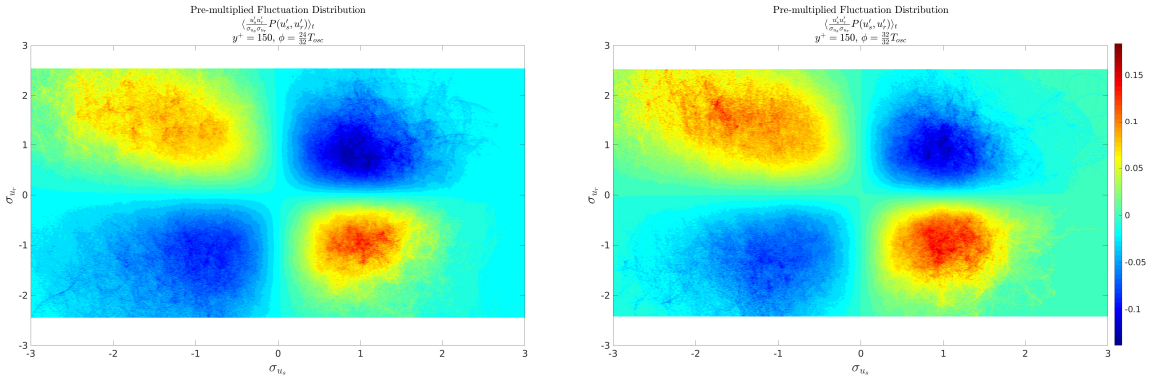

(a) Probability Distribution of the Streamwise and Azimuthal Fluctuations: $\phi = \frac{24}{32}\pi$

(b) Probability Distribution of the Streamwise and Azimuthal Fluctuations: $\phi = \frac{32}{32}\pi$

Figure B.14: Premultiplied Probability Density Function of (u'_x, u'_r) at $y^+ = 150$

B.4 JOINT DISTRIBUTION OF STREAMWISE-RADIAL FLUCTUATIONS AT $RE_\tau = 360$

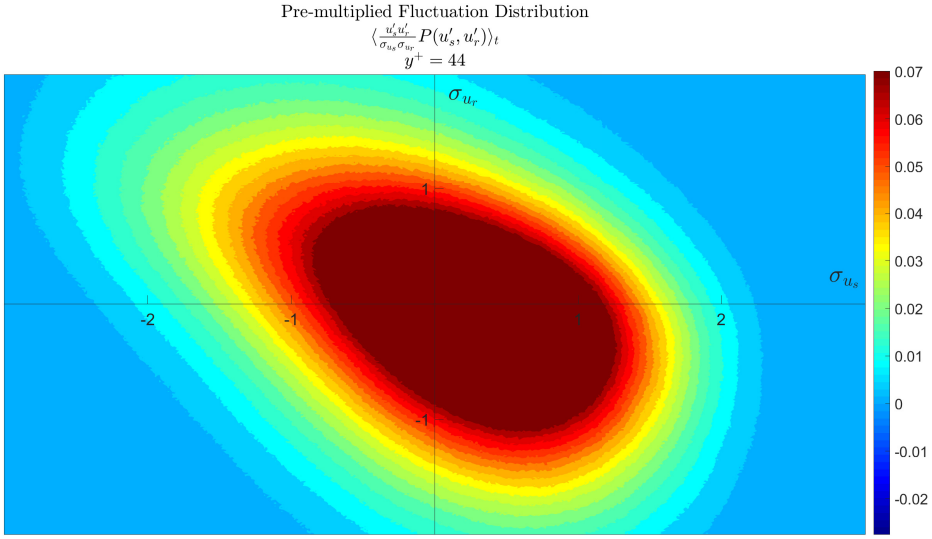

Figure B.15: Probability Distribution of the Streamwise and Azimuthal Fluctuations at $y^+ = 44$ for the standard pipe; $Re_\tau = 360$

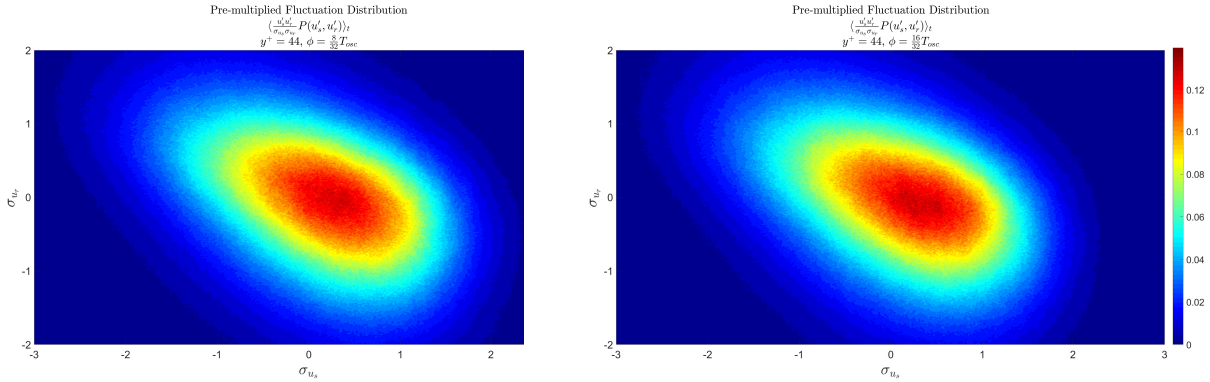

(a) Probability Distribution of the Streamwise and Azimuthal Fluctuations: $\phi = \frac{8}{32}\pi$

(b) Probability Distribution of the Streamwise and Azimuthal Fluctuations: $\phi = \frac{16}{32}\pi$

Figure B.16: Probability Density Function of (u'_x, u'_r) at $y^+ = 44$

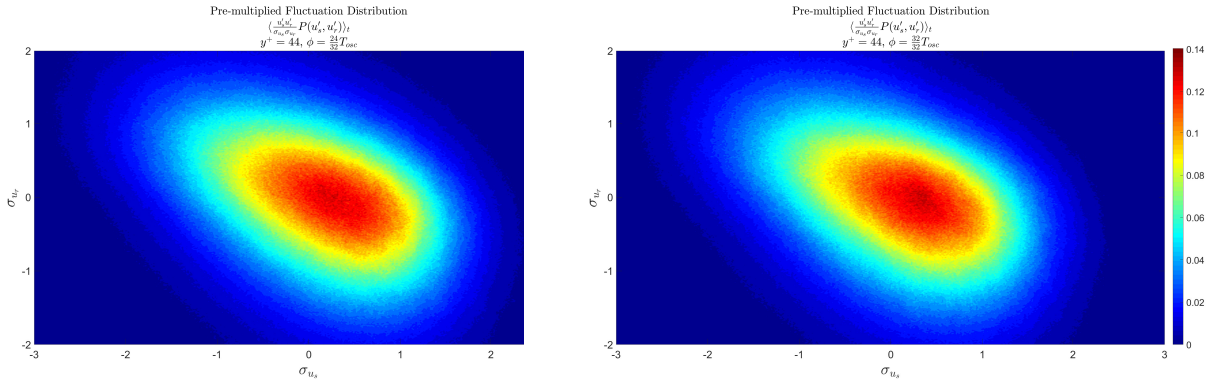

(a) Probability Distribution of the Streamwise and Azimuthal Fluctuations: $\phi = \frac{24}{32}\pi$

(b) Probability Distribution of the Streamwise and Azimuthal Fluctuations: $\phi = \frac{32}{32}\pi$

Figure B.17: Probability Density Function of (u'_x, u'_r) at $y^+ = 44$

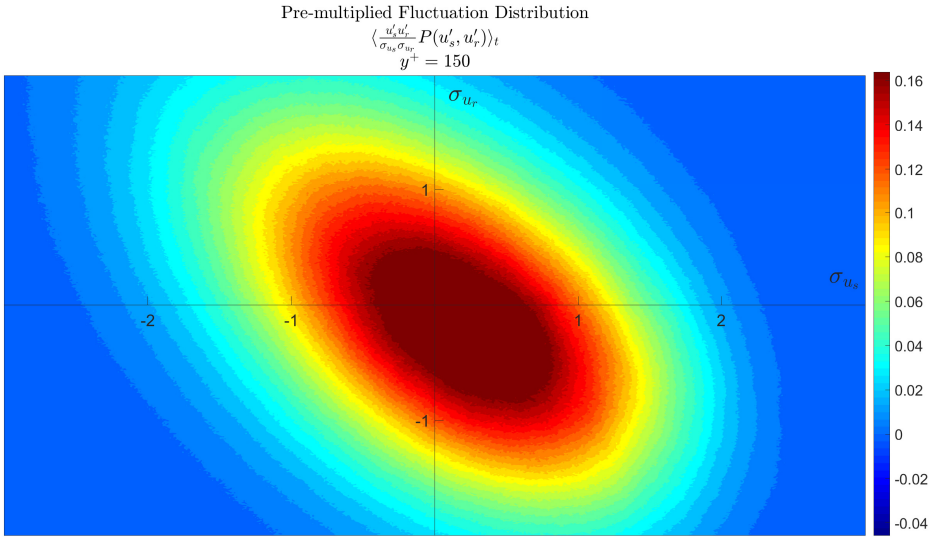

Figure B.18: Probability Distribution of the Streamwise and Azimuthal Fluctuations at $y^+ = 150$ for the standard pipe; $Re_\tau = 360$

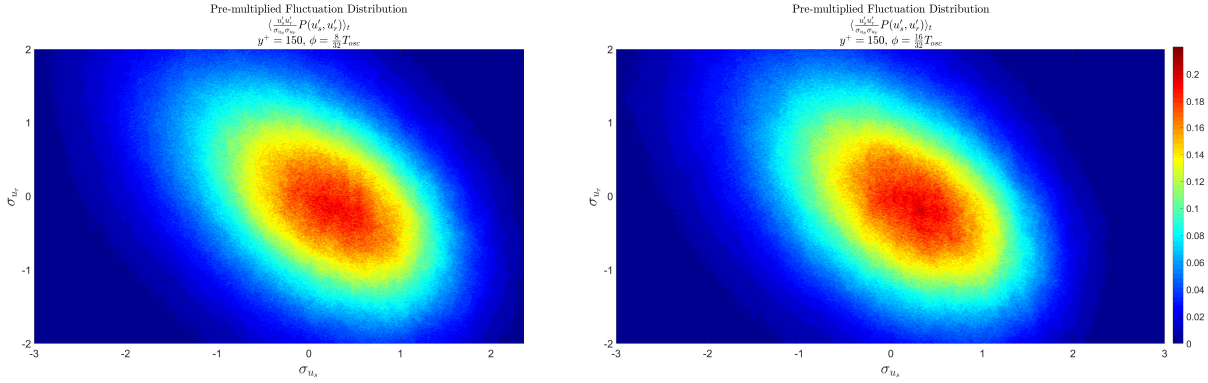

(a) Probability Distribution of the Streamwise and Azimuthal Fluctuations: $\phi = \frac{8}{32}\pi$

(b) Probability Distribution of the Streamwise and Azimuthal Fluctuations: $\phi = \frac{16}{32}\pi$

Figure B.19: Probability Density Function of (u'_x, u'_r) at $y^+ = 150$

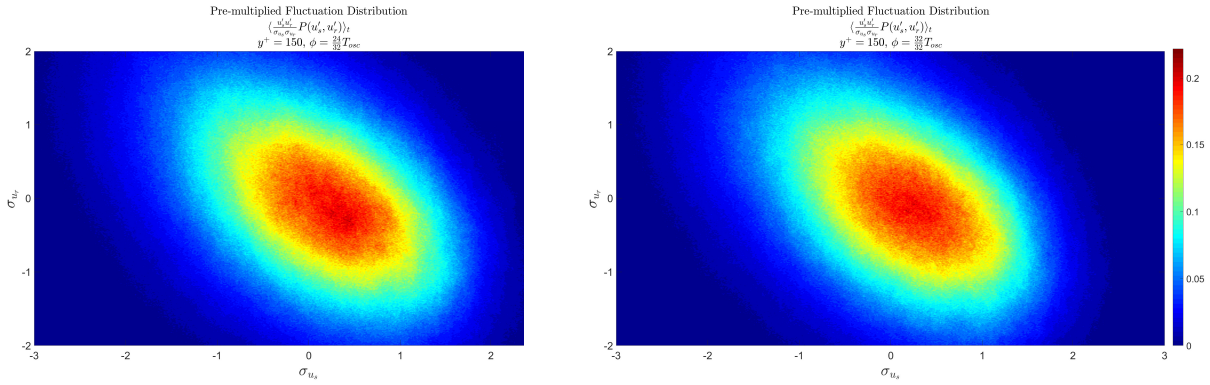

(a) Probability Distribution of the Streamwise and Azimuthal Fluctuations: $\phi = \frac{24}{32}\pi$

(b) Probability Distribution of the Streamwise and Azimuthal Fluctuations: $\phi = \frac{32}{32}\pi$

Figure B.20: Probability Density Function of (u'_x, u'_r) at $y^+ = 150$

B.5 DISTRIBUTION OF REYNOLDS STRESS $RE_\tau 360$

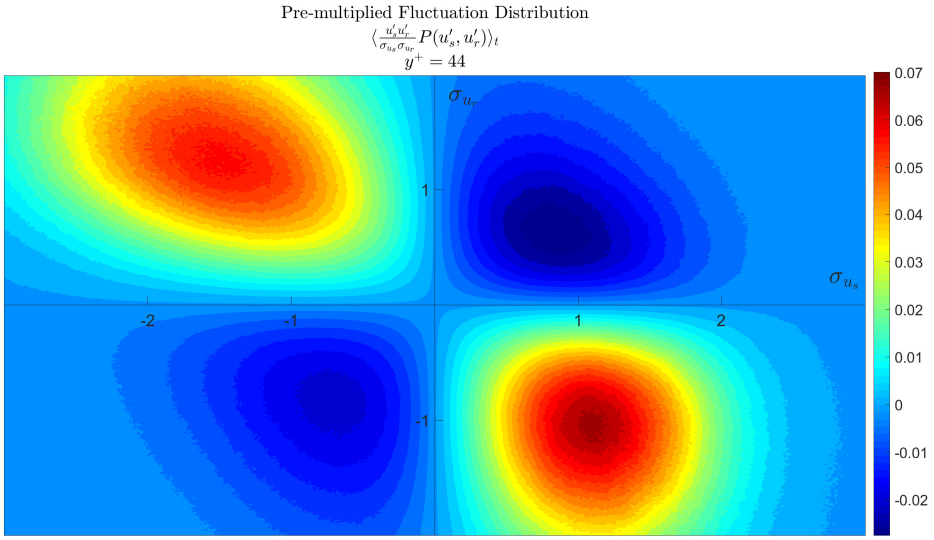

Figure B.21: Premultiplied Probability Distribution of the Streamwise and Azimuthal Fluctuations at $y^+ = 44$ for the standard pipe; $Re_\tau = 360$

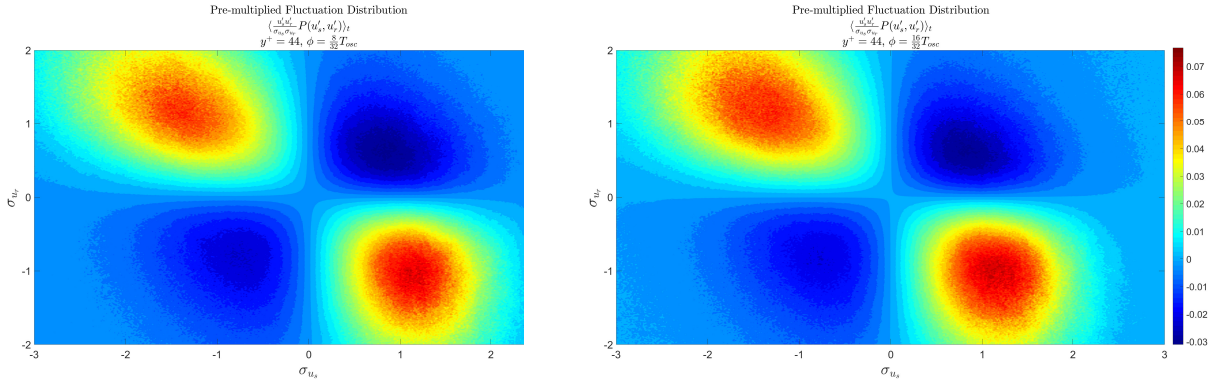

(a) Probability Distribution of the Streamwise and Azimuthal Fluctuations: $\phi = \frac{8}{32}\pi$

(b) Probability Distribution of the Streamwise and Azimuthal Fluctuations: $\phi = \frac{16}{32}\pi$

Figure B.22: Premultiplied Probability Density Function of (u'_x, u'_r) at $y^+ = 44$

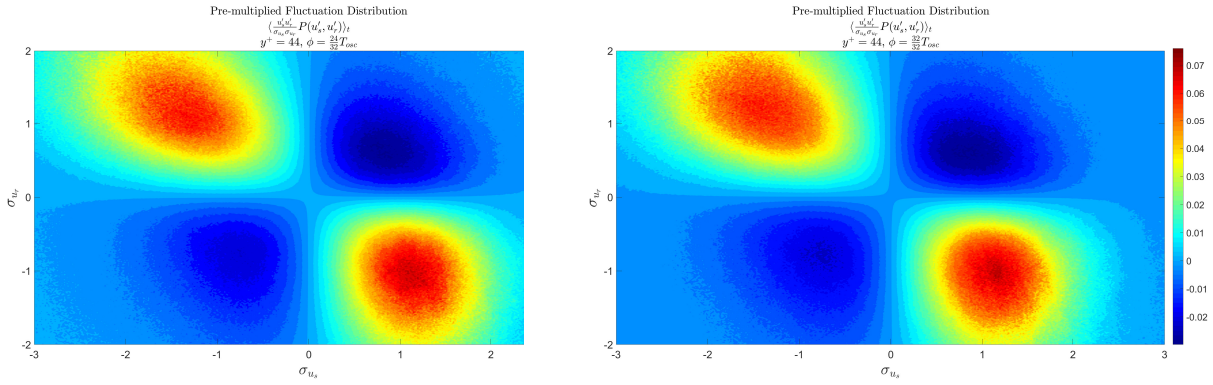

(a) Probability Distribution of the Streamwise and Azimuthal Fluctuations: $\phi = \frac{24}{32}\pi$

(b) Probability Distribution of the Streamwise and Azimuthal Fluctuations: $\phi = \frac{32}{32}\pi$

Figure B.23: Premultiplied Probability Density Function of (u'_x, u'_r) at $y^+ = 44$

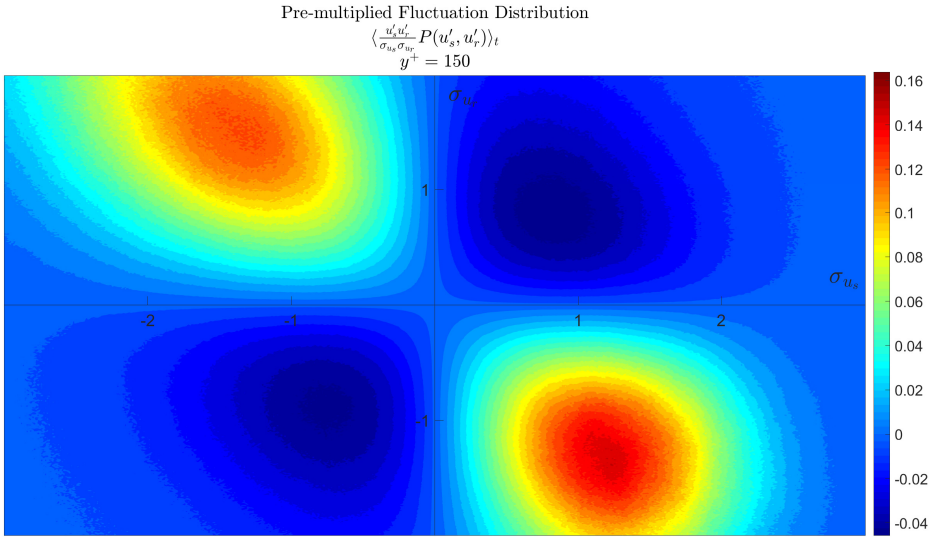

Figure B.24: Premultiplied Probability Distribution of the Streamwise and Azimuthal Fluctuations at $y^+ = 150$ for the standard pipe; $Re_\tau = 360$

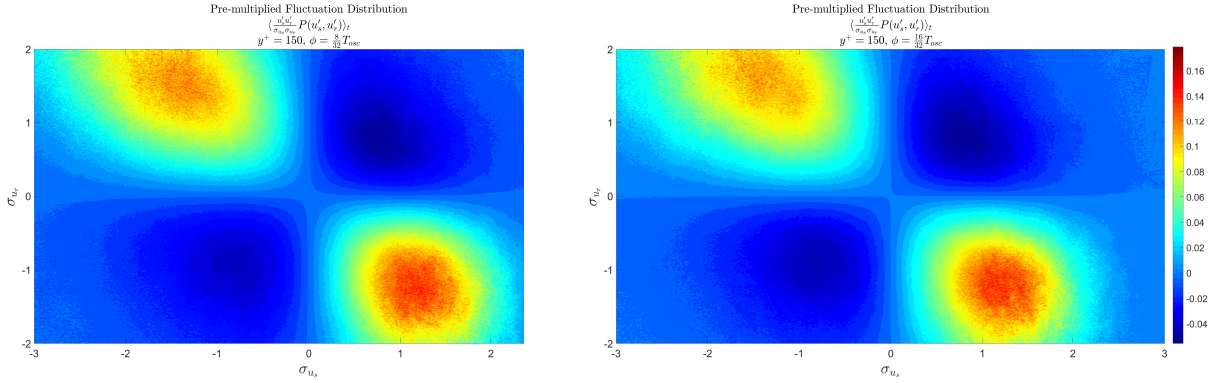

(a) Probability Distribution of the Streamwise and Azimuthal Fluctuations: $\phi = \frac{8}{32}\pi$

(b) Probability Distribution of the Streamwise and Azimuthal Fluctuations: $\phi = \frac{16}{32}\pi$

Figure B.25: Premultiplied Probability Density Function of (u'_x, u'_r) at $y^+ = 150$

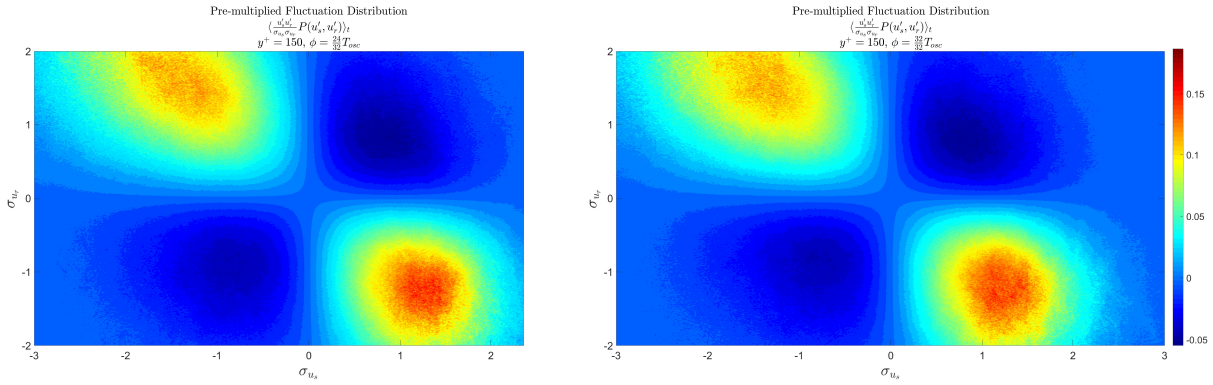

(a) Probability Distribution of the Streamwise and Azimuthal Fluctuations: $\phi = \frac{24}{32}\pi$

(b) Probability Distribution of the Streamwise and Azimuthal Fluctuations: $\phi = \frac{32}{32}\pi$

Figure B.26: Premultiplied Probability Density Function of (u'_x, u'_r) at $y^+ = 150$